Hydromagnetic Astrophysical Outflows

Thesis by

Ruben Krasnopolsky

In Partial Fulfillment of the Requirements

for the Degree of

Doctor of Philosophy

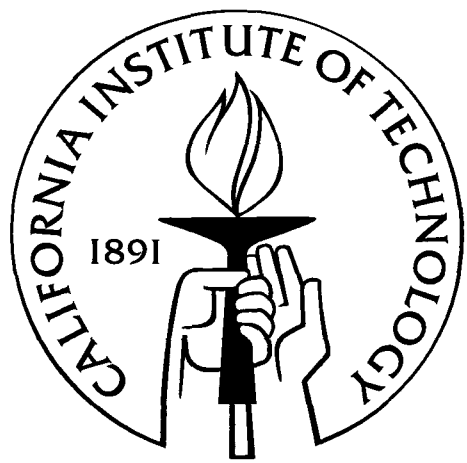

California Institute of Technology

Pasadena, California

2000

(Submitted 26 January 2000)

Acknowledgements

It is my pleasure to acknowledge:

- Caltech CACR, for parallel computer usage
- LCA, for the usage of ZEUS
- Dave J. McComas and B. Goldstein for the usage of data from the SWOOPS experiment aboard Ulysses.
- A. Balogh, for the usage of data from the magnetometer experiment aboard Ulysses.
- The NSSDC service, for the distribution of Ulysses data.

For direct of indirect contributions to the main meat of this thesis, I must also acknowledge the help of Eric Blackman, Roger Blandford, Peter Goldreich, John Hawley, Rick Jenet, Zhi-Yun Li, Dave Meier, Rashid Ouyed, and Jim Stone.

For appreciated and useful comments on different parts of this thesis, or for making the research environment more productive, I am happy to recognize the help of Ann Esin, Scott Hughes, Shinji Koide, Arieh Königl, Dustin Laurence, Yoram Lithwick, Jason Maron, Teresa Moore, Sterl Phinney, and Sima Setayeshgar

I thank the customer support of the Absoft Corporation for their prompt answer, which enabled us to continue using their FORTRAN compiler.

I appreciate USRA for granting my participation in the NASA Summer School for High Performance Computational Physics, during July 1996, in Maryland.

As almost everybody nowadays, this research has made use of NASA's Astrophysics Data System Abstract Service, which is here acknowledged.

Abstract

The launching, acceleration and stability of MHD outflows were studied numerically in two and three dimensions using a parallelized version of the ZEUS code.

The launching from Keplerian accretion disks was investigated using time-dependent simulations, to determine parameter dependence and stability to 3D perturbations. The most critical factors controlling the cold outflows from the disk surface were found to be the poloidal magnetic field profile and the mass discharge rate: together they determine the acceleration of gas away from the disk, and the location of the Alfvén surface, which, in turn, fixes the angular momentum loss and the asymptotic speed. The flows were found to be remarkably stable in 3D against perturbations of the initial conditions, at least in the formation region of the jet before the Alfvén surface. This is surprising in the context of previous studies.

Intermittent flows are found when the mass discharge rate is too large for a given magnetic field profile. This may be relevant to some observed episodic sources. This intermittency can be suppressed if the mass loading has the angular dependence suggested by the magnetocentrifugal mechanism, namely that the discharge is a function of the angle θ between the poloidal fieldline threading the disk and the rotation axis, turning off when $\theta \lesssim 30°$. The mechanism of intermittency sets up a maximum mass loading to the observed smooth jets, may explain those that are pulsed, and shows a possible transition back and forth between both regimes. The result presented here may be compared to some recently published papers which suggest that intermittency could occur if the mass loading is too small: here it occurs when it is too large. If both results are generic, mass loading is bracketed for steady flows.

Launching from disks was simulated using a cold disk and atmosphere. The number of boundary conditions that was imposed on the disk surface is what is necessary and sufficient to take into account information propagating upstream from the fast and Alfvén critical surfaces, avoiding over-determination of the flow and unphysical effects, such as numerical "boundary layers" that otherwise isolate the disk from the flow, produce impulsive accelerations and confuse the connection between the disk parameters and the flow.

The solar wind provides another example of an MHD outflow, using the high solar latitude observations by the satellite Ulysses. The simulations performed here allowed an estimate of the mean value of the azimuthal velocity, which is not directly accessible to measurement, and is necessary to estimate the torque of the solar wind. The Alfvén point was found to be located at $\sim 11 R_\odot$. Similar outflows from faster rotators were simulated, and found to be collimated along the rotational axis.

Contents

Chapter 1

Introduction

1.1 Observations

1.1.1 Collimated flows

Astrophysical jets are fast and well-collimated flows, observed in a wide variety of astronomical systems, of both stellar and galactic size.

Stellar jets are found associated with young stellar objects (e.g. Lada 1985). Other Galactic, stellar-size systems often associated with jets are microquasars (e.g. Mirabel & Rodríguez 1998, Hjellming 1997), such as SS433 (e.g. Margon 1984) or black hole X-Ray transients (e.g. Mirabel, Cordier, Paul, & Lebrun 1992). Extragalactic jets are frequently observed emanating from active galactic nuclei such as quasars (e.g. Begelman, Blandford, & Rees 1984). Table 1.1 shows typical outflow speeds, power, size and collimation angle of these different kinds of jet.

Table 1.1: Physical scales associated with jets or bipolar outflows in Active Galactic Nuclei, X-ray Binaries (XRB), and Young Stellar Objects (YSO). $V_{\rm jet}/c$ is a typical jet speed, and $L_{\rm jet}$ its luminosity. $M_\bullet/M_\odot$ and $R_\bullet$ are the mass and radius of the central object, and $V_{\rm esc}/c$ its local escape velocity. $R_{\rm coll}$ is an estimate of the radius by which collimation is achieved, and B is the inferred magnetic field at the source. All dimensioned quantities in cgs units.
Adapted from Blandford (1993), p. 17.

	AGN	YSO	XRB
$V_{\rm jet}/c$	1	10^{-3}	0.3
$L_{\rm jet}$	10^{44}	10^{35}	10^{40}
$M_\bullet/M_\odot$	10^8	1	10
$R_\bullet$	10^{14}	10^{11}	10^6
$V_{\rm esc}/c$	1	10^{-3}	0.3
$R_{\rm coll}$	10^{17}	10^{16}	10^{11}
B	10^4	10^3	10^9

When constructing a model, we must remember that there are indications that a single basic mechanism may be responsible for the formation and collimation of jets (e.g. Livio 1997). Accretion phenomena into a compact object seems to be present in all the relevant sources. Accretion disks have been observed in many cases, such as in YSO (e.g. Burrows et al. 1996), x-ray binaries and black hole x-ray transients (e.g. van Paradijs & McClintock 1995; Southwell et al. 1996). There is also some good evidence for the existence of accretion disks in the case of AGN, such as the nuclear disk of dust observed by Ferrarese, Ford, & Jaffe (1996), and the gas disks observed by Ford et al. (1997).

Another apparently universal characteristic is the fact that the outflow speed of jets is typically a few times the escape speed $v_{\rm esc}$ from the central object. This speed varies between a few hundred $\mathrm{km\,s^{-1}}$ in YSO, through mildly relativistic speeds of the order of 0.2 to $0.9c$ in microquasars, to highly relativistic speeds with Lorentz factor Γ of a few and up to 20 for AGN jets. Gamma Ray Bursts (GRB) may also form jets with Lorentz factors as high as $\Gamma{\sim}300$ (Piran 1999). The relation between asymptotic and escape speed hints that the mechanism of launching must be sensitive to the depth of the gravitational well, indicating that the jets originate in the vicinity of the central object.

An interesting although not universal characteristic of relativistic jets, both galactic and stellar, is apparent superluminal motion. This can happen when the jet is directed towards the observer. Shocks moving with velocity $v = \beta_s c$, at an angle θ to the line of sight, have an apparent transverse velocity in the plane of the sky equal to $\beta_{\rm app} c = \frac{\beta_s \sin\theta}{1-\beta_s \cos\theta} c$; this speed is larger than c for small values of the angle θ combined with large values of the Lorentz factor $\Gamma_s = (1-\beta_s^2)^{-1/2}$ (Rees 1966; Blandford, McKee, & Rees 1977). Some relativistic jets indeed have such point sources as features; tracking them over time shows their superluminal motion.

A related effect observed in similar conditions (small θ, large β) is *relativistic beaming* or *Doppler boosting* of the jet, which can boost the apparent luminosity of the source. The relativistic speed $\beta_f c$ of the fluid in the jet, not necessarily the same as the shock speed $\beta_s c$, has an associated Doppler boost factor $\mathcal{D} = \frac{1}{\Gamma_f(1-\beta_f \cos\theta)}$. If the source has a spectral index α, the observed flux at a given frequency is increased by a factor $\mathcal{D}^{2+\alpha}$. For small angles $\theta \ll 1$, the Doppler factor is of the order of the Lorentz Γ of the jet. If the source is intrinsically bipolar, with the opposite jets aligned, the counter-jet is also subject to Doppler effects, but its corresponding $\mathcal{D}$ is less than one, reducing the observable luminosity, so much that the jet might appear unipolar through Doppler dimming of the counter-jet. Performing the Lorentz transformation relative to proper time $\frac{dt_{\rm obs}}{d\tau}$ also shows that time variability is faster by a factor $\mathcal{D}$ in the beaming direction; this is relevant to some rapidly varying sources such as blazars. The enhanced luminosity of beamed sources makes them easier to observe. A small minority of beamed sources can dominate flux limited source samples.

1.1.2 Active Galactic Nuclei

Many galaxies show highly energetic nuclear activity, which has been observed in all electromagnetic frequencies from radio to γ-rays, and at spatial scales from intergalactic (Mpc scales) down to the resolution limit of the observations (typically 1pc for VLBI radio observations), allowing a very rich spectroscopy.

AGN activity takes many forms, although not all of them are present in a given object. Many AGNs show an optical nucleus of small angular size, brighter than its host galaxy, often observationally unresolved ("point-like"). Broad-band continuous emission from radio to γ-rays that cannot be

fit with a black-body model —showing that it is not only stellar in origin— is also typical. Strong emission lines, both broad and narrow, are present in most sources. Mild variability and weak polarization are seen in most cases, whereas strong variability and polarization are present in a few kinds of AGN, especially in "Blazars." Most AGN are weak radio sources, but a minority (~5–10%), called "radio loud" sources, have strong radio emission, remarkable for their huge spatial scales, often much larger than the galaxy size, with extended radio images showing lobes and jets.

Synchrotron radiation is emitted by relativistic electrons orbiting in the magnetic fields present in the AGN. This radiation has a substantial polarization, which gives information about the direction of the magnetic fields. Inverse Compton scattering by the same electrons also contributes to the power of the source, and also reprocess the synchrotron radiation inside optically thick sources.

Spectroscopy and morphology allow different classification schemes for AGN. This classification has grown following the development of observations, and it is still largely an unsystematic division of a set of objects whose real variation is a probably continuous. Some of the classifications might be dominated by the effects of orientation, beaming and obscuration. With this in mind, the following is a classification, mostly following Woltjer (1990).

Radio Galaxies (RG) While most galaxies have radio emission less than $10^{30.3}\mathrm{erg\,Hz^{-1}}$ (measured around 1.4GHz), radio galaxies have a much higher power, at least one or two orders of magnitude more intense. Radio maps show two large lobes, often much larger than the optical galaxy. Energy is being transferred from the galactic nucleus to the radio lobes by means of a fast collimated outflow; that is, a jet. These sources are often seen as bipolar, with two lobes and jets, one on each side of the galaxy. One of the observed jets sometimes is much brighter than the other. This is due to relativistic Doppler beaming, which enhances the apparent luminosity of sources moving towards us with a small angle by a power of its Lorentz Γ. Some apparently unipolar sources might in fact be bipolar with one of the sides amplified by beaming effects. Typically RG are associated with elliptical galaxies.

Radio galaxies have been classified according morphology by Fanaroff & Riley (1974) into two types, now called FRI and FRII. The morphological criterion is the distance between the two brightest spots in the opposite sides of the central galaxy, divided by the total extent of the radio source. If this ratio is less than 0.5, the source is classified as FRI, otherwise as FRII. The interest of this classification, is that many other properties of the sources correlate with this morphology.

Due to its definition, FRII radio galaxies have the lobes brightened at the edges, with radio hot spots located in the regions far away from the central galaxy. They also have a relatively dim jet connecting those spots to the source core. Their radio power is typically $P_{178\mathrm{MHz}} > 2\times10^{32}\mathrm{erg\,Hz^{-1}}$. FRI radio galaxies are relatively less powerful sources, with the edges of the

lobes darkened instead of brightened. Their jets are relatively brighter, and more liable to exhibit changes in curvature than in FRII sources.

Polarization data show that the magnetic field in FRI jets is seen as predominantly perpendicular to the jet direction, sometimes turning into parallel at the edges. By contrast, in FRII the magnetic field tends to be parallel to the jet (Bridle & Perley 1984). It has been suggested (Begelman, Blandford, & Rees 1984; Laing 1996) that the propagating jets consist of a spine, with a mostly perpendicular field and a shear layer outside, with a mostly parallel field. Edge-brightened sources, such as FRII, will show predominantly the radiation emitted from the shear layer, while center-brightened sources will show the field from the spine.

The observations above have been physically interpreted by assuming that the jets in FRIIs must be faster and more energetic, so that they are able to advance further into the intergalactic material before releasing some of their kinetic energy at the lobes; this would also explain why the edge-brightened sources are the more powerful.

Linear polarization is often observed, indicating the existence of ordered magnetic fields. Depolarization is also observed, stronger in the counter-jet of bipolar sources. This is explained as the effect of differential Faraday rotation through the medium surrounding the source, because the radiation from the counter-jet, which is further away from us, has to traverse a larger distance, and is more subject to depolarization (Laing 1988; Garrington et al. 1988).

During a study of the polarization properties of powerful radio sources, it became clear that in those sources with one-sided jets, depolarization with increasing wavelength is usually weaker for the lobe containing the jet. One obvious interpretation is that the depolarization is caused by differential Faraday rotation through irregularities in a magnetoionic medium surrounding the radio source. The side with the stronger jet is closer to us, is seen though a smaller amount of material, and therefore shows less depolarization. A halo of hot gas around the associated galaxy or quasar is a likely candidate for the depolarizing medium.

Radio-Loud Quasars (RLQ) The radio characteristics of these objects are similar to the more powerful RG, such as the FRII. However, the optical image is dominated by a bluish, unresolved, [1] luminous nucleus, with strong, broad emission lines. Most bright RLQ are also X-ray sources. It is probable that many powerful FRII radio galaxies are indeed RLQ, with their bright optical nucleus obscured by clouds of gas and dust. VLBI observations show that the nuclei of quasars have compact components, with measurable, superluminal proper motion on the plane of the sky, implying that there are beamed outflows at relativistic speeds (e.g. Unwin et al. 1989; Cohen 1989). The optical nuclei are often variable, especially in the flat spectrum

[1] Historical note: this unresolved nucleus, seen in the absence of the dimmer ambient galaxy, gave quasars their old name of "quasi-stellar objects."

radio sources[2] (FSRQ), which show also optical linear polarization. These FSRQ are related to the next two classes of source.

BL Lac objects These objects[3] resemble FSRQ, except that the optical broad emission lines are absent. They are highly variable at radio, optical and X-ray wavelengths, with strong and variable polarization. Their variability timescale in optical and X-ray can be less than a day, showing the presence of a small source. Two types have been observed, with peaks in their spectrum at respectively low and high frequencies: this is at least in part a bias effect due to taking samples from respectively radio and X-ray surveys. This is only one of the many instances where AGN classification is influenced by sample bias (Urry & Padovani 1995).

Optically Violently Variables (OVV) This is a class of quasars with optical characteristics like the BL Lac objects, but weak broad emission lines are present. OVVs, BL Lac objects and FSRQ are grouped together as "Blazars."

Blazars form a set of object of high variability at all wavelengths from radio to γ-rays, with high polarization, and flat-spectrum radio emission. It is probable that blazars contain relativistic jets pointing directly towards the observer (e.g., Urry & Padovani 1995;Urry 1996), with powerful relativistic beaming. This would explain their frequent superluminal motion (e.g. Vermeulen & Cohen 1994), high and rapidly variable polarization (e.g. Smith 1996), and the surprising intensity of their γ-ray emission (e.g. Dondi & Ghisellini 1995). Also, their rapid variability is attributable to superluminal expansion of the emitting features, with the Doppler factor shortening the time intervals of variation.

Powerful, beamed γ rays were observed in blazars, including BL Lac objects, FSRQ, and highly polarized quasars, by the instrument EGRET, on board the Compton Gamma Ray Obseratory. The luminosity above 100MHz can be larger than that emitted in all the other frequencies, and it is highly and rapidly variable. A rough estimation of the value of the Doppler boosts $\mathcal{D}$ was performed by Dondi & Ghisellini (1995), giving typical values between 1 and 10.

Radio-Quiet Quasars (RQQ, QSO) These objects resemble RLQ optically, but their radio emission is weak —though not silent. Most quasars are radio-quiet (~90%), so that optically selected quasars are sometimes assumed in surveys to be radio-quiet until strong radio emission is observed. The separation in radio power between RL- and RQ quasars is at $P_{5\mathrm{GHz}} \sim 10^{31.7} \mathrm{erg\,Hz^{-1}}$, close to the separation between weak and strong radio galaxies at this frequency. The X-ray emission relative to optical emission is lower for RGG than RLQ.

Some RQQ have very broad absorption lines in the optical, and are called BALQSO. Models of BALQSO present powerful, apparently uncollimated outflows, containing gas clouds (with

[2]Spectral index flatter than $\alpha = 0.5$ at GHz frequencies.
[3]Called after eponymous "variable star" BL Lacertae.

a small filling factor) where the absorption lines originate. The acceleration mechanism of the outflows may be either radiative, due to continuum or line radiation (Arav, Li, & Begelman 1994), hydromagnetic (Emmering, Blandford, & Shlosman 1992), or, more probably, a combination of both mechanisms at different distances from the central object (Königl & Kartje 1994). BALQSOs are almost never radio-loud. There is evidence that radiatively-driven outflows are generic in RQQ, with the BALQSOs being the case where the observer lies in the equatorial plane so that the flow is in our line of sight (Weymann, Morris, Foltz, & Hewett 1991).

Seyfert 1 (Sy1) The nuclei of these galaxies resemble RQQ, at a lower luminosity; the boundary is defined at $M_V = -23$. They have very broad hydrogen emission lines, with typical FWHM$\sim$5000km s^{-1}, and narrower forbidden lines, with FWHM$\sim$500km s^{-1}. Most Sy1 are radio sources with $P_{5\mathrm{GHz}} = 10^{27-30}\mathrm{erg\,Hz^{-1}}$. Their X-ray emission as compared to optical is a little stronger than for RQQ. This classification makes a continuum with the RQQ. Morphologically, these are often spiral galaxies.

Seyfert 2 (Sy2) The spectra of these galaxies have similar line widths for permitted and forbidden lines, with FWHM$\sim$500km s^{-1}; the hydrogen lines lack broad wings. Their nuclei have diameters ranging from point-like to 3kpc. They are weak X-ray sources. They have the same radio luminosity as Sy1, and, also like Sy1, they are associated with spiral galaxies. The optical spectra of RG can have either Sy1 or Sy2 properties, called Broad Line (BLRG) and Narrow Line Radio Galaxies respectively. Radio-loud quasars emission lines belong to the BLRG type, with wide wings.

The BL emission seems to come from a relatively dense region ($> 10^8\mathrm{cm^{-3}}$), whose size, deduced from variability, is around 10-100 light-days in Sy1, up to a few light-years in bright quasars. The gas velocity must be typically around 3000-10000km s^{-1}, large enough to justify the line width. In this same picture, the NL emission comes from a much larger region, where the density is around 10^3-$10^6\mathrm{cm^{-3}}$, and the gas speed is around one tenth of the above. This NLR region is resolved in some nearby Seyferts, with sizes around 100-300pc. The NLR in quasars is probably larger, around a few kpc.

Seyfert galaxies are by no means rare objects in the sky; based on CfA, the local fraction of Seyfert galaxies is around a few percent (Huchra & Burg 1992). It is widely believed than Sy1 and Sy2 are the same kind of object, observed from a different angle, so that Sy2 nucleus is partially obscured by an equatorial gas torus which happens to lie edge-on. Broad emission lines from Sy2 are observed in polarized radiation; in the unified model, this radiation is explained as being emitted from the central region in a non-equatorial direction, and then reflected towards us. The reflection mechanism would polarize the light, and allow it to reach

us avoiding the obscuration region (Antonucci & Miller 1994).

"Normal" Galaxies Some form of nuclear activity is present in all galaxies, often showing some of the typical AGN phenomena at a lower energy range. For instance, our Galactic center is marked by the compact radio source Sgr A*, which probably harbors a black hole with a mass $\approx 2.6\times10^6 M_\odot$, as shown by the motion of the stars close to this object (Ghez et al. 1998; Eckart & Genzel 1997).

Also, observations of the dynamics of the gas at the center of several normal galaxies, indicate central objects with a mass between $10^{6\text{-}9} M_\odot$, and with a large mass/luminosity ratio, indicating some darkness of the object (Kormendy & Richstone 1995). While these data do not conclusively prove the presence of central black holes, it is by far the most conservative explanation, because alternative models such as compact clusters or superstars are unstable in a timescale much shorter than the age of a galaxy or invoke objects whose existence violates the laws of physics.

Non-thermal low-ionization emission is a regular feature in most spiral galaxies (Keel 1983). The low-ionization nnuclear emission line regions (LINERs) and low-luminosity ("dwarf") Seyfert nuclei were detected by Ho, Filippenko, & Sargent (1997) in a large fraction of galaxies taken from a magnitude-limited sample.

1.1.3 Microquasars

The name of "microquasars" has been given to stellar-mass systems in our Galaxy showing relativistic jets, which exhibit on a smaller scale many characteristics of quasars.

These systems include a stellar-mass black hole or neutron star, which accretes material through an accretion disk from a binary companion. The accretion disk emits hard X-rays[4]; relativistic jets are launched, and are observed via synchrotron emission.

Most of the ingredients of quasar models are present here in the little; the central compact object (a few million times smaller in mass than in quasars), the accretion disk, and the collimated outflow (a few parsecs long, instead of the Mpc scale of extended radio galaxies). Microquasars are expected to show most of the same physics of quasars, and not only be superficially similar. Their properties are more convenient to observe in a human lifetime, because typical variation times are 10^5–10^8 times smaller.

Superluminal motion has been observed for microquasars, starting from the first observations in GRS1915+105 (Mirabel & Rodríguez 1994) and GRO J1655-40 (Tingay et al. 1995; Hjellming & Rupen 1995). In particular, the ejecta of GRO J1655-40 have an extremely fast proper motion in the plane of the sky (40 to 65 mas per day). This object is a binary of a star of 1.7-3.3$M_\odot$ and a

[4]Justifying the spectrally-biased name of X-ray binaries given to these sources.

collapsed object of 4-7$M_\odot$ (Orosz & Bailyn 1997; Phillips, Shahbaz, & Podsiadlowski 1999). Given the large mass of the collapsed object, which is above the maximum stable mass for a neutron star, it has been concluded that this is a black hole (Kalogera & Baym 1996).

A review on microquasars can be found in Mirabel & Rodríguez (1999). A review of the object SS433 can be seen in Margon 1984. Jet power and formation has been studied by Levinson & Blandford (1996).

1.1.4 Young Stellar Objects

A young star is formed by gravitational collapse in the dense core of a cloud. This core later accretes material, via an accretion disk. However, at the same time that gas falls in, large outflows are produced: it is often speculated that some of this outflow is necessary for accretion to proceed, releasing the excessive angular momentum of the cloud material, viscous mechanisms being probably insufficient for this (e.g. Königl & Pudritz 2000). The infalling material forms first an accretion disk around the central object, rotating at a Keplerian speed which prevents its immediate collapse. This theoretically-expected disk has been observed in compelling detail by the Hubble Space Telescope (HST), notably in the object HH30 (Burrows et al. 1996). The size of these disks is typically of the order of the solar system. In the case of HH30, the size of the disk is 500AU, and that of the jet is 1600AU, with a jet velocity of 300km s^{-1}.

The young stellar jets have speeds of the order of several hundred km s^{-1}, higher for high luminosity sources; these speeds are inferred from both emission lines and the proper motion of knots inside the jet. This collimated outflow forms a bipolar jet, which interacts with the interstellar medium on parsec-scales forming the Herbig-Haro objects, which are nebulae of shocked material. These HH objects have the shape of bow shocks or knots, tracking the trajectory of the jet. In some cases, such as HH34, a long chain of HH objects is visible (Reipurth et al. 1986). The jets are accompanied by bipolar, poorly collimated outflows (Lada 1985).

1.1.5 Uncollimated flows: Stellar Winds

Most stars emit some mass in the form of a stellar wind. In the case of the Sun, it is a fast, mostly radial outflow of ionized plasma (400–800km s^{-1}), with a mass loss rate of $\sim 2\times10^{-14} M_\odot$ per year. For other stars, however, the loss due to the wind might be significative for its evolution. Different mechanisms have been proposed, adapted to the circumstances of the different stars and flows observed: no generic theory valid for all objects is expected. In the case of the Sun, it is probably a thermally driven wind from the corona (Parker 1958), combined with an Alvén-wave driven mechanism (Hartmann & MacGregor 1982). In early times in the life of a star, when its rotational speed is faster, a magnetocentrifugal mechanism may be also relevant (Weber & Davis

1967).

1.2 Theories

This observational summary surely demonstrates that outflows are typically observed to accompany accretion. Sometimes they are relativistic, sometimes not. Sometimes they are collimated into jets, sometimes not. Sometimes they are magnetically driven, sometimes not. There is a wealth of phenomenology that is difficult to interpret because of strong orientation effects (relativistic beaming and absorption). It is the primary goal of theoretical research, like that described below, to match these observations to the properties of physical flows.

1.2.1 Hydromagnetic models of jets

Hydromagnetic models start from the equations of MHD, frequently restricted to axisymmetry. The energy is extracted from the accretion disk, or from the magnetic field. In some variants of the model, gas pressure and magnetic turbulent pressure may also help in the launching. Most of the models in this category are quasi-stationary, and can be studied with either the steady state or the time dependent equations. Other models are fundamentally episodic, or intermittent (Uchida & Shibata 1985; Ouyed & Pudritz 1997a). Both possibilities are considered below.

Before describing the models, it is convenient to write down the equations that govern MHD outflows.

1.2.2 Theory of MHD outflows

A generic hydromagnetic outflow, accelerated or not, collimated or not, can be modeled by the usual equations of adiabatic MHD, which are presented here in order to to fix the notation:

$$\frac{\partial \rho}{\partial t} + \nabla \cdot (\rho \mathbf{v}) = 0 \tag{1.1}$$

$$\rho \frac{\partial \mathbf{v}}{\partial t} + \rho (\mathbf{v} \cdot \nabla) \mathbf{v} = -\nabla p + \rho \nabla \Phi_g + \mathbf{j} \times \mathbf{B}/c \tag{1.2}$$

$$\frac{\partial \mathbf{B}}{\partial t} = \nabla \times (\mathbf{v} \times \mathbf{B}) = \nabla \times \mathcal{E} \tag{1.3}$$

$$\frac{\partial u}{\partial t} + \nabla \cdot (u \mathbf{v}) = -p \nabla \cdot \mathbf{v} \tag{1.4}$$

$$p = (\gamma - 1) u \tag{1.5}$$

where

$$\rho = \text{matter density} \tag{1.6}$$

$$\mathbf{v} = \text{velocity flow field} \tag{1.7}$$

$$\mathbf{B} = \text{magnetic field} \tag{1.8}$$

$$\mathbf{j} = (c/4\pi)\nabla \times \mathbf{B} = \text{current density} \tag{1.9}$$

$$\mathcal{E} \equiv \mathbf{v} \times \mathbf{B} = -c\mathbf{E} \tag{1.10}$$

$$\Phi_g = \text{gravitational potential} \tag{1.11}$$

$$p = \text{thermal pressure} \tag{1.12}$$

$$u = \text{internal energy density (per unit volume)} \tag{1.13}$$

$$\gamma = \text{adiabatic index.} \tag{1.14}$$

These adiabatic equations do not include phenomena such as resistivity, viscosity, cooling, heat transfer, ambipolar difussion, etc., each of which would add an extra term to the equations.

Cylindrical coordinates (z, R, ϕ) are usually preferable. The projection of a vector on the poloidal plane (z, R) will be indicated with a sub-index p, so that for instance, the velocity vector $\mathbf{v}$ can be written as $\mathbf{v} = \mathbf{v}_p + v_\phi \hat{\phi} = v_z \hat{z} + v_R \hat{R} + v_\phi \hat{\phi}$. Spherical coordinates, when needed, will be labeled as (r, θ, ϕ), preventing confusion between the cylindrical and spherical radii R and r.

The components of the current in cylindrical coordinates are

$$\left(\frac{4\pi}{c}\right) j_z = \frac{1}{R}\frac{\partial}{\partial R} R B_\phi - \frac{1}{R}\frac{\partial B_R}{\partial \phi} \tag{1.15}$$

$$\left(\frac{4\pi}{c}\right) j_R = -\frac{\partial B_\phi}{\partial z} + \frac{1}{R}\frac{\partial B_z}{\partial \phi} \tag{1.16}$$

$$\left(\frac{4\pi}{c}\right) j_\phi = \frac{\partial B_R}{\partial z} - \frac{\partial B_z}{\partial R} \tag{1.17}$$

At first, instead of solving this full system of equations, a simplified case of great astrophysical importance will be shown; the experience gained will help in acquiring an intuition for the kinds of solutions expected in the more general case.

1.2.2.1 Axisymmetric, steady outflows

The most developed part of the theory of compressible MHD outflows is that dealing with stationary axisymmetric flows. The fieldlines can be labeled using the flux function ψ, such that

$$B_z = \frac{1}{R}\frac{\partial \psi}{\partial R} \quad \text{and} \quad B_R = -\frac{1}{R}\frac{\partial \psi}{\partial z}\,, \tag{1.18}$$

with the boundary condition $\psi(z, R=0)=0$. This flux function is related to the magnetic flux Ψ across a circle of radius R by $\psi = \Psi/2\pi$, and to the magnetic vector potential component A_ϕ by $\psi = RA_\phi$.

There are five constants of the motion derivable from the axisymmetric, steady equations of motion, which appear as functions that are constant along fieldlines in the poloidal plane (Mestel 1968, Weber & Davis 1967, Heinemann & Olbert 1978, Blandford & Payne 1982), becoming functions of ψ alone:

$$k(\psi) = 4\pi\rho v_p/B_p, \text{ the ratio of mass to magnetic flux;} \tag{1.19}$$

$$\Omega(\psi) = \frac{1}{R}\left(v_\phi - B_\phi v_p/B_p\right), \text{ the corotational angular velocity;} \tag{1.20}$$

$$l(\psi) = R\left(v_\phi - B_\phi/k\right), \text{ the specific angular momentum;} \tag{1.21}$$

$$e(\psi) = v^2/2 + h + \Phi_g - \Omega R B_\phi/k, \text{ the specific energy; and} \tag{1.22}$$

$$S(\psi) = k_B(\gamma-1)^{-1}\ln\left(p/\rho^\gamma\right), \text{ the specific entropy,} \tag{1.23}$$

where h is the specific enthalpy of the fluid, $h = \int_{\psi=\text{const}}(dp/\rho)$, equal for an adiabatic equation of state to $h = \frac{\gamma}{\gamma-1}\frac{p}{\rho} = \frac{c_s^2}{\gamma-1}$. It is convenient to define derivative operators $\partial/\partial s$ and $\partial/\partial n$, respectively along and across fieldlines, so that for instance $\partial e/\partial s = 0$. The angle of inclination of the fieldlines to the axis is called θ, so that

$$\partial/\partial s = \cos\theta(\partial/\partial z) + \sin\theta(\partial/\partial R) \tag{1.24}$$

$$\partial/\partial n = -\sin\theta(\partial/\partial z) + \cos\theta(\partial/\partial R)\ . \tag{1.25}$$

Three Alfvén speeds are of particular interest, $v_{Ap} = B_p/\sqrt{4\pi\rho}$, $v_{At} = B/\sqrt{4\pi\rho}$, and $v_{A\phi} = B_\phi/\sqrt{4\pi\rho}$, constructed out of the poloidal, total, and azimuthal magnetic field.

In the axisymmetric steady state the velocity is related to the magnetic field by $\mathbf{v} = \frac{k\mathbf{B}}{4\pi\rho} + R\Omega\hat{\phi}$, so that

$$\frac{v_z}{B_z} = \frac{v_R}{B_R} = \frac{v_\phi - R\Omega}{B_\phi} = \frac{v_p}{B_p} = \frac{k}{4\pi\rho}\ . \tag{1.26}$$

The quantity Ω is related in steady state to the electric field components by $\Omega = \mathcal{E}_R/RB_z$ and, in the case of launching from a Keplerian accretion disk, it is expected to be close to the Keplerian angular speed at the disk surface, so that

$$\Omega^2 = \frac{1}{R_f}\left(\frac{\partial\Phi_g}{\partial R}\right)_{z=0} \equiv \left(v_K/R_f\right)^2\ , \tag{1.27}$$

where v_K is the Keplerian speed at the footpoint R_f of a given fieldline ψ.

These equations determine most properties of the flow along a given fieldline, with proper boundary conditions. The last equations required are the conservation of mass,

$$\nabla \cdot (\rho \mathbf{v}) = 0 \tag{1.28}$$

and the balance of forces across fieldlines, which can be written as a Grad-Shafranov equation (Lovelace et al. 1986)

$$\left(1 - \frac{k^2}{4\pi\rho}\right)\left(R\frac{\partial}{\partial R}\frac{1}{R}\frac{\partial}{\partial R} + \frac{\partial^2}{\partial z^2}\right)\psi - k\nabla\left(\frac{k}{4\pi\rho}\right)\cdot\nabla\psi =$$
$$= -4\pi R^2\rho\left[e' - (\Omega l)' + Rv_\phi\Omega'\right] - k(Rv_\phi - l)[Rv_\phi k' - (lk)'] + 4\pi R^2 p\left(\frac{S'}{k_B}\right) , \tag{1.29}$$

where the primes represent derivatives with respect to ψ, or equivalently as (e.g. Ustyugova et al. 1999; Bogovalov 1997)

$$\left(v_p^2 - v_{Ap}^2\right)\frac{\partial\theta}{\partial s} - \frac{\cos\theta}{R}\left(v_\phi^2 - v_{A\phi}^2\right) + \frac{1}{\rho}\frac{\partial}{\partial n}\left(p + \frac{B^2}{8\pi}\right) + \frac{\partial\Phi_g}{\partial n} = 0 \tag{1.30}$$

The force balance equation is difficult to solve analytically; however, self-similar descriptions have been used, which reduce the problem to the solution of coupled ODEs and give some insight.

Equation 1.30 may be regarded as governing the collimation, as it gives the derivative of θ along the fieldlines, $\frac{\partial\theta}{\partial s}$. It can be seen here that collimation may be either dominated by the poloidal field (through the term $-\frac{1}{8\pi\rho}\frac{\partial B_p^2}{\partial n}$), by the toroidal field (through a term that can be written as $-\frac{1}{8\pi\rho R^2}\frac{\partial(RB_\phi)^2}{\partial n}$), or by the thermal pressure (through a term $-\frac{1}{\rho}\frac{\partial p}{\partial n}$).

Collimated outflow models can be classified on the basis of which of these three effects is predominant in collimating the wind, as either toroidal, poloidal, or thermal.

The force per unit mass along a fieldline can be written as (Ustyugova et al. 1999)

$$f = \frac{v_\phi^2}{R}\sin\theta - \frac{1}{8\pi\rho R^2}\frac{\partial(RB_\phi)^2}{\partial s} - \frac{1}{\rho}\frac{\partial p}{\partial s} - \frac{\partial\Phi_g}{\partial s} . \tag{1.31}$$

Terms of particular interest in this force are the magnetocentrifugal acceleration

$$f_C = \frac{v_\phi^2}{R}\sin\theta \tag{1.32}$$

and the magnetopropulsive acceleration

$$f_M = \frac{1}{\rho c}(\mathbf{j}\times\mathbf{B})\frac{\mathbf{B}_p}{B_p} \tag{1.33}$$
$$= -\frac{1}{8\pi\rho R^2}\frac{\partial(RB_\phi)^2}{\partial s} \tag{1.34}$$

These two forces, together with the thermal push $f_p = -\frac{1}{\rho}\frac{\partial p}{\partial s}$, must counter the projected gravitational pull $f_g = -\frac{\partial \Phi_g}{\partial s}$. Depending on which of the three pushing terms dominates at low altitudes above the outflowing surface, a model describing the launching of an outflow can be called magnetocentrifugal, magnetopropulsive, or thermal.

1.2.2.1.1 Parker thermal wind launching theory

The equations of this axisymmetric theory are already more complex than those of Parker's theory of stellar outflows (Parker 1958), and can be regarded as its natural extension.

Parker theory created the concept of *solar wind*, in the context of a study of the outer solar atmosphere (the corona). Starting from the equations of fluid dynamics, it was found that in order to find solutions with a pressure at a few solar radii compatible with observation (relatively high), and a pressure at infinity comparable to that of the interstellar medium (close to zero), it was necessary to postulate a permanent outflow of material; the Sun is losing matter, at a rate that is now estimated around $\sim 2\times10^{-14} M_\odot$ per year. In spherical symmetry, the relevant equation is

$$\frac{dv_r}{dr}\left(v_r - \frac{2k_B T}{m_i v_r}\right) = \frac{2k_B r^2}{m_i}\frac{d}{dr}\frac{T}{r^2} - \frac{GM_\odot}{r^2} \ , \tag{1.35}$$

where m_i is the mass of the solar wind particles. The details of the solution of this equation depend on the profile of $T(r)$; however, the topology of the solutions does not depend strongly on this profile, giving solutions with the shape shown in Fig. 1.1 for temperatures declining less rapidly than $1/r$. Three kinds of solutions connect small and large distances from the source; subsonic (below the AD line), supersonic (above the CB line), and a single transonic curve, going from A to B, and passing smoothly through a critical point where the outflow speed becomes equal to the local isothermal sound speed $c = \sqrt{2k_B T/m_i}$. In the case of the Sun, the flow at small radii is locally subsonic, which forces the rejection of the supersonic solutions; the subsonic solutions (so called *breeze* solutions) yield a non-zero pressure at infinity, much larger than the interstellar gas pressure. Despite early criticism by Chamberlain (1961, 1965) only the transonic solution is now considered to be relevant. The existence of critical points in these solutions restricts the freedom in the choice of parameters, in contrast to purely subsonic outflows. The Parker solution is appropriate under a wide set of assumptions for the equation of state giving the thermal pressure. However, it does not take into account the dynamical effects of the magnetic field on the flow.[5]

1.2.2.1.2 Critical points in axisymmetric, steady MHD

The full addition of magnetic fields to this outflow problem can be done with the help of the equations 1.18–1.30. Solving them also requires the crossing of critical points. Instead of crossing one

[5]The justly celebrated Parker spiral —the profile of B_ϕ/B_p as a function of radius— takes into account only the kinematic effect of the flow on the magnetic fields.

critical (sonic) point as in the Parker problem, there are now up to three critical points, corresponding to the crossing of the slow magnetosonic speed ($v_p \sim c_{\rm sound}$), the Alfvén speed ($v_p = B_p/\sqrt{4\pi\rho} \equiv v_{Ap}$), and the fast magnetosonic speed ($v_p \sim B/\sqrt{4\pi\rho} \equiv v_{At}$, for a cold flow). If these points are to be crossed at all, the flow must be smooth across them. Crossing the fast critical point is not required by the observation of stellar winds (sub-fast flows at infinity are possible), but it is probably required by all applications dealing with astrophysical jets, due to their large observed speeds. Crossing the Alfvén point poses a strong restriction on the transported angular momentum, namely $l = R_A^2\Omega$, where R_A is the *cylindrical* radius at the point where the flow makes the Alfvénic transition $v_p = v_{Ap}$ (Mestel 1968, Weber & Davis 1967). The slow magnetosonic crossing produces a more complex condition, ultimately constrains the mass outflow ρv_p along the fieldlines, analogously to the sonic critical point in Parker's hydrodynamic model in a high plasma β flow. Crossing of the fast point also produces a complex condition, involving $|B|$, which constrains the outflow of angular momentum.

1.2.3 Axisymmetric, time dependent outflows

In time dependent theory, the functions 1.19-1.23 are no longer constant along fieldlines.[6] However, it is convenient to carry out time-dependent studies even when looking for steady state solutions. Steady-state methods usually do not give the most general solutions, due to the great complexity of the critical surfaces whose loci are unknown a priori (Heinemann & Olbert 1978). Time dependent methods also guarantee that, if a final steady-state solution is found at the end of a study, it is reachable for the given set of initial and boundary conditions, satisfying causality automatically. However, unsteady and intermittent (§4.3) solutions also become possible.

1.2.4 3D MHD outflows

3D MHD outflows are largely unexplored. It has been argued (e.g. Begelman 1998) that MHD instabilities may be destructive for these flows. For instance, outflows whose magnetic field is dominated by the B_ϕ component have been compared to Z-pinches, which are known to be unstable to a variety of modes distorting the plasma column, such as the $m = 0$ "sausage" mode, and the $m = 1$ and higher kink instabilities. Kink instabilities are essentially 3D, and this dimensionality must be used to study their non-linear development. Furthermore the equilibrium flows that we model are far more complex than the static configurations studied analytically, because they involve lateral expansion, longitudinal shear and radial density gradients.

Against this expectation of MHD instability, it should be mentioned that fast acceleration is a common characteristic to many of these outflows, together with strong velocity shears. Moreover,

[6] At a boundary where the conductivity is very high, it is still possible to impose values for the quantity Ω, related to an electric field component.

the dominance of B_ϕ over the poloidal components $\mathbf{B}_p$ is not fully established during the launching process until the Alfvén surface is reached (Königl & Pudritz 2000).

1.2.5 The magneto-centrifugal model

This jet-launching mechanism was proposed by Blandford & Payne (1982), investigated for instance in Clarke, Norman, & Burns (1986), Lovelace, Mehanian, Mobarry, & Sulkanen (1986), Pudritz & Norman (1986), Königl (1989), Ostriker (1997), and reviewed recently by Königl & Pudritz (2000).

Consider poloidal magnetic fieldlines emerging from the surface of an accretion disk. In steady state, the flow will be along these lines, due to the frozen-in property of ideal MHD flows. We can picture one element of gas flowing along a fieldline as a 'bead' sliding on a rigid 'wire' (Henriksen & Rayburn 1971). Let that bead start from $z = 0$, at a slow speed or at rest. The wire is rotating at a constant angular speed Ω. This will exert on the bead a centrifugal force outwards, competing against the gravitational force pulling the bead inwards. For a lever arm large enough, the centrifugal force wins this competition, and the field line propels the flow. This happens when the inclination θ of the poloidal fieldlines from the axis is larger that a critical angle θ_c, allowing the flow to accelerate centrifugally along the fieldline as if shot by a sling. This critical angle is $\theta_c = 30°$ for Newtonian gravity and Keplerian rotation.

During rotation, the fieldlines are twisted backwards due to the inertia of the outflowing gas, creating a toroidal B_ϕ. The magnetic pressure of this field component tends to collimate the flow, decreasing θ along a fieldline for increasing height z, as shown in equation 1.30. In addition, the gradient in the poloidal field pressure causes focusing, depending on the shape of the flux function. The three critical surfaces of MHD axisymmetric theory may be present: the Alfvénic surface ($v_p = B_p/\sqrt{4\pi\rho} \equiv v_{Ap}$), depending on the poloidal magnetic field; the fast surface ($v_p \sim B/\sqrt{4\pi\rho} \equiv v_{At}$), depending on the total magnetic field, and the slow magnetosonic surface, with ($v_p \sim c_{\rm sound}$). Blandford & Payne (1982) consider two kinds of winds: sub-fast, just able to reach the fast speed asymptotically at infinity, and super-fast, which make this transition at a finite distance from the source, typically not very far from their Alfvénic point.

Close to the disk, v_ϕ is not far from v_K, making a powerful force f_C. Gradients of the toroidal magnetic field provides a force term f_M, which also helps in pushing material up the gravity well. Further up, but typically still below the Alfvén surface, the term f_M starts to be larger than f_C. Beyond the Alfvén surface, the poloidal magnetic field becomes dynamically small, and is wound up by the outflow efficiently, generating a large B_ϕ, and reducing v_ϕ. The centrifugal force f_C is therefore small; the only possible acceleration will be due to departures of B_ϕ from its expected R^{-1} dependence. This is why most of the acceleration is expected to be complete by the Alfvén surface, making v_A and v_∞ of the same order. If the collimation mechanism reduces θ by a large amount for small z, then f_C becomes small (due to the reduced $\sin\theta$ factor), and becomes inefficient to launch

the jet. The magnetocentrifugal mechanism is more efficient if collimation is not dominant before the Alfvén surface is reached.

The magnetocentrifugal model has the advantage that it is able to explain both acceleration and collimation inside the same picture. It can work with a variety of profiles for the flux profile $\psi(R)$ along the disk. It is quite likely that open magnetic field lines thread accretion disks over many decades in radius. Note that the fraction of the disk surface that is threaded by open field lines may be quite small (Blandford & Payne 1982). In the models that follow, we define an effective disk surface in the corona, above the closed loops.

This assumption can be contrasted with Shu et al. (2000), who have proposed for young stars the X-wind model, which concentrates the open field lines on a thin ring close to the inner radius of the accretion disk. This question about the radial extent of the region on the disk threaded by open poloidal lines is linked to assumptions about the ambient medium (whose pressure at large distances should keep the open poloidal fieldlines from falling towards the equator in the large radius picture), and the efficiency of reconnection process on the disk surface (which cannot be allowed to be too efficient for thin ring pictures, because fieldlines with $\theta \sim 90°$, skimming over the accretion disk would otherwise reconnect outwards);

The question about the critical angle, is potentially threatening to the model. It has been argued that the nature of the accretion flow may make it difficult to achieve the expected values of $\theta > 30°$ (Lubow et al. 1994): $\theta = 30°$ might be an unstable equilibrium. Since demonstrations omit key ingredients of the model, these results are not necessarily applicable to all accretion flows. However, even admitting them, Ouyed & Pudritz (1997a) have shown that, if the initial field lines start from such an inconvenient angle as $\theta = 0°$, the formation of the toroidal magnetic field can make the fieldlines open outwards —even if temporarily— so much that jet launching will still be present, at least episodically.

Another question is how the open poloidal fieldlines happen to form. A plausible mechanism has been studied by Romanova et al. (1997), where magnetic field loops, initially closed, open up due to differential rotation of the footpoints at different radii on the disk surface in the regions where the plasma $\beta \lesssim 1$. Dynamo-generated magnetic fields are probably still not the answer, at least in the thin disk case, because they tend to have too large a B_ϕ/B_p ratio for the models to proceed efficiently. Numerical studies concentrating on the atmosphere around the accretion disk (such as those by Miller & Stone 1997) may help in answering these questions about the disk-jet interaction.

1.2.6 Stationary magnetopropulsive models

In these models, the force term f_M (equation 1.33) is important even at $z = 0$, making most of the launching. A strong gradient $\frac{\partial B_\phi}{\partial z}$ is required close to the disk surface such as in Contopoulos (1995) astrophysical plasma gun. These models are similar to the magnetocentrifugal picture; the forces

involved are the same, changing only their relative importance. Intermediate cases may happen. For instance, many simulations show at $z = 0$ a value of Ω dominated by v_ϕ, but a value of l dominated by B_ϕ.

1.2.7 Non-stationary magnetopropulsive models and the magnetic spring

These models are highly dynamical, and have been studied more by simulation than analytically. They depend on creating a strong $\frac{\partial B_\phi}{\partial z}$ by twisting field lines in a tight configuration. Once a strong magnetic field gradient is created, this "magnetic spring" becomes large enough to launch coronal material. This differs from the model shown in §1.2.6 in being essentially out of steady state, and frequently episodic.

Uchida & Shibata (1985) create the initial tension by starting with a sub-Keplerian flow whose infall twists fieldlines rapidly. Magnetic pressure then drives a hollow jet. This initial state is very far from equilibrium, but it still determines the final solution. The formation of the sub-Keplerian flow is not a part of the simulation. No steady state can be achieved, and the initial state cannot be reproduced.

The Bell & Lucek (1995) model starts in Keplerian, hydrostatic equilibrium. Differential rotation in the corona twists the initially poloidal magnetic field, creating a component B_ϕ. This toroidal component propagates into the fluid in a torsional Alfvén wave, which reduces the angular momentum of the material at the disk surface. This reduces v_ϕ at the disk surface: this process is also referred to as "magnetic braking of the disk." Keplerian equilibrium fails, and the gas at the disk surface falls into more central regions. This increases the gas pressure there, enough to drive a powerful jet.[7]

The simulations presented in §4.3 have some of the features of these models, with the great advantage that the flow is able to reproduce the initial conditions approximately, making intermittent episodes of outflow driven by the magnetic spring instead of single transients. They also differ from Bell & Lucek (1995) in being cold; launching is based on magnetic pressure and centrifugal forces.

1.2.8 Blandford-Znajek mechanism

When a black hole is in rotation (such as the astrophysically expected Kerr black holes), part of its energy is stored in its spin, and can be extracted. Blandford & Znajek (1977) proposed a mechanism for this extraction of rotational energy. When a black hole in rotation is threaded by a magnetic field, an electromotive force appears. This "battery" can drive an electric circuit: its internal resistence is 377Ω (given by the black hole magnetic properties), and its resistive load is at the base of the wind being launched by this mechanism. The electromagnetic power produced is of the order of the area

[7]This feature is not present in Uchida & Shibata (1985), who allow the material falling into central regions to accrete immediately into the central object, and do not obtain large gas pressures.

of the black hole, times the magnetic pressure of the field that effectively threads the black hole, times the speed of light.

It is very plausible that this mechanism extracts energy from a black hole, powering an axial jet, at the same time that some other mechanism extracts energy hydromagnetically from the disk, powering an outer envelope for the axial jet, and becoming responsible for its collimation.

1.3 Numerical simulations of jet launching

The historical development of jet launching simulations started then with non-steady, transient phenomena, probably due to the computational costs involved in keeping a numerically stable simulation running for a long time. This is in contrast to analytical work, which started from steady state studies, which are the most convenient case for theoretical analysis. Later, long term simulations appeared, aiming for steady state solutions. Nowadays some of the longest term simulations are also aiming for episodic behavior, in an apparent full circle to the initial, transient studies, but now without a stringent dependence on initial conditions.

The first simulations of jet launching were published by Uchida & Shibata (1985); they are not based on the magnetocentrifugal mechanism, instead they simulate a transient flow, based on the magnetic spring mechanism (§1.2.7). [8] A variant of this mechanism is simulated by Bell & Lucek (1995), and its stability investigated by Lucek & Bell (1997).

Simulations of jet launching based on the magnetocentrifugal model include Lind et al. (1989), Ouyed & Pudritz (1997b), Romanova et al. (1997), Ustyugova et al. (1999), Krasnopolsky et al. (1999).

Relativistic simulations of launching are already starting, using flat, Schwartszchild (Koide et al. 1998, Koide et al. 1999), and Kerr metrics. Up to now, these simulations are not cold (gas pressure effects are very important), and are dominated by transient infalls due to the initial conditions. Computational costs are probably still too large for either stationary or recurrent, episodic relativistic simulations, but, comparing to the history of the non-relativistic case, it appears that they will be coming soon.

Non-relativistic studies of jet propagation (as opposed to launching) have been studied by e.g. Hardee et al. (1997). Relativistic jet propagation has been studied by e.g. Nishikawa et al. (1997). Effects of the interaction with the ambient medium have been studied by Nishikawa et al. (1998).

[8] Kudoh, Shibata, & Matsumoto (1998) argue that it represents the magnetocentrifugal mechanism, on the grounds of some characteristics they have in common. However, the use of a sub-Keplerian corona misses one of the most important features in Blandford & Payne (1982), namely the almost complete cancelation between centrifugal and gravitational force at the disk surface, which allows the existence of the critical angle of 30°.

1.4 This Thesis

In this thesis simulations of astrophysical outflows are presented. Simulated jets are launched from accretion disks in a cold atmosphere in chapter 3, together with improved boundary conditions studied in §2.2.1. Collimated outflows from a finite disk are shown in chapter 4. In particular, a model of transition from stationary to intermittent flows is studied in §4.3. The stability of the launching mechanism against 3D perturbations is studied numerically in chapter 5. Finally, the largelly non-collimated solar wind flow is studied, based on data and simulations in chapter 6. To do all these simulations, a parallel version of the ZEUS code (Clarke et al. 1994) was written, and presented in §2.1.3.

Fig. 1.1 *Solutions of the Parker solar wind equation plotted as radial velocity vs. radius for a temperature profile decreasing less steeply than* $1/r$. *The curve labeled* $(2kT/M)^{1/2}$ *represents the local isothermal speed. The unique wind solution connects from A to B, passinght through the critical point.*

Source: Parker (1965).

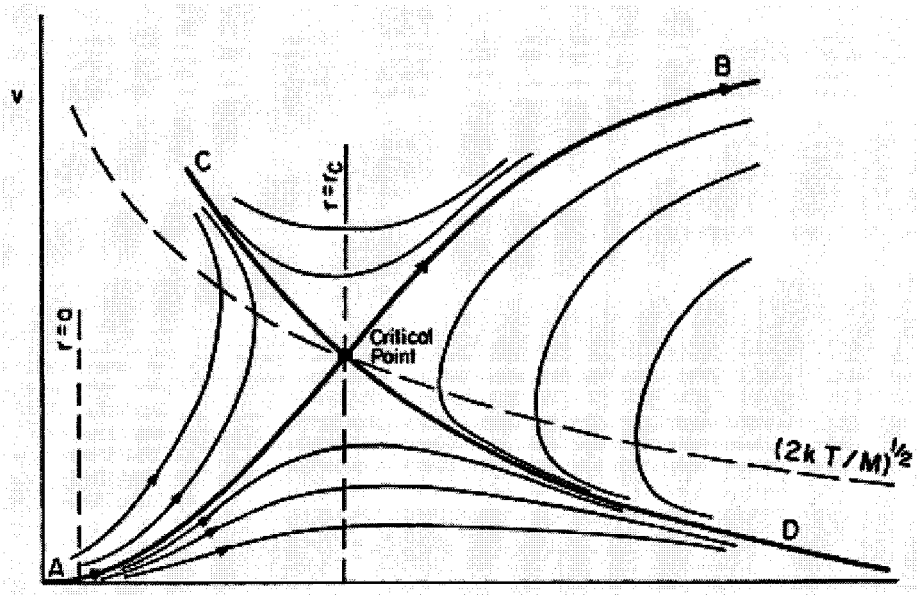

Chapter 2

Numerical Methods

2.1 Computational Engine

2.1.1 Overview of numerical methods

Before describing the numerical code used in this work, I want to place it in the wider context of the art of computational fluid dynamics (CFD).

2.1.1.1 General overview and classification

CFD methods can be classified according to the locality of treatment of the computational volume, starting from those that treat the volume globally and ending with methods that deal at a (pseudo)-particle level.

Spectral methods

In spectral methods, a set of field functions f_i is defined, and flow quantities are approximated by linear combinations of these functions. The duty of the numerical method is then to find the coefficients of these linear combinations. These methods treat the flow without breaking the volume into cells, and therefore are very global in character.

It is often recommended to choose the f_i so that the boundary conditions (BC) are fulfilled automatically; this can be done (in principle) if the BC are linear. Another recommendation is to use a set of functions already known to be similar to the expected solutions, for instance by using the known solutions of a simplified version of the problem. Frequent choices for the expansion functions are:

Sines and cosines (Fourier basis) This has the advantage that space derivatives are easy to calculate (sines and cosines are eigenfunctions of ∇^2), there is access to the FFT technique (which is convenient for treating the non-linear terms), and the coefficients often have a direct physical meaning. It has the disadvantage that sharp features in flows produce ringing (the Gibbs phenomenon), and require many terms to be retained.

Chebyshev polynomials This basis is able to represent flows inside a computational domain, with a better treatment of sharp features than the Fourier basis. The fast Fourier transform is still available, because of the algebraic trigonometric definition of these polynomi-

als, $T_n(x) = \cos(n \arccos(x))$. Derivatives are still easy to represent using the recurrence relations.

The most impressive advantage of spectral methods is the extremely large Reynolds number that can be achieved. They have good treatment of smooth flows, but a rather poor treatment of non-linearities, and especially bad treatment of shocks. For linearized, smooth problems with simple boundary conditions, these are probably the best methods to use, giving high accuracy and low numerical viscosity with little computational cost.

The range of applicability of spectral methods can be widened by using a basis of appropriate wavelet functions, whose sharpness allows the description of sharp features in the flow. The equations usually don't have an exact solution in terms of an expansion in the subspace F generated by the basis functions f_i. There is a residual, which the method tries to minimize in terms of a set of test functions N_i. If these test function coincide with the basis elements, we have the Galerkin method, in which the error is declared to be orthogonal to the subspace F; this is the most usual approach, but it is not the only one.

Some non-spectral methods can be described using a spectral language. For instance, a set of splines subordinate to a splitting of the volume in cells can be a good choice of basis; but this good idea already makes the method more local and less global in character, and it is an example of the finite element method. In an extreme case, Dirac delta functions can be approximated by localized top-hat functions, centered at points in the flow; this is equivalent to the finite-difference method.

An example of usage of the method in an astrophysical contex can be seen in Marcus (1988); general references can be seen in Gottlieb & Orszag (1977) and Canuto et al. (1987).

Finite element methods

These methods are intermediate between finite difference and spectral methods. There is a grid, as in a finite difference method, which can be either structured or unstructured.[1]

At each mesh location, a localized functional shape or set of functional shapes sharing a finite support are defined. Flow quantities are then described in terms of these functions, instead of sample values at the mesh points as in a finite-difference description. Finite elements are strongly recommended for problems with boundary conditions with complex geometry. The grid can be chosen to adapt to those boundaries, especially if an unstructured mesh is chosen. This is the reason it is the most popular method to study practical CFD in aeronautics.

[1] Computational meshes can be called structured, when their topology is defined from a coordinate system, and unstructured, when the topology is defined ad-hoc (it might even be time-dependent), requiring an explicit data structure containing topological information such as the list of vertices corresponding to a cell and the list of its next neighbors. Structured grids, being easier to keep track of, are more commonly used. On the other hand, mesh refinement or higher dimensionality Lagrangian methods are more efficient when coded using an unstructured mesh.

Finite difference methods The basic idea of these methods is probably the most intuitive. A grid is defined, and the flow quantities are represented by values defined only at the grid points. The derivatives appearing in the fluid dynamic equations are represented by differences (hence the name of this family of methods), and the integrals by sums. The numerical representation of first derivatives might be by as little as two points, making the error first order in the spacing Δx, or it can be by more points, so as to reduce the truncation error to a higher order.

In finite-differencing, better physical results are found in methods that try to keep track of flow-conserved quantities, such as mass, momentum, angular momentum and energy. This is done by setting up volume control cells around the grid points, estimating the total value of the conserved quantity on each such small volume —for instance, the total energy—, calculating the expected energy flux between the volume interfaces, and use only those fluxes to calculate the advection of energy. This is one reason why it is convenient to write the equations in divergence form prior to finite differencing them: the fluxes become explicit in the equations. The various grid setups used in finite differencing can also be ordered from most global to most local. Here are some of the most common examples:

Eulerian grid These are grids fixed in space and time, over which the equation is differenced, following the Eulerian form of the fluid equations. It is usually simpler to code than other grids, and does not incur computational overheads of grid updating. They are best for problems where the location of the regions of interest and boundary conditions are known beforehand, or when evolving the grid would produce an unacceptable overhead in computer or programming time.

Moving Eulerian grid These grids are topologically fixed, but are allowed to move in space according to the motion of the regions of interest, tracking for instance the bulk motion of the flow or the location of a sharp variation.

Adaptive Eulerian grids Obviously there is an advantage in having more detail in the regions of the flow where more complex phenomena occur. This can be done by changing the grid during run-time. Two popular approaches to this are grid refinement and grid nesting. In grid refinement steps, points are added to the grid at run-time in regions where more precision is looked for; de-refinement steps are also needed to subtract points that have fallen out of the "spotlight". In grid nesting, temporary, finer grids are created inside a global, coarser grid, and evolved using a finer time-step than the rest of the flow. These methods produce a very accurate representation of the flow, and are recommended when sharp shocks, whose locations can't be predicted, dominate the flow. They are expensive in computational time, though, because the finer grids or refined space intervals require a finer time step Δt to be both precise and stable.

Lagrangian grid Here the grid follows the fluid elements, using the Lagrangian description of the fluid. Mass conservation is (in principle) automatically ensured. Moreover, following the fluid elements has the advantage that a region undergoing a sudden compression gets automatically refined by the natural motion of the fluid elements. This is the grid method of choice in 1-D problems, such as the simulation of a spherically symmetric star or supernova, a point blast, or a problem with 1-D plane symmetry. In a higher and more realistic dimensionality, flow motion distorts the shape and even the topology of the grid cells. The usual work-around for this problem involves doing a periodic remap to an Eulerian grid. Another solution involves working with a Lagrangian adaptive grid, which will split cells that become too ill-shaped, and will keep track of topological changes at run-time.

Particle methods An even more local description of the fluid than using a Lagrangian grid is done by representing it by a set of N particles, and studying an appropriately modified N-body problem to evolve the flow. These are often called *pseudo*particles, when there is need to distinguish them from the authentic particles in the flow.

Each particle has information on its position $\mathbf{x}_i$, its velocity $\mathbf{v}_i$, its mass m_i, a local value of the pressure or of the internal energy, and of other fields (e.g. $\mathbf{B}$, $\mathbf{j}$) as needed.

Each computational particle used represents a region of the flow, with an extent and shape described by an interpolating kernel function W_i. The method is usually called SPH (Smooth Particle Hydrodynamics).

Frequent applications of SPH are to galactic dynamics, electrostatic plasmas, and other systems where there is a large density dynamic range. The low-density regions are relatively unimportant for the dynamics, and the particle description will naturally de-emphasize them.

With the local value of $\mathbf{v}_i$ in hand, updating the position $\mathbf{x}_i$ is easy enough; the difficult step lies in the calculation of forces on the particles, especially if they are long range. If the number of particles is small, it is possible to calculate the force by adding all the interactions between pairs of particles. The number of these interactions grows like N^2, which is computationally too expensive.

Two techniques used to overcome this limitation are:

Particle-in-cell (PIC) A mesh is set up for the purpose of storing information that permits the calculation of long-range forces at mesh points (for instance, by solving the Poisson equation in the case of electrostatic or gravitational forces). These mesh-valued forces are applied to each particle that happens to lie there. The method as defined here (Particle-Mesh, PM in short), has the disadvantage that the departures from the average, coming from next-neighbor

forces, are disregarded. It is however good enough for non-collisional problems.

If the system is collisional, this method can still be used if we split the force between a contribution from a few nearest neighbors, which will be calculated exactly and a contribution from further away particles, which is calculated in an average way. The resulting method is called P^3M, because the particle-particle interactions are taken into account together with the smooth particle-mesh part.

The identification of nearest neighbors can be done by using another, coarser mesh; particles belonging to the same cell (or nearby cells) are considered to be next-neighbors. This particle identification step is however computationally expensive, and difficult to parallelize; so it is not usually done every time step.

Tree methods These methods also split the force into one between nearest-neighbors and an average force term, but without using a mesh to calculate them (Hernquist & Katz 1989). Instead, a tree data structure keeps information on the relative location of the particles. At the root node of the tree, all particles are present. Successive branches include groups of closely connected particles, until the leaf nodes, which contain only the closest neighbors. These are used to calculate the local forces exactly; wider levels in the branching are used to calculate average forces with varying degrees of precision, which can be tailored to balance computational accuracy and efficiency. Creating and updating the tree is also a relative expensive task, which is not done exactly every time step. For the benefit of parallelization, some tree methods do a frequent approximate update (every few time steps), followed by a less frequent full redraw of the tree to prevent it from becoming too inexact.

2.1.1.2 Some necessary techniques and concepts

In the following I will describe some techniques applicable to some or all numerical methods, concentrating on those effectively employed in this thesis.

Treatment of time dependence When solving a time-dependent equation of the form

$$\frac{\partial u(\mathbf{x},t)}{\partial t} = A(u,\mathbf{x},t) \ , \tag{2.1}$$

time dependence can be treated either *explicitly* or *implicitly*.

Explicit methods Here already known values of the field u are used in the numerical representation (for instance, finite-differencing) of the right-hand side. These values are used then to update u. This algorithm is usually first order in time; in some favorable circumstances,

such as those of the *leapfrog method*[2], it can reach second order.

Implicit methods Here the numerical representation of the operator A is done using both the present value at time-step n, and its future value at the next step $n+1$. For instance, equation 2.1 can be represented in an implicit method by

$$\frac{u(\mathbf{x}, t_{n+1}) - u(\mathbf{x}, t_{n+1})}{\Delta t} = A(u(t_n), u(t_{n+1}), \mathbf{x}) \ , \tag{2.2}$$

where at least some of the appearances of u in the operator A use the unknown value $u(t_{n+1})$. Finding $u(t_{n+1})$ requires solving an algebraic equation, which will be more or less complex depending on the operator A. These methods are inherently higher order in time, but tend to have better numerical stability; both features allow them to work with larger time-steps Δt. However, they incur the extra costs of having to solve an extra operator equation per timestep (which also complicates coding), and having to store both $u(t_{n+1})$ and $u(t_n)$ in the computer memory, which can also be a limitation when using very fine grids.

Numerical stability

It has been known for a long time (von Neumann & Richtmyer 1950; Richtmyer & Morton 1967) that many numerical methods can become unstable if they are not treated properly. That is, the output of the method can grow exponentially from a small perturbation, even when the underlying physical system would be stable or grow at a much slower rate. For simple systems it is possible to do a full stability analysis: the difference representation of the differential equations is linearized around an equilibrium solution, assuming a small perturbation around it. The growth rate of the perturbation can be found from an eigenvalue problem, and it is of course desired that it be at most 1. For more complex systems, this stability study is not done directly, but the experience obtained from simpler problems can be used.

In grid methods, stability of the advection terms often depends on the Courant number (Courant, Friedrichs, & Lewy 1928), roughly defined as $C = v\Delta t/\Delta x$, where Δt is the timestep and Δx is the grid spacing, and v is the largest speed of transmission of information, such as a flow speed, a sound speed or an Alfvén speed as the case may be. Stability of good explicit methods requires C to be smaller than a value of order unity. Fixing the desired C to some reasonably safe value such as 1/2 or 1/10 fixes the maximum Δt available to the method for a given grid spacing. From this we see that using a grid finer by a factor of 2 requires the simulation to run for a time larger by a factor of 16, because the time step must also contract.

[2]The leapfrog method consists in time-staggering the positions and velocities, so that velocities correspond to half a time-step after the positions. This can be combined with space-staggering in a grid.

Unconditionally stable methods are those not formally required to satisfy the Courant condition, remaining stable for all values of C, no matter how large, allowing larger values of Δt. Some implicit methods are known to be unconditionally stable in this sense; however, using too large a value of Δt of course harms the accuracy of the method, and it is not too surprising to find that keeping C on the order of unity or smaller is often a condition for accuracy here as well.

Finally, a method can be so defective as to be unconditionally unstable, so that no matter how small C is, numerical instability will appear. This often happens in grid treatments of the advection equation, where the $(\mathbf{v}\cdot\nabla)u$ term can be treated in different ways. In doing this gradient in finite differences, it is possible to use centered differences ($\Delta x_i^{-1}(u_{i+1}-u_{i-1})$, in a 1D problem), upwind differences ($\Delta x_i^{-1}(u_i-u_{i-1})$, in a 1D problem with $v_i>0$), downwind differences ($\Delta x_i^{-1}(u_{i+1}-u_i)$, in this same example), or combinations of the above. Downwind differencing of advection terms should never be used in practice, because the method becomes unconditionally unstable (Fletcher 1990). The simple upwind differences are stable. They introduce an extra element of diffusivity to the equation, akin to an artificial viscosity, which can be either desirable or undesirable, depending on the case. Centered differences are higher order in a Taylor expansion in powers of Δx, and they are therefore more accurate and less diffusive. It is a trade-off in each particular case if their more restrictive stability is tolerable. It is possible to combine these two virtues of accuracy and stability: that is shown below when treating shock-capturing methods.

Treatment of shocks in the various finite-difference methods

Representing a shock numerically requires additional care. It is necessary that the numerical scheme produces the correct Rankine-Hugoniot jump conditions, the correct front propagation speed, and conserve energy, momentum, and magnetic flux with sufficient accuracy.

Shocks can be treated by *shock resolution*, for instance using an adaptive grid, or *shock tracking*, which detects the presence of a shock and applies the shock boundary conditions directly to the cells where a shock is detected.

The preferred approach nowadays is *shock-smearing*, or *capturing*. In these methods, the shock is purposely diffused so as to make it a few zones wider in its numerical representation than in reality. To do that, the method imitates the physics, where real shocks are resolved on the basis of physical dissipation, using a well-designed artificial dissipation scheme, so that only shock regions are affected by the artificial diffusive effects. Numerical viscosity is usually seen as an enemy of the accuracy of simulations, reducing the achievable Reynolds number and the reliability of the method. However, in an authentic compact with the Devil, here an artificial diffusivity is imposed on the flow with the intention of improving the treatment of shocks and

the stability of the numerics. This artificial viscosity must be non-linear, so as to increase in shocked regions. The most usual choice (Richtmyer & Morton 1967) for an explicit artificial viscosity term has it growing as some power of the gradient of velocity. Ideally, artificial viscosity should be small and irrelevant in a smooth flow, but strong near shocks to smear them for a few grid cells (such as two or three, which is usually sufficient).

An explicit artificial viscosity alone can be enough to treat shocks. However, more and better can be done. In the calculation of fluxes between computational cells, it is necessary to interpolate some of the flow quantities at the interfaces between the cells (the fluxes will later be used to update the flow quantities in a conservative way). In doing the interpolations, it is desirable to use methods that combine a high-order accuracy in the smooth flow, with a lower order method in the shock regions. Upwinding improves the stability of the method, by following the direction of causality properly. It may also be desirable to have a method to reduce unphysical noise, such as ringing; that is done for instance by using *monotonizers* (other linear and non-linear filters of high-frequency noise are also used). Both monotonization and upwinding are diffusive; sometimes so much that there is no longer need of an explicit artificial viscosity.

Various upwinding methods differ in the order of the interpolation being used. At lowest order, there is the simple donor cell method, in which the upwinding is done simply by choosing the value of the variable being updated in the upstream direction. This method is very highly diffusive, too much to be accurate. Better are higher order schemes such as van Leer upwinding and monotonization (van Leer 1979), and the interpolator defined in PPM method (Colella & Woodward 1984).

Once the interpolated values are found, they can be used directly in an advection step; this is a simpler procedure, which is often good enough, especially if a price is paid by increasing the number of grid zones. This is done in the ZEUS code (Stone & Norman 1992).

In modern shock-capturing methods, designed to handle sharper shocks at a lower computational cost in grid resolution, this is not enough. The results from the interpolation step give a flow profile which is not used directly, but instead used as initial conditions to find the flows, using some prescription based on the physics of the problem. This becomes necessary for instance in relativistic flows.

For example, using Godunov methods, a Riemann shock problem is solved at each cell interface; the flow obtained from that shock problem is then used in the updates. Different Godunov methods differ in the order of the interpolator, the kind of monotonizer or other non-linear filter used, and the construction of the Riemann solver itself, which is either exact or approximate. We have for instance Godunov's original method Godunov (1959), which uses

simple (first order) upwinding; van Leer's method (1979, using second order upwinding and a monotonizer; Colella and Woodward's (1984) Piecewise Parabolic Method, using higher order interpolation by approximating the flow variables by parabolic arcs; ENO, which uses a less drastic monotonizer than the previous schemes, with the intention of reducing clipping of the peaks of authentic waves (Harten et al. 1987), and many others. Godunov methods do not as a rule require explicit artificial viscosity; they take care of their own dissipation. The use of a Riemann solver makes the methods inherently upwind, because they use locally the shape of a solution of the shock equations. A review and tutorial on Godunov methods, written by Manzini (1994), can be found as an interactive book on the WWW.

All the methods above succeed by purposefully reducing the order in the shock zones. In flux limited schemes, we start (in 1-D) from a conservation equation of the form

$$\frac{\partial w}{\partial t} = \frac{\partial}{\partial x} f(w) \ . \tag{2.3}$$

Using a grid x_i, with spacing Δx_i, a discretization of this equation in flux form is

$$w_i^{n+1} = w_i^n - (F_{i+1/2} - F_{i-1/2})/\Delta x_i \ , \tag{2.4}$$

where $F_{i+1/2}$, the numerical flux, is a numerical approximation to the value of f at the cell interface $x_{i+1/2}$, integrated along the timestep going from t_n to t_{n+1}. Two possible values for the flux are considered; a diffusive but numerically stable flux $F^L_{i+1/2}$, based on a low-order upwinding, and a more precise flux $F^H_{i+1/2}$, based on a higher order calculation, which has some risk of instability, and their difference $A_{i+1/2}$, called the antidiffusive flux. A combination of both, $F_{i+1/2} = F^L_{i+1/2} + C_{i+1/2} A_{i+1/2}$, will be finally be applied to evolve the w_i. For instance, in the Flux Corrected Transport method, the lower order flux is used first to construct a reference solution for the primitive variable w_i, which is then used to estimate how large C can be at each point, subject to the conditions $0 \leqslant C \leqslant 1$ and of keeping the solution from exceeding specified bounds in its maximum and minimum values. In smooth regions, C ends up being close to 1, while in shock regions it is close to 0. Other flux limiters are also used. A wide family of these methods are the so-called upwind flux limiters, following a classification scheme by Sweby (1984), as generalized by Zalesak (1987). These limiters calculate the quantity $C_{i+1/2}$ without previous knowledge of the other values of C. The lower order solution is not, as a rule, explicitly computed. The family includes Roe's Superbee method (1985), the PDM method (Hain 1978), and many others. Many Godunov methods (including the eponymous first-order Godunov scheme) can be written in an algebraic equivalent form as flux-limited methods, and therefore also belong to this family.

Operator splitting

Let's suppose we have a differential equation of the form

$$\frac{\partial w(x,y,z)}{\partial t} = A(w,x,y,z) + B(w,x,y,z) \ . \tag{2.5}$$

A finite difference representation of this may have the form

$$w^{n+1}_{i,j,k} = w^{n}_{i,j,k} + (A_{i,j,k} + B_{i,j,k})\Delta t^n \ , \tag{2.6}$$

where A and B may depend on both w^{n+1} and w^n in an implicit method, but only on w_n in an explicit one.

If solving both terms together is inconvenient, an operator split method consists on evaluating first the effects of the A term obtaining

$$w^{*}_{i,j,k} = w^{n}_{i,j,k} + A_{i,j,k}\Delta t^n \ , \tag{2.7}$$

and after this half-timestep is advanced, calculating the effects of B by doing

$$w^{n+1}_{i,j,k} = w^{*}_{i,j,k} + B_{i,j,k}\Delta t^n \ . \tag{2.8}$$

The numerical errors introduced this way can sometimes be reduced by exchanging the order of A and B on the following timestep.

This technique is often used to separate the source terms from the transport terms in the equation (the transport terms are often more difficult to treat). It is also frequent using it to evolve 3-D and 2-D systems one dimension at a time, instead of treating all three dimensions together. This technique of *dimensional split* allows the generalization of most 1-D schemes to 3-D, including some schemes whose direct 3-D usage would be cumbersome or impossible. The error introduced by dimensional splitting is small, of the order of the other truncation error terms already tolerated. Following tradition perhaps more that authentic testing, it is common to vary the order of the dimensions being updated on each timestep; this is expected to avoid dimensional bias and to improve accuracy.

Treatment of the magnetic field

The magnetic field is subject to a null-divergence constraint, which should be considered in evolving it.

Constrained Transport Probably the most direct approach to this problem is Evans & Hawley (1988) Constrained Transport method. In this method, the magnetic field is evolved in

such a way that no monopoles can be formed. The equation for the evolution of the magnetic field has the form $\partial \mathbf{B}/\partial t = \nabla \times \mathcal{E}$, with for instance $\mathcal{E}$ equal to $\mathbf{v} \times \mathbf{B}$ for an ideal MHD problem. The values for the electromotive force field $\mathcal{E}$ are first found in all the computational volume, and their numerical curl is found, and used to update $\mathbf{B}$. If the numerical curl is defined properly, its numerical divergence will be zero (up to machine round-off error). If the initial $\mathbf{B}$ field fulfilled the divergence constraint, its updated value will not depart from it. Implementation of this consistent numerical curl is done more easily by using a staggered grid. If we consider each grid point in a 3-D grid as the vertex of a small computational cube (corresponding perhaps to a small wedge in a spherical grid), the preferred staggered grid will have its vectors $\mathbf{B}$ and $\mathbf{v}$ defined on the faces of the cube, and the vector $\mathcal{E}$ on its edges.

Other methods The $\nabla \cdot \mathbf{B} = 0$ constraint can be taken care of also by other methods, that will be mentioned here with less detail than they deserve.

Evolve the B field components with a method that might produce some small divergence, then subtract a term cancelling this divergence out. This usually requires solving a Poisson equation.

Evolve only two of the three components of $\mathbf{B}$ in a 3D problem, and calculate the last component by solving the Poisson equation $\nabla \cdot \mathbf{B} = 0$. This method has the disadvantage that it concentrates the numerical truncation and precision errors into this last component.

Evolve the vector potential instead of the magnetic field. This idea may be particularly appealing in a 2-D problem, where one component of the vector potential often suffices. For an axisymmetric problem, the variables could be the flux function ψ and the component B_ϕ, which is free of divergence constraints when $\partial/\partial\phi = 0$. The disadvantages of this idea is that it requires a higher order in the numerical derivatives when calculating force terms. It becomes less convenient in 3-D.

A more risky approach consists in tolerating the presence of a non-zero $\nabla \cdot \mathbf{B}$, but making sure that it has no direct effects in the force term.

2.1.2 Description of ZEUS3D

The simulations presented here are based on ZEUS36, a parallel version of the code ZEUS3D. As the main numerical algorithm is unchanged, I start by describing the parent code, and in the next section I will describe the differences.

ZEUS3D is a general-purpose code for three-dimensional MHD, widely popular among the astrophysics community. Written by David Clarke (Clarke, Norman, & Fiedler 1994), it is presently

maintained by the LCA (Norman 1996), where the code can be obtained on request. Its easy availability and generality of scope amply justify its popularity. It is made all the more convenient by its good manual and excellent internal documentation.

2.1.2.1 Geometry of the code

ZEUS3D uses a 3D Eulerian mesh, in any of three geometries: cartesian, cylindrical and spherical. The structured grid is made out of three coordinate axes, called in a geometry-independent way `x1`, `x2` and `x3`, corresponding to either of cartesian (x, y, z), cylindrical (z, R, ϕ) or spherical (r, θ, ϕ). Each coordinate axis has associated with it a main 1-D grid, called the `a` grid, located at the edges between the computational zones, and a secondary grid `b`, located at the zone centers; this is done to allow staggering of the different flow fields, as explained below. Each of the main 1-D grids can move in space independently, allowing some motion to the Eulerian mesh (however, as this feature was not found useful for the problems we studied here, it has not been maintained in ZEUS36).

Each axis extends between a minimum and a maximum active value, assigned by the user at grid-creation time. Beyond these active values, a few non-active values are required for the purpose of taking care of boundary conditions.

The grid is staggered so that

$$\mathtt{x1a}_i < \mathtt{x1b}_i = \frac{\mathtt{x1a}_i + \mathtt{x1a}_{i+1}}{2} < \mathtt{x1a}_{i+1} \ ; \tag{2.9}$$

we may then say that the `a` grid is centered at the index values i, and the `b` grid is centered at the index values $i + 1/2$. Most scalar fields are defined at zone centers, on the `b` grid, at the points $(\mathtt{x1}_{i+1/2}, \mathtt{x2}_{j+1/2}, \mathtt{x3}_{k+1/2})$. This includes the density ρ, the internal energy u, the Newtonian gravity field Φ_g, the pressure p, the divergence of the velocity $\nabla \cdot \mathbf{v}$, and many others. The vector fields $\mathbf{v}$ and $\mathbf{B}$ are defined at zone interfaces, so that the component `v1` is defined at the point $(\mathtt{x1}_i, \mathtt{x2}_{j+1/2}, \mathtt{x3}_{k+1/2})$, `v2` at the point $(\mathtt{x1}_{i+1/2}, \mathtt{x2}_j, \mathtt{x3}_{k+1/2})$, and `v3` at $(\mathtt{x1}_{i+1/2}, \mathtt{x2}_{j+1/2}, \mathtt{x3}_k)$; similarly for the magnetic components. The Constrained Transport method requires also the calculation of values of the field $\mathcal{E} = \mathbf{v} \times \mathbf{B}$; calculation of the Lorentz force may require the current $\mathbf{j}$. These two vector fields are centered at zone edges, at the locations $(\mathtt{x1}_{i+1/2}, \mathtt{x2}_j, \mathtt{x3}_k)$, $(\mathtt{x1}_i, \mathtt{x2}_{j+1/2}, \mathtt{x3}_k)$, and $(\mathtt{x1}_i, \mathtt{x2}_j, \mathtt{x3}_{k+1/2})$ respectively for the components in the three directions.

ZEUS3D can be used in a two-dimensional and even one-dimensional mode, by imposing appropriate symmetry flags. As a two-dimensional code, it is a descendent of ZEUS2D, written by James Stone (Stone & Norman 1992), and also presently maintained at LCA (Norman 1996).

2.1.2.2 Algorithm

The algorithm is explicit in time, using both operator and dimensional splitting. The transport terms of momentum are treated using *Consistent Advection*, by which the fluxes of momentum on each axis are obtained from the mass fluxes in the same directions (Norman, Wilson, & Barton 1980). Specific energy advection is treated similarly. The magnetic field is evolved using the *Constrained Transport* (CT) method (Evans & Hawley 1988), which guarantees a constant divergence of $\mathbf{B}$, set to zero initially by the user. Three different CT options are given, differing in their calculation of the EMF term $\mathbf{v} \times \mathbf{B}$, and in their treatment of the Lorentz force $\mathbf{j} \times \mathbf{B}$. In the simpler option, CT is implemented directly by doing an upwind estimate of $\mathbf{v} \times \mathbf{B}$, and the Lorentz force is simply treated as a source term in the equation of momentum conservation. This method, while essentially correct, may be too diffusive, smearing out the magnetic field being advected. The two other options are less diffusive, They implement a method of characteristics approach to the calculation of both $\mathbf{v} \times \mathbf{B}$ and the transverse part of Lorentz force; the longitudinal part is now treated as the gradient of a magnetic pressure. The two method of characteristic implementations, called MOC and HSMOC in the internal code documentation, differ technically in the way the upwinding is performed; it has been observed, however, that the older MOC can produce unphysical spikes in the magnetic field, especially when the field is passive, making HSMOC the preferred method (Hawley & Stone 1995).

At the beginning of each complete time step, the fields stored are ρ, $\mathbf{v}$, $\mathbf{B}$, u, and Φ_g. Each explicit time step starts by calculating the pressure field, and the three components of the momentum. The three components of the momentum are updated considering only the source terms in the force, but none of the transport terms; the terms considered are the gradient of pressure, gravity, and the Lorentz force (its longitudinal part or all of it, depending on the usage or not of the method of characteristics). Also the pseudoforces arising from curvature in the non-cartesian coordinate systems supported are updated during this source step. This partial update is of course an example of operator splitting of the whole equation. The velocities are then updated from the values of momenta. Artificial viscosity is then applied to the flow, updating velocities and the internal energy u. To finish the source step, the internal energy is updated, by taking into account the compressional heating $p\nabla \cdot \mathbf{v}$, and, for non-adiabatic problems, empirically defined cooling and heating functions. Values of the fields in the ghost zones are then found by using the boundary conditions set up by the user.

The transport step is in charge of calculating the advective terms, which are particularly prone to numerical instability. Upwinding becomes a necessity here.

The transport step starts by considering magnetic effects; first of all, the transverse components of the Lorentz force (if they had not been calculated before in the source step), and next the update of the magnetic field, based on values of $\mathcal{E}$, using the constrained transport method.

The three components of the momentum $\mathbf{s}$ are then calculated from ρ and $\mathbf{v}$. By using upwinding,

the mass flux in the direction 1 is obtained and used to update the local value of the density. The same is done with the specific internal energy u/ρ. The value of the mass flux is then used to calculate the flux of the vector $\mathbf{s}$ in the direction 1. This procedure is repeated in the other two directions. On succeeding timesteps, the order of the three directions will be changed, in the hope of diminishing the bias introduced by this dimensional split, so that if timestep 1 starts with an order 123, it will be followed by 213, 231, 321, 312 and 132. Once all the components of $\mathbf{s}$ are updated due to fluxes in all three directions, they are used to recalculate $\mathbf{v}$. The boundary conditions are used again to find ghost zone values, finishing the transport step.

All terms in the flow equations have now been accounted for, and all fields have been updated. But before starting the next timestep, the code needs to know the value of Δt to use. This is done by considering the Courant condition, so that Δt will not be larger than $c\Delta x/v$, where Δx is an estimation of the coordinate spacing; v is an estimation of the speeds of propagation of information, including the sound speed, the Alfvén speed, and the flow speed. The factor c is a safety parameter set by the user between 0 and 1. The timestep Δt also contains effects due to the artificial viscosity, and it is not allowed to grow larger than the older timestep multiplied by 1.26; but it is allowed to decrease by any factor (however, if the decrease is too steep, a warning is produced, and if too many such warnings are produced, simulation stops).

Once the size of the new Δt is known, the code checks if there are any I/O requests, and complies with them if present. The termination conditions for the simulation are also checked here. If they fail, the next timestep will start.

2.1.2.3 Input/Output

A multitude of output mechanisms are provided; however, most have not been included in the parallel version, so I will not go into their detail. They include full restart dumps, one and two dimensional plots and dumps along slices, rebinned volume dumps, 2D integrations along line of sight, values of selected scalars, and 3D HDF output files. Of the many output quantities included, I will mention first the main stored fields $\mathbf{v}$, $\mathbf{B}$, u, ρ and Φ_g, and also other quantities, such as the Mach number, the thermal and magnetic pressures, components of the current and of the momentum, and the divergence of $\mathbf{v}$ and $\mathbf{B}$.

Most user input is done while writing the initial setup of the problem (or adapting one of the sample initial setups provided with the code) and selecting the boundary conditions to use. It may also be necessary to edit two small files used by the precompiler, especially if there is a change in the problem being studied or in the number of elements used in the grids. Control of the parameters used by the code is done by editing the namelist file `inzeus`. Finally, ZEUS3D allows some variables to be modified by run-time input, which allow the modification of the termination conditions, or of the conditions to produce the different kinds of output.

ZEUS3D is distributed together with a powerful precompiler, specialized in working with FORTRAN77 code, called EDITOR. Also written by David Clarke (Clarke 1992), it is intended to facilitate the management of large FORTRAN projects.

The last released version of ZEUS3D is version 3.4, which can be obtained from LCA at the URL `http://zeus.ncsa.uiuc.edu:8080/lca_intro_zeus3d.html`.

2.1.3 Parallelization: ZEUS36

Parallelization requires distributing both the data and the tasks over a set of computational nodes. This distribution is straightforward for the case presented here, which is a fixed, structured Eulerian mesh: the computationally cubic grid is subdivided into N equal, smaller cubic grids, each given to one of the N computer nodes (independent processors in a parallel machine). Communication between the nodes is realized by taking advantage of the boundary condition subroutines, appropriately modified to allow communication between adjacent computer nodes. The equality of the subdivision guarantees *load balancing.*[3]

It was found convenient when doing the mesh subdivision to add one ghost zone more to the grid, which might improve the treatment of boundary conditions. More important for parallel usage, however, was making fully consistent the treatment of the corners and edges of the grid. Corners and edges are of less importance when the code is not run in parallel. They become more important in a parallel treatment, where they appear in the middle of the overall mesh rather than less obtrusively at the boundaries of the calculation, where the simulation has lowered reliability anyway. This also improved the performance of the code with periodic boundary conditions, which are subject to the same need for clean corners.

The user interface was modified to make it more convenient to our usage on many different computer systems, serial and parallel. For instance, it was decided not to use the powerful precompiler EDITOR (Clarke 1992), bundled into the ZEUS3D release. This precompiler is very powerful and versatile, but it is slower than the standard C precompiler, which was finally preferred. This change was also intended to eliminate the need to recompile the main code: only the specific problem setup should need recompilation. EDITOR 'decks' were replaced by include files, conditional compilation statements were replaced by either FORTRAN conditional statements, invocation of user-defined routines, or, as rarely as possible, C precompiler statements. These changes were helped by the use of dynamic memory allocation, which allows one to dispense with recompilation in the frequent event of grid size change.[4] Sadly, dynamic memory allocation is not a standard FORTRAN77 feature, and FORTRAN90 is not yet easily available in all parallel systems. Therefore, dynamic memory alloca-

[3] All computer nodes have the same computational load, minimizing the wait times involved when one node has to wait for another to complete its task whose result is needed elsewhere.

[4] And also in the less frequent event of being able to omit some array not needed for a particular problem, such as the energy density for an isothermal problem.

tion required going beyond the standards. The most convenient way consisted in using Cray-style pointers,[5] which allow explicit dynamic allocation of arrays whose pointers can then be passed along via the subroutine call interface or common blocks. Unused arrays can simply be omitted from the explicit allocation, reducing memory usage with no need for recompilation. However, not all FORTRAN77 dialects available had this useful feature; a conspicuous exception was GNU FORTRAN77 (g77), which is closer to standard compliance than most other compilers. For this case, a less obvious departure from ANSI FORTRAN77 standards was used, consisting in the usage of automatic arrays.[6]

Communication of data between the different nodes was done using MPI —a standard message passing interface for parallel machines, including networks of workstations. This makes ZEUS36 easily portable in the parallel computing world: ZEUS36 has been run on the historical Delta Touchstone, on Intel Paragon machines, on an HP Exemplar with 128 CPUs, and recently on a Beowulf system. The practical payoff of portability is great, especially given that the two first mentioned systems have already been decommissioned at Caltech. Experienced supercomputer users point out that all such machines only start to run smoothly by the time they are already obsolete.

2.2 Boundary Conditions

2.2.1 Boundary Conditions at the Accretion Disk

The launching problem will be studied here describing the accretion disk as a boundary condition —no attempt will be made to model or simulate the disk itself. This disk is also the main motor of the jet in the magnetocentrifugal mechanism, requiring extreme care in describing this boundary condition.

The first question to address is the number of boundary conditions we are allowed to fix at this surface. This was studied for instance in Bogovalov (1997), with the main intention of using the results for steady state, axisymmetric flows; but the reasoning is general.

The number of boundary conditions to fix is equal to the number of waves outgoing normally from the boundary, which is also equal to the number of characteristics outgoing from the same boundary (Kontorovich 1959; Landau & Lifshitz 1987). This can be calculated counting the degrees of freedom of the system, subtracting all constraints, and adding in the effects of the flow speed. There are, in principle, seven degrees of freedom: the density, three components of $\mathbf{v}$ and $\mathbf{B}$, minus the constraint $\nabla \cdot \mathbf{B} = 0$, and also the internal energy, because our simulation, while dynamically cold, keeps track

[5] Semantically very similar to the pointers used in C, even if their syntax is widely different.

[6] The three array dimensions are passed as integers to an allocator subroutine via either common blocks or the call interface. This subroutine then defines local arrays having these sizes. Subroutines downstream from there are able to read those arrays via the call interface. It may be a surprise to some FORTRAN users to know that this practice is not completely standard, and indeed some compilers (Absoft Fortran, Paragon) still do not allow it.

of a small internal energy. These degrees of freedom correspond to seven MHD waves: one entropy wave, and two Alfvén, two slow and two fast magnetosonic, waves. In a plasma at rest, the pairs of Alfvén and magnetosonic waves have opposite group speeds, propagating backwards and forwards from the interface, while the entropy wave has zero speed. In a plasma in motion, the speed of the plasma is added vectorially to the group speeds of these seven waves. At the $z = 0$ interface, the plasma speed v_z is added to the group speed in the normal direction. If this speed were positive, but slower than the slow magnetosonic speed, then the number of outgoing waves is four, counting the forwards Alfvén, the forwards slow and fast waves, and the entropy wave. Therefore, when studying the launching hot plasma undergoing the slow magnetosonic transition, it is necessary to fix four boundary conditions. In our problem, however, we are studying a cold plasma, cold enough that v_z is larger than the slow magnetosonic speed (projected on the z axis), but smaller than the Alfvén speed. In this case, both slow waves become outgoing, albeit at different speeds. The number of boundary conditions required is now five.

Strong geometrical restrictions such as axisymmetry or self-similarity impose strong limitations on the waves that can propagate. Axisymmetry is responsible for the importance for steady state flows of the fast and Alfvén surface defined in terms of the poloidal speed alone ($v_p = B/\sqrt{4\pi\rho}$ and $v_p = B_p/\sqrt{4\pi\rho}$ for a cold flow), independent of v_ϕ. Self-similarity limits wave propagation to the self-similarity direction chosen.

It is interesting to observe that the proper number of boundary conditions can also be found in an axisymmetric, steady state problem by subtracting one independent quantity per crossing of a critical surface, which in steady state is also a constraint that removes a degree of freedom. In principle there are three such surfaces, slow, Alfvénic and fast; however, in our simulations, the initial poloidal v_p at $z = 0$ is already larger than the slow speed, so only two critical surfaces can be crossed. Five independent waves are left out of the original seven, and so five boundary conditions should be imposed, agreeing with the more general argument above.

In some simulations (e.g. Ouyed & Pudritz 1997b; Meier et al. 1997) more BC are imposed at the disk than allowed by the above description. In that case a boundary layer may appear between the disk surface and the wind, where the quantities readjust discontinuously.[7] Typically, this produces localized kinks in the poloidal fieldlines, associated with abnormally high values of j_ϕ. Also locally impulsive forces may appear, which change the flow substantially between the first few active zones in the grid and the intended boundary conditions. Artificial, locally impulsive forces are particularly dangerous when studying a naturally powerful acceleration mechanism, because they cast doubts on the authentic origin of the acceleration. The disk parameters do not control directly the simulation of the wind, because they may be masked by the boundary layer.

[7]The boundary layer might be absent if the BC imposed happen to match the values physically given by the flow evolution. The only practical case where this is possible is in finding stationary solutions by a shooting method.

In an alternative presentation, it has been argued, for instance by Meier (1998), that the disk may be resilient to react to information propagating backwards from the wind, due to its higher matter density, so that fixing a larger number of boundary conditions at the disk is justified on physical grounds. In particular, the angle between the fieldlines and the disk would be fixed by the disk alone, with no wind intervention. This does not seem to be the case, due to the arguments mentioned above. But, assuming for a moment that it is the correct picture, the interface between the disk and the wind will naturally present the sharp variations and large curents mentioned, which a simulation of the boundary layer region above the resilient disk should try to resolve by increasing the resolution, describing the strong forces associated with the proposed transition instead of representing them in a numerically impulsive way.[8] There is a simple interpretation that allows the simulations presented here to adapt to this picture. In this resilient-disk picture, it is possible to find a relatively small altitude above the disk surface where the quantities are again smooth. This altitude, which we may call the base of the wind, can be used as a launching surface in the simulations, and it will be sensitive to backward propagating waves, even if the disk is considered resilient to them. By considering that the effective BC is defined at this base of the wind, the simulations presented here keep validity in both pictures, with the only difference of replacing all references to the disk surface by a small altitude above it.

Once the flow leaves its launching region, it will finally encounter the outer edges of the computational box. The boundary conditions here are difficult to represent properly, because we have no authentic information on the outside flow. Different guesses have been proposed in this outflow region, mostly trying to reduce unphysical effects such as wave reflection on the box boundaries; however, no matter what is done, the issue remains that these are guesses and not real knowledge of the outside flow, especially when out of steady state. However, if the flow is already super-Alfvénic when it reaches the box surfaces, the influence of these outer boundary conditions is substantially reduced, and it is possible to relax some of the care required in their treatment. The usage of simpler outer boundary conditions is then allowed. Fortunately for the problems studied here, most or all of their outer boundary surfaces are super-Alfvénic.

When using cylindrical coordinates, two purely geometric boundary conditions also appear: the azimuthal boundaries at $\phi = 0$ and 2π, and the inner radial boundary condition at the axis $R = 0$. These are both easy to treat geometrically, the first by periodicity, and the second using rotational symmetry.

[8] No simulation up to the present has achieved enough resolution to do this kind of study in this region with sharp gradients of density, and, inside the present assumption, with large currents. Probably the closest would be Miller & Stone (1997).

2.2.2 Numerical implementation

In these cylindrical simulations the computational grid has at most six boundaries: axis ($R = 0$), outer radius ($R = R_{\max}$), disk ($z = 0$), outer height ($z = z_{\max}$), and inner and outer azimuth ($\phi = 0,\ 2\pi$). The last two obviously disappear in a 2-D axisymmetric study.

The ZEUS code enforces boundary conditions by assigning values to the fields ρ, u, $\mathbf{v}$, and $\mathcal{E}$ at the grid edge and at a few ghost zones beyond the edges of the active the computational grid. In each coordinate direction, there are up to three ghost zones to each side, continuing both the a a and b grids described in §2.1.2.1 or in Stone & Norman (1992).

The boundary conditions for $\mathbf{B}$ are enforced indirectly from the values of $\mathcal{E}$, using the equation $\partial\mathbf{B}/\partial t = \nabla \times \mathcal{E}$ to evolve $\mathbf{B}$ in both active and ghost zones, ensuring $\nabla \cdot \mathbf{B} = 0$ everywhere; this indirect treatment of the magnetic boundary conditions is required by the Constrained Transport method to avoid formation of numerical monopoles.

2.2.2.1 $\phi = 0$, $\phi = 2\pi$

These two boundaries are very easy to treat, by enforcing the periodicity $f(\phi) = f(\phi + 2\pi)$ for all fields f. When working on a parallel computer, and there is more than one node spanning the azimuthal range, this requires communication between the first and the last computer node in the ϕ direction.

2.2.2.2 $R = 0$

The axis boundary is geometrically well-determined by symmetry, and it presents no complications either in implementing or running. The conditions are implemented as usual for the axis in cylindrical coordinates, by observing the result of rotating the model by 180°, which should be equivalent to a change of sign in R. This implies that in the calculation of ghost zone values for $R < 0$, scalar fields f are reflected ($f(R) = f(-R)$), and components of vectors $\mathbf{A}$ are reflected with a change of sign for the R and ϕ components ($A_z(R) = A_z(-R)$ as the scalars, but $A_R(R) = -A_R(-R)$, and $A_\phi(R) = -A_\phi(-R)$).

2.2.2.3 $z = z_{\max}$

The upper boundary is treated by using an outflow boundary condition, as defined in the ZEUS3D code. Specifically, for $z > z_{\max}$ $A(z) = A(z_{\max})$ for all fields, except for $v_z(z) = \max(v_z(z_{\max}), 0)$. This is not perfect, but, as the physics of the model implies the existence of a supersonic, super-Alfvénic accelerated outflow, these imperfections are not expected to have a large influence in the simulated flow.

2.2.2.4 $R = R_{\rm max}$

This is more delicate, especially for some of the simulations, where the flow at small heights above the disk is sub-Alfvénic, and can influence the upstream flow. In practice we use similar outflow conditions as for $z = z_{\rm max}$. If there is a fieldline that becomes trans-Alfvénic only at the box edge $R = R_{\rm max}$, such as $\Psi = \Psi_1$ in the axisymmetric simulation shown in Fig. 3.1, it is clear that artificial conditions imposed at $R = R_{\rm max}$ for $\Psi > \Psi_1$ may induce spurious collimation. In the present treatment, it becomes necessary to explore the sensitivity of the results to the treatment of this part of the boundary. (cf. §3.3).

In one example of an alternative prescription, Romanova et al. (1997) have used a "force-free" prescription, $\mathbf{j}_p || \mathbf{B}_p$, that can be written as $\mathbf{B}_p \cdot \nabla(RB_\phi) = 0$; a later proposal from the same authors is taking $\mathbf{B}_p \cdot \nabla(RB_\phi) = \alpha B_R B_\phi$, with α a constant to be determined (Ustyugova et al. 1999), observing that artificial collimation may occur for inappropriate box sizes.

2.2.2.5 Disk Surface at $z = 0$

Even more important is the treatment of $z = 0$. It represents the launching surface of the model, located at the top of the disk, or the base of the corona, above the slow magnetosonic surface. Its properties will determine all the flow downstream.

As explained above (§2.2.1), the number of BC to fix is five. We chose to fix the five fields ρ, u, $\mathcal{E}_\phi$, $\mathcal{E}_R$ and v_z at the disk —if launching were sub-slow, the presence of the slow critical surface would reduce the number of independent boundary conditions to the first four. At $z = 0$, the boundary conditions for $\mathcal{E}_\phi$ and $\mathcal{E}_R$ are derived from the infinite conductivity of the disk material, giving $\mathcal{E}_\phi = 0$ and $\mathcal{E}_R = R\Omega B_z$. The condition for $\mathcal{E}_\phi = (\mathbf{v}_p \times \mathbf{B}_p) \cdot \hat{\phi}$ implies that $\mathbf{v}_p || \mathbf{B}_p$, $v_R/B_R = v_z/B_z = v_p/B_p$. The condition for $\mathcal{E}_R = v_\phi B_z - v_z B_\phi$ implies that $v_\phi = R\Omega + B_\phi v_p/B_p = R\Omega + B_\phi v_z/B_z$. Implementation is done by assigning values to fields at the ghost zones $z \leqslant 0$. Density, velocity and internal energy are defined at the ghost zones as straightforward functions of R, with $u = \rho c_{s0}^2/(\gamma-1)$ for a small constant c_{s0}. This fixes the mass flux ρv_z; if our launching were subsonic, this quantity should be determined from the crossing of the slow critical surface.

The magnetic field evolves in time following $\partial B_z/\partial t = R^{-1}\partial R\mathcal{E}_\phi/\partial R$, $\partial B_R/\partial t = -\partial \mathcal{E}_\phi/\partial z$, and $\partial B_\phi/\partial t = \partial \mathcal{E}_R/\partial z - \partial \mathcal{E}_z/\partial R$. Fixing $\mathcal{E}_\phi = 0$ at $z = 0$ allows us to keep a constant $B_z(R)$ at the disk surface, anchoring the field lines to the disk. The angle $\theta = \arctan(B_R/B_z)$ between the lines and the vertical should be allowed to change in time, because otherwise the fieldlines might get sudden kinks at $z = 0$, associated with large currents and localized forces. This requires a $\mathcal{E}_\phi(z)$ dependence allowing B_R evolution. We demand that $\mathcal{E}_\phi$ be odd in z, so that it vanishes on the disk $z = 0$. Time dependence of B_z becomes odd in z, and that of B_R even. The final inclination θ of the field line is decided by the flow itself and its crossing of the critical surfaces, producing a much better

steady state than alternative approaches in which the fieldline inclination is fixed. Similarly we make $\mathcal{E}_R(z)$ symmetric around its known value at $z = 0$, defining $\mathcal{E}_R(z) = 2R\Omega(R)B_z(R) - \mathcal{E}_R(-z)$ for $z < 0$. (An alternative possibility here would be extrapolating the fieldlines inside the ghost zones; however, this is somewhat more difficult to implement.) With this choice, one term of the time dependence of B_ϕ is even in z. We make the other term also even, by requiring $\mathcal{E}_z(z) = \mathcal{E}_z(-z)$, which allows this quantity to vary freely. Finally we need values for v_R and v_ϕ. We will take them from $v_R = B_R v_z/B_z$ and $v_\phi = R\Omega + B_\phi v_z/B_z$, which we implement using the values of B_z and Ω at $z = 0$. Following the variation of these quantities inside the ghost zones is also a possible option.

In simulations that present a finite disk of radius R_D (such as those in chapters 4 and 5), it is necessary to set the functions $v_z(R)$ and $B_z(R)$ to zero for $R > R_D$. The $z = 0$ boundary conditions for $R > R_D$, ouside of the finite disk, must be modified. This is done by obtaining ghost values for $z \leqslant 0$ of ρ, u, v_ϕ and v_R from their values at the first active zone with $z > 0$, and assigning the ghost values for v_z to zero.

In some simulations —early in the run of the simulation, long before steady state is approached— v_z becomes negative at the first active zone close to the disk. In that case the boundary conditions are modified, allowing the disk to absorb the backflow, thus preventing the numerical artifacts shown in §2.2.3. This is implemented by temporarily assigning ghost values at $z \leqslant 0$ for the fields ρ, u, v_R, v_ϕ and v_z in the same way described in the previous paragraph. [9] With this prescription, backflow is absorbed, and eventually disappears.

In most of this thesis the mass flux $j = \rho v_z$ has been prescribed as a function of R alone, although mass loading is effective only for $\theta \gtrsim 30°$. However, in the steady state simulations presented here this inequality is satisfied for most of the disk outside the innermost region, justifying the choice of disregarding θ dependence in these cases.

The functions of radius are parametrized using a combination of exponents and softening radii:

$$\rho(R) = \rho_0 / \sqrt{(1 + (R/r_\rho)^2)^{e_\rho}} \tag{2.10}$$

$$B_z(R) = B_{z0} / \sqrt{(1 + (R/r_b)^2)^{e_b}} \tag{2.11}$$

$$v_z(R) = (v_{z\text{inner}}^\nu + v_{z\text{outer}}^\nu)^{1/\nu} \tag{2.12}$$

$$v_{z\text{inner}} = \frac{v_{z0} / \sqrt{(1 + (R/r_{vi})^2)^{e_{vi}}}}{\sqrt{(1 + (R/r_{vo})^2)^{e_{vo}}}} \tag{2.13}$$

$$v_{z\text{outer}} = (f_{vo} R\Omega(R)) / \sqrt{(1 + (R/r_{vo})^2)^{e_{vo}}} \tag{2.14}$$

$$\tag{2.15}$$

Exponents $\nu = 1$ (linear) and $\nu = 2$ (quadratic) were used. For large R, $v_z \propto R^{(e_{vo}+1/2)} \equiv R^{-e_v}$, $j \equiv \rho v_z \propto R^{-(e_v+e_\rho)} \equiv R^{-e_j}$, and $\Psi \propto R^{-(e_b-2)} \equiv R^{-e_\Psi}$.

[9] In some simulations, however, the internal energy was set to $u = \rho c_{s0}^2/(\gamma - 1)$ in the backflowing ghost zones; given that these simulations are remarkably cold, this is a small detail that made no dynamical difference.

For finite-disk problems, the functions $B_z(R)$ and $v_z(R)$ must go to zero for $R > R_D$, taking care that their ratio must be kept finite, because it is used in the boundary condition for v_ϕ. This is performed by multiplying both of them by a continuous function $f(R)$ which softens the transition to zero by spreading it out over some interval. The most frequent choice was an arc of a cubic spline,

$$f(R) = \begin{cases} 0 & \text{if } R > R_D \\ (R-R_D)^2\left[\frac{1}{(R_{D1}-R_D)^2} - 2\frac{R-R_{D1}}{(R_{D1}-R_D)^3}\right] & \text{if } R_{D1} \leqslant R \leqslant R_D \\ 1 & \text{if } R < R_{D1}\ , \end{cases} \tag{2.16}$$

which spreads the transition smoothly over the interval $[R_{D1}, R_D]$.

The boundary condition for v_ϕ defined above needs a definition of the Keplerian speed $v_K \equiv R\Omega$ to be complete. This has been taken from the softened Newtonian gravity field

$$\Phi_g = -\frac{\Omega_0^2 r_g^3}{\sqrt{r_g^2 + z^2 + R^2}}\ , \tag{2.17}$$

with Ω_0 and r_g fixed parameters. The product $v_{K0} = \Omega_0 r_g$ gives the scale of Keplerian speeds, so that

$$v_K = R\Omega_0\left[1 + \left(\frac{R}{r_g}\right)^2\right]^{-3/4} \tag{2.18}$$

$$= v_{K0}\frac{R}{r_g}\left[1 + \left(\frac{R}{r_g}\right)^2\right]^{-3/4} \tag{2.19}$$

at the launching surface $z = 0$. The critical angle θ_c for this smoothed gravity is given by $\tan^2\theta_c = 1/3 + r_g^2/R^2$, only slightly different from 30° for $R \gg r_g$.

This implementation of disk boundary conditions uses some values of the fields in the corona; there is upstream propagation of information. The velocity at $z = 0$ is supersonic but still sub-Alfvénic; upstream propagation of waves is physically expected. A simulation that omits this effect is incomplete, and our results are, manifestly, sensitive to the treatment of the surface conditions. There is, in principle, a risk of numerical instability involved in using this information in the code; fortunately, our runs did not show this kind of instability.

2.2.3 Pitfalls

We mention here some numerical problems that had to be overcome in developing and testing the code, in the spirit of helping developers of similar codes.

A simulation can develop backflow through at least two physical mechanisms. One is simple gravitational infall, which operates mostly in the axial region, where the magneto-centrifugal accel-

eration fails. A second mechanism is cocoon backflow. Due to the differential Keplerian rotation, the inner parts of the flow launch a jet earlier than the outer parts. The cocoon of this jet may produce a temporary backflow. When the backflow impinges on the disk boundary, our boundary conditions shown in §2.2.2 carefully allow the disk to absorb it. This easy prescription avoids the problems discussed below. However, in our earliest simulations, the disk boundary condition was independent of the sign of v_z in the first active zone. This created two kinds of trouble: false acceleration, and filamentation.

2.2.3.1 False acceleration

If there is backflow onto the disk, it encounters a boundary condition imposing a positive speed outwards. Compression increases the density close to $z = 0$. This increased mass is then flung out at the speed v_z given by the boundary condition imposed. No physical process is involved: only a badly chosen boundary condition. This false acceleration is seen more clearly when we reduce the axial injection, allowing the gravitational infall to go all the way into the disk; with these incorrect boundary conditions, the infalling flow quickly bounces back unphysically.

2.2.3.2 Non-physical filamentation

Suppose that, early in the simulation, a portion of the cocoon backflows onto the disk at some radius $R = R_1$, already far from the axis. If the disk boundary condition enforces a forwards speed $v_z > 0$ to the material, we will get an increase in density due to the artificial compression of the coronal material. If the ejection speed v_z is not large, a fast bounce-back will be avoided, and we will not get a false acceleration like in §2.2.3.1. Nevertheless, we still get a localized region, close to the disk, where the density is abnormally large. This larger density will be associated with large localized B_ϕ, and it will have a large inertia; the magneto-centrifugal acceleration will not be enough to lift the material up. The region around R_1 will be a hole in the acceleration front; the jet will proceed forwards for both smaller and larger radii, but it will stagnate here. A succession of such holes would make the simulation look filamentary; again, allowing the disk to absorb the backflow avoids this numerical effect. This numerical defect is more interesting than the previous one, because it is possible to imagine physical (instead of numerical) conditions that may produce a similar effect.

2.3 Initial Conditions

Naturally, we are mostly interested in flows that are independent of the starting conditions. It turns out that in most cases, transients decay in a few Alfvén crossing times, and do not influence the late final flow. Nevertheless, they deserve some detailed explanation, at least for the benefit of researchers wishing to check and continue this work.

The initial density at $z > 0$ is given by $\rho(z, R) = \eta_\rho \rho(z = 0, R)$, with $\eta_\rho < 1$. Initial v_z in the corona is defined similarly through $v_z(z, R) = \eta_v v_z(z = 0, R)$. The initial value for the internal energy is $u = \rho c_{s0}^2/(\gamma - 1)$.

In axisymmetric problems, $\mathbf{B}_p$ at $z = 0$ is always defined from its boundary condition value $B_z(R)$ at $z = 0$. This gives the flux Ψ at the launching surface. The flux in all the volume is defined using either of two alternative prescriptions: fixing the shape of the initial fieldlines, or setting the initial toroidal current j_ϕ to zero. The calculations needed for this second case will be shown in §2.3.1.

In the first case, the initial fieldlines are prescribed by giving the initial position of the footpoint $(z = 0, R = R_0)$ corresponding to the poloidal fieldline passing through a point (z, R). This footpoint R_0 is found from the equation

$$R_0^2 - (R - m_\ell r_\ell (1 + z/r_\ell)^{e_\ell})\, R_0 - R m_\ell r_\ell = 0 \ , \tag{2.20}$$

where B_{z0}, r_b, e_b, r_ℓ, e_ℓ and m_ℓ are constant parameters. The lengthscale r_ℓ determines the location of the initial footpoint R_c of the critical fieldline Ψ_c with $\theta = \theta_c$, e_ℓ gives the initial curvature and collimation of the fieldlines, and m_ℓ sets the maximum slope $\tan\theta$ allowed for the fieldlines, through the prescription $\tan\theta = e_\ell R/(r_\ell + R/m_\ell)$ valid at $z = 0$. If m_ℓ is set to infinity, all angles θ are allowed, and $R_0(z, R) = R/(1 + z/r_\ell)^{e_\ell}$.

In most of these simulations the initial value of B_ϕ has been set to zero, and, consistently, the initial toroidal speed at $z = 0$ is Keplerian, $v_\phi(z = 0, R) = v_K = R\Omega(R)$. For simplicity, this initial v_ϕ is chosen as independent of z. Finally, the radial component of the velocity, v_R, is set to zero in the bulk of the flow, and to its boundary condition value $v_R = B_R(v_z/B_z)$ for $z \leqslant z_{\rm min}$, where $z_{\rm min}$ is the value of z at the first zone above the disk.

In some 2-D finite disk problems, it was found that convergence to a steady state could be accelerated by assuming a lighter coronal density, with a density reduction that follows ellipses with foci at the edges of the disk, $(z = 0, R = \pm R_D)$. For a given point (z, R) in the poloidal plane, with $z > 0$, or $R > R_D$, the sum of the distances to these two foci is calculated:

$$f = \sqrt{(R - R_D)^2 + z^2} + \sqrt{(R + R_D)^2 + z^2} \ . \tag{2.21}$$

This value is then used to find the initial density, following

$$\rho(z, R) = \eta_\rho \rho(z = 0, R) \left[1 + \left(\frac{f - 2R_D}{z_{\rho i}}\right)^2\right]^{-e_{\rho i}/2} \ , \tag{2.22}$$

where $z_{\rho i}$ and $e_{\rho i}$ are appropriate constants. The initial value for the internal energy is again

$u = \rho c_{s0}^2/(\gamma - 1)$. This lower initial density profile makes it easier for the flow to sweep out the initial condition and relax to steady state values; this is particularly useful in simulations using very large boxes, which extend far away from the Alfvén surfaces. However, reducing the density makes also for a worse initial Courant condition, because Alfvén speeds are larger. The value of the exponent $e_{\rho i}$ is chosen based on this trade-off.

The few modifications of the initial conditions, required by non-axisymmetric 3D simulations, will be presented in §5.2.

2.3.1 Current-free poloidal field

In this prescription for the initial poloidal magnetic field, it is necessary to find a current-free field compatible with the choice of $B_z(R)$ at $z = 0$. The advantage of a guaranteed smooth value for the initial currents becomes important in the case of the non-steady solutions, removing suspicions of their non-steadiness being due to numerical artifacts originating in small discontinuities in the current. It will also be interesting to compare the final configuration of fieldlines with the initial potential field. Using the flux function $\psi(z, R)$ as the dependent variable, the differential equation

$$-\left(\frac{cR}{4\pi}\right) j_\phi = \frac{\partial^2 \psi}{\partial z^2} + R\frac{\partial}{\partial R}\left(\frac{1}{R}\frac{\partial \psi}{\partial R}\right) = 0 \tag{2.23}$$

can be solved by separation of variables, subject to the boundary conditions $\psi(z, R = 0) = 0$, $\psi(z = \infty, R) = 0$, and $\psi(z = 0, R) = \bar{\psi}(R)$, with $\bar{\psi}(R)$ a known function of R, that flattens to a constant value ψ_D for $R > R_D$, the outer radius of the disk for finite-disk problems. The solution is

$$\psi(z, R) = R\int_0^\infty dk e^{-kz} J_1(kR) g(k) \tag{2.24}$$

$$g(k) = k\int_0^\infty dR J_1(kR)\bar{\psi}(R) \tag{2.25}$$

$$= k\int_0^{R_D} dR J_1(kR)\bar{\psi}(R) + J_0(kR_D)\psi_D \tag{2.26}$$

where J_n are Bessel functions. Doing these integrations at each grid point can be expensive, especially in regions where these integrals are slow to converge, due to the rapidly oscillatory integrands. For finite-disk problems, a more convenient and safe procedure consists in evaluating with sufficient approximation the integrals at the edges $z = z_{\max}$, $R = R_{\max}$, which together with the known values of $\psi(z, R)$ at the disk and axis, set up the Dirichlet boundary conditions for the elliptic differential equation 2.23. Assuming that the spherical radius at the edges is $r \gg R_D$, the integrals can be expanded in powers of k. The first two terms, which proved enough to calculate our boundary

values in finite disk problems, are

$$\psi(z,R) = \psi_D(1 - z/r) + \frac{3}{2}\alpha z R^2/r^5 \ , \tag{2.27}$$

where $\alpha = \int_0^{R_D} R\bar{\psi}(R)dR - \frac{1}{2}\psi_D R_D^2$. The elliptic equation $j_\phi = 0$ was then solved by a relaxation method of Successive Overrelaxation (SOR, Press et al. 1992), assuming $\psi(z,R) = \bar{\psi}(r)(1 - z/r)$ for the initial guess required by the method.

When doing this relaxation, erroneous results were sometimes observed, ranging from results subtly dependent on computer architecture and other non-physical parameters, to runs collapsing with obviously unphysical results. After some heavy testing, these errors were finally traced to defects in the Absoft compiler used on the Linux machines. A workaround for the error was found, disabling optimization of a particular variable involved in a loop (with a special FORTRAN extension option). A contact to the supplier gave a more general workaround for this serious defect, ultimately due to overeager but erroneous optimization in the strength reduction step, especially visible in loops with variable bounds, as required by the Numerical Recipes implementation of the relaxation method. This workaround requires downloading a variant version of their compilation script, and then turning on one undocumented flag in the compilation line, thus disabling the excessive and erroneous optimization. I thank the customer support of the Absoft Corporation for their prompt answer, which enabled us to continue using their product.

2.4 Code Tests

2.4.1 Parallelization tests

Parallelization of the code was tested by running 3D MHD problems, split over different numbers of computer nodes, checking that both even and odd number of nodes in the different directions would be used (such as $2 \times 3 \times 4$ nodes), and comparing the results with single-node, unsplit output. The comparison was done very stringently, in a bit-per-bit basis, which, when comparing across different architectures, always requires forcing the compiler to produce fully IEEE compliant code, and sometimes requires transforming the endianity of the output.

Passing this stringent test required including a few extra calls to the boundary condition subroutines after some of the field updates. For instance, the boundary conditions are called by ZEUS36 during the trasport term calculation, immediately after each of the updates of ρ and u, where the original ZEUS3D code delayed the boundary condition call for after the completion of the transport step. Probably this measure was not the most efficient, and involves some overkill; however, it was decided to err on the side of safety and correctness versus efficiency. However, probably efficiency is not deeply harmed here, because boundary condition updates are usually less computationally

expensive than full field updates, growing like N^2 instead of N^3, for a typical grid size N.

Having passed these tests, it is now possible to be certain that the code ZEUS36, when used properly and (at least) for the subroutines probed by the test problems, produces exactly the same results when used on either a serial or parallel computer —provided, of course, that the problem is not so large as to overwhelm the capacity of the serial processor.

This stringent testing had to be repeated for the setup, ensuring that proper parallelization has been done, not only for the main numerical engine, but also for the problem setup and problem-dependent boundary conditions.

2.4.2 Boundary condition tests

Once the boundary conditions were implemented and properly parallelized, it was necessary to check if the flow was properly following them. The most stringent test performed consisted in running a simulation up to steady state (such as the simulation presented in §3.2), and then checking if the quantities Ω and l indeed behave as functions of the flux ψ alone, especially at low altitudes z above the boundary. The results are shown in Fig. 3.6. The agreement found for Ω is excellent, but that for l was subject to some visible but minor defects for the first few active zones. It was found that the best choice, reducing z dependence in l, was setting v_R from its boundary condition value $v_R = B_R v_z / B_z$ for $z = z_{is+\frac{1}{2}}$ (with $z_{is} = 0$), despite the fact that this value of $z > 0$ is an active zone for other fields such as v_ϕ, ρ, B_R, and u. Most probably there is still room for improvement here.

Chapter 3

Launching of Cold Winds

3.1 Introduction

The magnetocentrifugal mechanism (Blandford & Payne 1982) is simulated, under the assumption that the winds are already fully supersonic at the launching surface. This was done with the intention of isolating the magnetocentrifugal mechanism from thermal forces, which might cast some doubt about which mechanism was responsible for the jet formation. In the magnetocentrifugal picture, parcels of cold gas are stripped from the surface of a Keplerian disk and flung out along open magnetic field lines by centrifugal force. At large distances from the source region, rotation winds the field lines up into concentric loops around the axis. These magnetic loops pinch on the outflow (or wind) and collimate it into a narrow jet. The mechanism has been investigated for instance in Clarke et al. (1986), Lovelace et al. (1986), Pudritz & Norman (1986), Königl (1989), Ostriker (1997), and recently reviewed by Königl & Pudritz (2000). Here a simulation procedure was adopted, searching for steady-state solutions for a given set of boundary conditions defined at the disk surface. This flexible approach has been adopted by several authors (e.g., Lind et al. 1989; Stone & Norman 1993; Ouyed & Pudritz 1997b; Romanova et al. 1997; Ustyugova et al. 1999). The boundary condition on the disk was treated as described in §2.2.1 and §2.2.2, avoiding overdetermination that may cause the effective boundary conditions governing the wind flow to differ from those imposed at the disk, as mentioned in Meier et al. (1997).

3.2 Reference Run

Here a fiducial or reference simulation is described, to help fix ideas and in the presentation of results. The final, stationary solution is shown in Fig. 3.1. The simulation box has 256×128 active pixels, with $0 \leq z \leq 80.0$ and $0 \leq R \leq 40.0$. Initial and boundary conditions for this run are shown in Fig. 3.2. The boundary density at $z = 0$ is constant and uniform, $\rho = \rho_0 = 1$, with initial $\rho = 0.1\rho_0$ for $z > 0$. The Keplerian velocity scale is given by $v_{K0} = \Omega_0 r_g = 1$, with $r_g = \sqrt{3}$. The function $v_z(z = 0, R)$ is determined by $v_{z0} = 1.7$, $f_{vo} = 0.1$, $r_{vi} = r_{vo} = r_g$, $e_{vi} = 2$, $e_{vo} = 1$, making $e_v = 1.5$. Initially $v_z(z > 0, R) = 10^{-6} v_z(R)$, $B_\phi = 0$ and $v_\phi = R\Omega(R)$, independent of z. The parameters determining $\mathbf{B}_p$ are $B_{z0} = 4v_{K0}\sqrt{4\pi\rho_0}$, $r_b = r_g$, $e_b = 3/2$, $r_\ell = r_g$, $e_\ell = 1$ and $m_\ell = \sqrt{3} = \tan 60°$. The initial sound speed is set to $c_s = 0.0002$, ensuring that pressure is

unimportant in this simulation. The adiabatic index is $\gamma = 5/3$.

The flow is then evolved until a steady state is reached. Once in steady state, the flow is accelerated up to 2.77 times the Keplerian speed at the launching point; the acceleration is purely centrifugal and magnetic. The maximum Alfvén number $v_p/v_{Ap} = 3.98$ is found close to the upper edge, where the maximum fast Alfvén number v_p/v_{At} is also found, equal to 1.36. Collimation of the fieldlines starts even before the flow crosses the Alfvén surface $v_p = v_{Ap}$, as can be seen in Fig. 3.1. The minimum Mach number is 140, showing that pressure is dynamically unimportant in this cold simulation. The acceleration along the fieldline $\Psi = \Psi_e$ passing through the outer edge of the grid is shown in Fig. 3.3. Important fieldlines are Ψ_1, the last fieldline able to make the Alfvén transition inside the computational volume; Ψ_c, the fieldline making a critical angle θ_c with the axis; and Ψ_0, with footpoint at $R = r_{vi}$, at the outer edge of the "core" inner injection, thus separating this core from the wind region.

We have followed this simulation for a time equal to 2.6 Keplerian turns $2\pi/\Omega$ at $R = R_{\max}$ (and, equivalently, 94 turns at the critical radius R_c, 170 at the smoothing length radius r_g). The poloidal velocity and the magnetic field change by less than 1.1×10^{-4} in the last 10% of the run.

The approach to steady state can also be observed in the integrals of motion Ω, l, k and e (Fig. 3.6) which are already functions of Ψ alone, with the exception of border effects for the smallest and largest values of z, important mostly for the non-centrifugal core region, $\Psi < \Psi_0$. We followed these integrals along all the fieldlines in the wind region where $\Psi > \Psi_0$, and found that on each fieldline the integrals depart from their averaged value by less than 5% for Ω, 6% for l, 7% for k and 7% for e. This still overestimates the errors; the corresponding standard deviations divided by the mean are less than 0.3% for Ω, and 3% for the other integrals, further improved to 0.9% if the outermost region $\Psi > \Psi_1$ is excluded.

The Alfvén radius can be found from Mestel's theorem $R_A^2 = l/\Omega$. Our parameter choice is such that angular momentum is primarily extracted from the disk by magnetic stress. Therefore we can estimate l for low values of z by its magnetic term alone, and write an approximate lever-arm ratio as $R_A/R_0 \approx \sqrt{-(B_\phi/B_z)v_{Az}^2/v_z v_K}$. Fig. 3.4 shows the observed value, the exact formula and the estimate; all agree on a value around 3 for all fieldlines, already large enough to justify approximating l by its magnetic term. In the formula of the estimate, the boundary conditions determine all the quantities at $z = 0$, with the exception of the toroidal field B_ϕ, which is allowed to self-adjust in the simulation; assuming a value for the lever-arm ratio gives an estimate for the toroidal field at the base of the wind in steady state, which can then be compared with disk models to check consistency.

The collimation shifts the position of fieldline Ψ_c which makes a critical angle with the disk surface. In steady state θ_c is found at $R_c = 1.85 r_\ell$, while initially it had been $R_c = 1.63 r_\ell$. The integrals $\dot{M}(\Psi)$, $L(\Psi)$ and $G(\Psi)$ are the total fluxes of mass, energy and angular momentum between the axis and a fieldline Ψ. They have very little numerical dependence on the height z of the surface

used to perform the integration, because the ZEUS algorithm respects these conservation laws. The axial thrust T used here is divided by a factor of 2, defined as the surface integral of the kinetic energy term $\rho v_z^2/2$, calculated at $z = z_{\max}$. The integrals $\dot{M}$ and Ψ at $z = 0$ are completely determined from the boundary parameters, and have been done analytically. These results are shown in Table 3.1.

It is important to observe that in this steady state, not only do the fieldlines and streamlines collimate, but also the density, which is roughly a function of R alone for large z, as shown in Fig. 3.5, in spite of the boundary condition at $z = 0$, where ρ is kept constant. This result is in accord with previous asymptotic analysis (Shu et al. 1995).

As a stringent quality check, we made contour plots of the ratio between the magnetopropulsive and magnetocentrifugal forces per unit mass along fieldlines, f_M and f_C, defined in equations 1.32–1.33. Centrifugal acceleration dominates close to the disk, approximately up to the point where v_p achieves the local escape speed; magnetopropulsive acceleration takes over afterwards. There is no visible discontinuity associated with the fieldline $\Psi = \Psi_1$; this shows that the influence of the sub-Alfvénic boundary at $R = R_{\max}$ is not unduly large. However, there is a triangular region near the outer corner where $f_M < 0$, decelerating the flow —the vertices of this triangle are the points $(z = 60, R = 40)$, $(z = 80, R = 30)$ and the outer corner. The box was enlarged in both directions z and R, as shown below in §3.3.1.2, which showed that this is an artifact caused by the edges and not a physical effect.

Table 3.1: Mass discharge $\dot{M}$, luminosity L, torque G, and thrust T at selected fieldlines labeled by their magnetic flux Ψ or footpoint R_0. $\dot{M}$ is in units of $\rho_0 v_{K0} r_b^2$, L in $\rho_0 v_{K0}^3 r_b^2$, G in $\rho_0 v_{K0}^2 r_b^3$, T in $\rho_0 v_{K0}^2 r_b^2$, and Ψ in units of $\sqrt{4\pi\rho_0} v_{K0} r_b^2$. Thrust was calculated at $z = z_{\max}$.

	Ψ_0	Ψ_c	Ψ_e	$2\Psi_c$	$3\Psi_c$	Ψ_1	$R_{\max}$
L	5.5	13.1	18.1	20.5	24.0	25.0	28.5
G	8.8	31	54	71	109	127	265
$\dot{M}$	3.2	6.0	7.7	8.6	10.2	10.8	14.8
Ψ	9.5	22.6	35.8	45.2	67.9	79.2	191
R_0	1.73	3.20	4.77	6.01	9.41	11.35	40
R_A/R_0	2.94	3.14	3.29	3.38	3.50	3.51	–
T	1.9	4.1	5.5	–	–	–	–

3.3 Validation

In this section, the reference run described in §3.2 is criticized, in order to find if it has any dependence on non-physical parameters such as resolution or the size of the computational box, or uncontrolled dependence on the initial conditions.

3.3.1 Dependence of the reference run on resolution and box size

3.3.1.1 Resolution

The resolution of the original reference run is reduced by one half, using a box with 128×64 active pixels, $0 \leq z \leq 80.0$ and $0 \leq R \leq 40.0$. Simulation converges to a steady state similar to the reference run, with maximum $v_p/v_{Ap} = 3.74$ and maximum $v_p/v_{At} = 1.33$. The resolution test is therefore passed.

3.3.1.2 Box size: changes in both length and width together

This simulation is performed in a larger box, with 256×128 active pixels, $0 \leq z \leq 160.0$ and $0 \leq R \leq 80.0$; this is the same space resolution used in §3.3.1.1, with a box extending in space to twice the height and width of the reference run. The lower quadrant of the final, stationary state of this simulation is compatible with the reference run. For instance, in Fig. 3.10, the surfaces of constant Alfvén number for the two runs compare with good results. The strongly accelerated flow found before is reproduced, with a maximum Alfvén number in the lower quadrant of this run of 3.78, and a maximum fast number of 1.34. These results are close to the reference run and even closer to the results of §3.3.1.1, showing a numerically small and qualitatively irrelevant dependence on resolution. It is important to check the ratio f_M/f_C of the forces acting along the fieldlines, especially where this quantity was ill-behaved in the reference run, now the center of the computational box. Fig. 3.11 shows that f_M/f_C in this region is smooth, with positive magnetopropulsive acceleration; therefore the conclusion is that the deceleration observed in the reference run was only an edge effect related to the outer corner. As another indication that outer boundary conditions effects are responsible for this effect in f_M, this simulation shows a tiny triangle of magnetic deceleration near its outer corner.

3.3.1.3 Box size: change in width only; a sub-Alfvénic case.

This run has also the same physical parameters, changing only the shape of the computational box. Here the larger box from §3.3.1.2 has been cut in half, obtaining a square box with 128×128 active pixels, $0 \leq z \leq 80.0$ and $0 \leq R \leq 80.0$.

The results show that the Alfvénic surface crosses the outer boundary $z = z_{\max}$: the flow at the boundary $R = R_{\max}$ is fully sub-Alfvénic. The last fieldline able to make the Alfvén transition, $\Psi = \Psi_1$, now crosses the $z = z_{\max}$ edge. It marks the separation between two very different kinds of simulated flow. Towards the axis, the usual magnetocentrifugally accelerated flow in steady state is present. But outside, in the sub-Alfvénic region, there is a complex structure out of steady state, with filaments of magneto-centrifugal acceleration approximately parallel to the fieldlines, wide islands where the magnetopropulsive force f_M is negative, and sharp variations in the magnetic twist B_ϕ/B_p.

Collimation is excessive, slowing down the acceleration of the flow. The total projected force along fieldlines, $f_g + f_M + f_C$, is negative in a sizable part of the box, instead of only around the axis.

As shown in §3.3.1.2, this complex flow disappears in a larger and axially elongated box; it is created by the finite size, which sets artificial limits on the critical surfaces. The fieldlines in the $\Psi < \Psi_1$ region are able to reach the Alfvén surface, carry the proper critical point information, and propagate it downwards to the disk. Due to the shape of the box here, most fieldlines have $\Psi > \Psi_1$, with critical points at $z > z_{\max}$, inaccessible to the simulation. Mathematically, the assumptions used to decide the number of functions to fix at the disk surface are wrong, because the critical points are not reached. In this region, each streamline is nearly independent, creating the possibility of filaments.

To further check this assumption that the different behavior of our square and non-square boxes is due to the location of the Alfvén surface, the Alfvén surface used in §3.3.1.3 was displaced by reducing the intensity of the magnetic fields by half without changing the box. This allows the flow to become super-Alfvénic inside the square computational box. The flow is now smooth, showing that the relative position of the simulated Alfvén surface and the computational volume determines whether the run will be filamentary or smooth. We have also checked that the conserved quantities are functions of Ψ.

3.3.2 Dependence of results on initial conditions

When large parts of the flow are unable to cross the Alfvén surface, it raises the possibility that the solution is no longer unique, because the boundary conditions do not determine the solution. This may produce dependence on the initial conditions, as observed in the simulation described here.

The setup used is similar to the reference run, differing only in the initial values of B_ϕ and v_ϕ, set by $v_\phi(z = 0, R) = (1 - f_{B\phi})v_K$ and $B_\phi(z = 0.R) = f_{B\phi}v_K B_z/v_z$, with $f_{B\phi}$ a small fraction, equal to 0.01. For simplicity, we have kept the initial values of B_ϕ and v_ϕ independent of z; we could have chosen them to make the initial Ω a function of Ψ, but the initial values for B_ϕ would still be away from steady state.

This simulation starts with a large initial toroidal field, which later in the run provides excessive collimation of the fieldlines, making the angle θ too small for magnetocentrifugal acceleration. Also, the magnetic force along the fieldlines is such that $\mathcal{B} = (RB_\phi)^2$ acts like a pressure (equation 1.33), often producing acceleration; but here $\mathcal{B}$ grows along the fieldlines, decelerating of the flow. Filamentation, low acceleration, and high twist result. This flow is sub-Alfvénic throughout the volume. We observe here that initial conditions can matter in these simulations, provided that the Alfvén surface is not reached.

3.3.3 Results of the validation tests

These tests show that when a majority of the fieldlines reach the critical Alfvén surface inside the computational volume, acceleration of the flow is not affected by artificial effects due to the finite computational box, and it can proceed smoothly, provided that the parameters of the flow allow a physical, stationary solution. If these conditions are met, the simulation results depend mostly on the disk boundary conditions, with little dependence on the outer boundary conditions. The transients are quickly swept up by the advance of the fast accelerating flow. The opposite happens when too many fieldlines lay in the $\Psi > \Psi_1$ region: then the runs show filamentation, excessive collimation, dependence on initial and outer boundary conditions, and —obviously— a slow acceleration. As shown in §3.3.1.3, the shape and size of the simulation box can sometimes induce artificial instability in sub-Alfvénic flows. Caution must be observed also in steady-state sub-Alfvénic flows, due to their possible dependence on the outer boundary (3.3.2). Controlling the position of the critical surfaces inside the computational box can improve convergence, and avoid this kind of numerical uncertainties.

Knowing the importance of keeping this control has helped in the setup of the subsequent simulations. For instance, the critical surfaces are well controlled in the simulations presented in chapters 4 and 5 by setting up initial and boundary conditions such that a finite, rotating disk will be enclosed by the Alfvénic and fast surfaces, which are fully nested inside the computational box. This setup successfully minimizes the influence of the outer boundaries, where the flow speed is now faster than the propagation speed of waves.

3.4 Parametric Study

Now that the reference simulation presented §3.2 is validated, with a known range of reliability, it is possible to vary some of its parameters.

Here we explore the steady state solution dependence on changes in the functions $v_z(R)$, $\rho(R)$ and $B_z(R)$, parametrized by the exponents e_v, e_ρ and e_b, or $e_j = e_v + e_\rho$ and $e_\Psi = e_b - 2$.

3.4.1 Relevance of Mass Flux $j = \rho v_z$

It is important to observe that e_j is indeed a determining parameter of the flow, by comparing simulations starting with different values of the function $\rho(R)$ but the same value of the product $j = \rho v_z$. A simulation was performed with the same value of $j = \rho v_z$ as the standard run, but with $e_\rho = 0.25$ instead of zero, and it was let to run for the same physical time (measured in units of ${\Omega_0}^{-1}$). For $z > 2$, the results of this simulation coincide with the reference run; however, steady state is not achieved at the outer corner (Figs. 3.7 and 3.8). Despite its slower convergence, it represents

the same physical steady state as the reference run, with the exception of very small values of z, where the different profile of $\rho(R)$ at $z = 0$ still has some influence. For a larger value of the density exponent, such as $e_\rho = 1$, the run fails to reach steady state in the same box as the reference run. However, simulations with a box size four times larger, such as in the one used in §3.3.1.2, show that the $e_\rho = 1$ case is nearly identical to the previous case.

Let's suppose that a portion of fluid is just leaving the sonic point with a velocity $\mathbf{v}$, whose component v_z is much smaller than both v_K and v_A, but verifies $v_z > c_{\rm sound}$. The bead-on-a-wire model shows that the accelerating forces of the cold magnetocentrifugal mechanism applied to this portion of fluid do not depend on the velocity. Typically, after a very short distance Δz above the disk, they would add momentum equal to a relevant fraction of mv_K to a portion of fluid of mass $m = \rho\Delta V$. This will be essentially all the momentum of the fluid at an altitude $z = \Delta z$, regardless of the initial value of v_z for all $v_z \ll v_K$. However, mass conservation is still enforced. It is governed by the mass discharge per unit time per unit area, equal to ρv_z. Therefore, the product ρv_z keeps its relevance, even if v_z is irrelevant, provided it is small enough.

This conclusion will be used in the following, by not considering as essentially different two simulations with identical $j(R)$ profiles, differing only in having two different values of $v_z(R)$, provided that both of these values are supersonic, and far below Keplerian and Alfvén speeds. This has been checked again in the non-steady simulations presented in §4.3.

3.4.2 A parameter sweep

Here a few simulations for different values of the parameters are presented. Fig. 3.9 shows the critical surfaces and fieldlines for these runs. Their shapes are qualitatively similar, with the remarkable exception of the outer fieldlines for the flatter j simulation $e_j = 0.5$, $e_b = 1.5$; some of these lines start pointing inwards instead of outwards. Not all fieldlines are able to propel the flow centrifugally at $z = 0$; they must spend some initial kinetic energy before acceleration can start. Further tests can tell if this unexpected effect is physical or only a numerical artifact. Because the assumption $|\theta| > \theta_c$ is not fulfilled everywhere, these tests should take into account that the mass flux should be reduced for those fieldlines, requiring the usage of a mass flux j dependent on θ.

Values of speed, Alfvén number, lever-arm ratio, luminosity and torque are calculated at the point $(z_{\rm max}, R_{\rm max})$ and given as functions of the exponents e_b, e_v and e_ρ in Table 3.2. The first four columns are the simulations represented in Fig. 3.9. The last column is the simulation shown in Fig. 3.7, where we can already see that it is almost completely equivalent to the reference run. Only its flux at the outer corner is slightly different; this is due to its insufficient convergence to the steady state in that region of the computational volume.

Table 3.2: Dependence of some flow quantities on the exponents e_b, e_v and e_ρ. Fluxes and thrust are calculated at the outer corner of the grid, and made dimensionless as in Table 3.1. The maxima of v_p/v_{K0} are taken at $z = z_{\max}$.

e_v	1.5	0.5	1.25	0.5	1.25
e_b	1.5	1.5	1.625	1.25	1.5
e_ρ	0.0	0.0	0.25	0.0	0.25
e_j	1.5	0.5	1.5	0.5	1.5
e_Ψ	-0.5	-0.5	-0.375	-0.75	-0.5
Ψ	35.8	42.5	27.1	70.8	38.8
R_0	4.77	5.64	3.91	7.68	5.15
R_A/R_0	3.29	2.31	3.03	2.61	3.31
Max. M_A	3.98	5.06	5.26	2.66	3.78
Max. v_p/v_{K0}	1.67	1.33	1.67	1.31	1.54
$\dot{M}$	7.73	15.02	6.89	19.54	8.05
L	18.1	23.5	14.5	34.3	18.8
G	54	85	38	162	58
T	5.5	8.9	4.8	10.4	5.2

3.5 Conclusions

As expected, cold, steady jets can be launched smoothly from Keplerian disks by the magneto-centrifugal mechanism. The same mechanism is also effective in collimating the outflows. Collimation is observed both in the shape of the fieldlines and in the density profiles, which become cylindrical and thus jet-like at large distances along the rotation axis, in agreement with asymptotic analysis.

Steady-state jets obtained in earlier studies using an essentially incomplete treatment of the disk boundary conditions are qualitatively unchanged when this deficiency is rectified. It remains to be shown, however, whether the same is true in general for non-steady jets.

The magneto-centrifugal mechanism for jet production is robust to changes in the conditions at the base of the jets, which have consequences consistent with expectations. However, the size of the simulation box can strongly influence the outcome of a simulation unless most field lines pass through the Alfvén surface within the box. As a result, simulations that produce mainly sub-Alfvénic disk outflows, steady or not, must be treated with caution. This highlights the pressing need for box-invariant simulations, which will be shown in the following chapters.

The structure of the magnetocentrifugal outflows is insensitive to the separate values of the initial density or flow speed at the injection surface, as long as their product (i.e., the mass flux) is kept constant. This important result, which simplifies the parametrization of the flows, will be used in the following two chapters.

The code ZEUS3D can be parallelized so that solutions from different subgrids match smoothly.

Fig. 3.1 *Reference simulation.*

The local Alfvén number v_p/v_{Ap} is shown in grayscale. In thin black, fieldlines and vectors of $\mathbf{v}_p$. In medium black, the critical surfaces $v_p = v_{Ap}$, $v_p = v_{At}$ and the local escape speed line $v_p = \sqrt{-2\Phi_g} \equiv v_{esc}$; the line $B_p = B_\phi$ is shown in dashes. In thick black, some selected fieldlines: Ψ_1 passing through the intersection between the Alfvén surface and the outer boundary; Ψ_0 at the outer edge of the axial injection zone, separating the injected core from the main wind; Ψ_c, the fieldline whose inclination is critical at $z = 0$; and Ψ_e, passing through the outer edge of the grid.

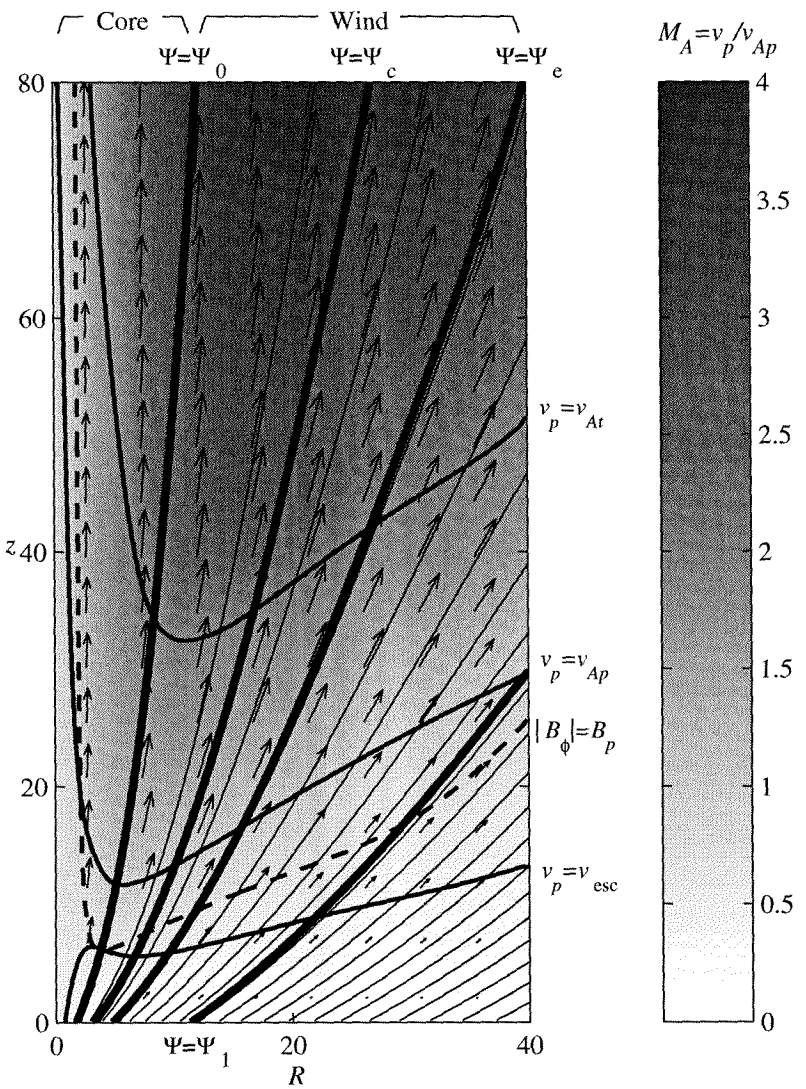

Fig. 3.2 *Reference simulation.*

Boundary and initial conditions for v_z, $v_{Az} = B_z/\sqrt{4\pi\rho}$, v_{Ap}, $v_K \equiv R\Omega$, B_z *and* $\sqrt{-\Phi_g} = v_{esc}/\sqrt{2}$ *at* $z = 0$ *as functions of* R, *normalized by the Keplerian speed scale* $v_{K0} = \Omega_0 r_g$.

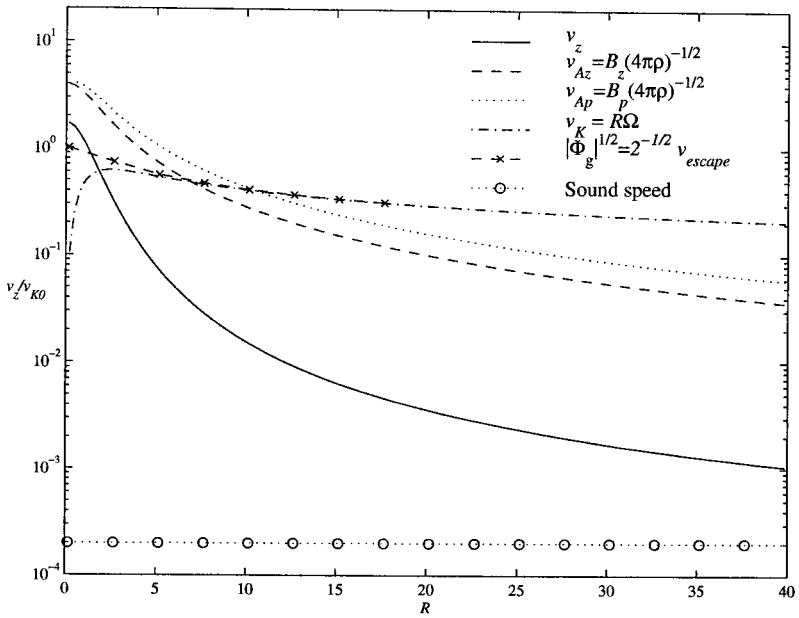

Fig. 3.3 *Reference simulation.*

Velocities along the fieldline $\Psi = \Psi_e$ *passing through the outer edge of the grid. Plot of* v_p, v_{Ap}, v_{At}, v_{esc}, $R\Omega$, $R_0\Omega$ *and* v_ϕ *vs.* z, *showing the growth of poloidal speed.*

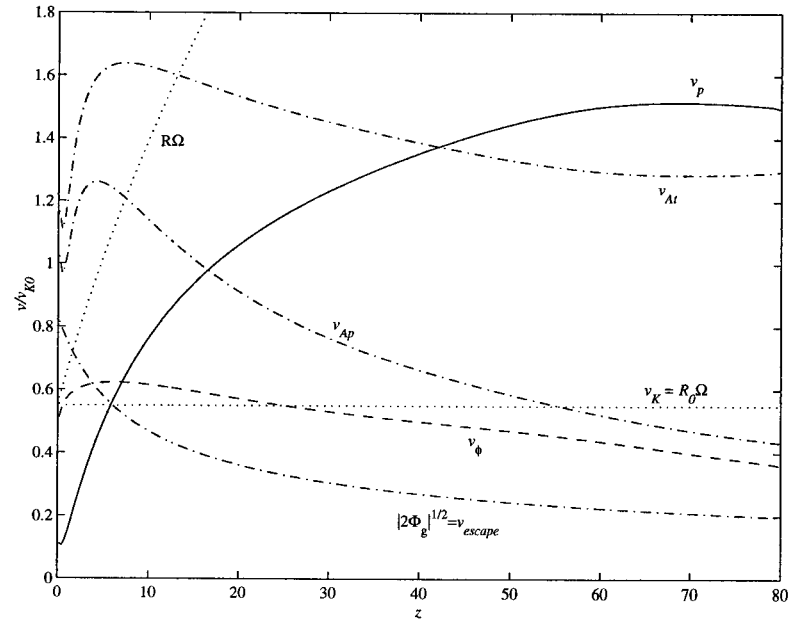

Fig. 3.4 *Lever arm ratio R_A/R_0 (full lines), compared to $\sqrt{\ell/\Omega}$ in dashes and $\sqrt{-(B_\phi/B_z)v_{Az}^2/v_z v_K}$ in dots. Both the flux Ψ and the footpoint R_0 are used to label the fieldlines.*

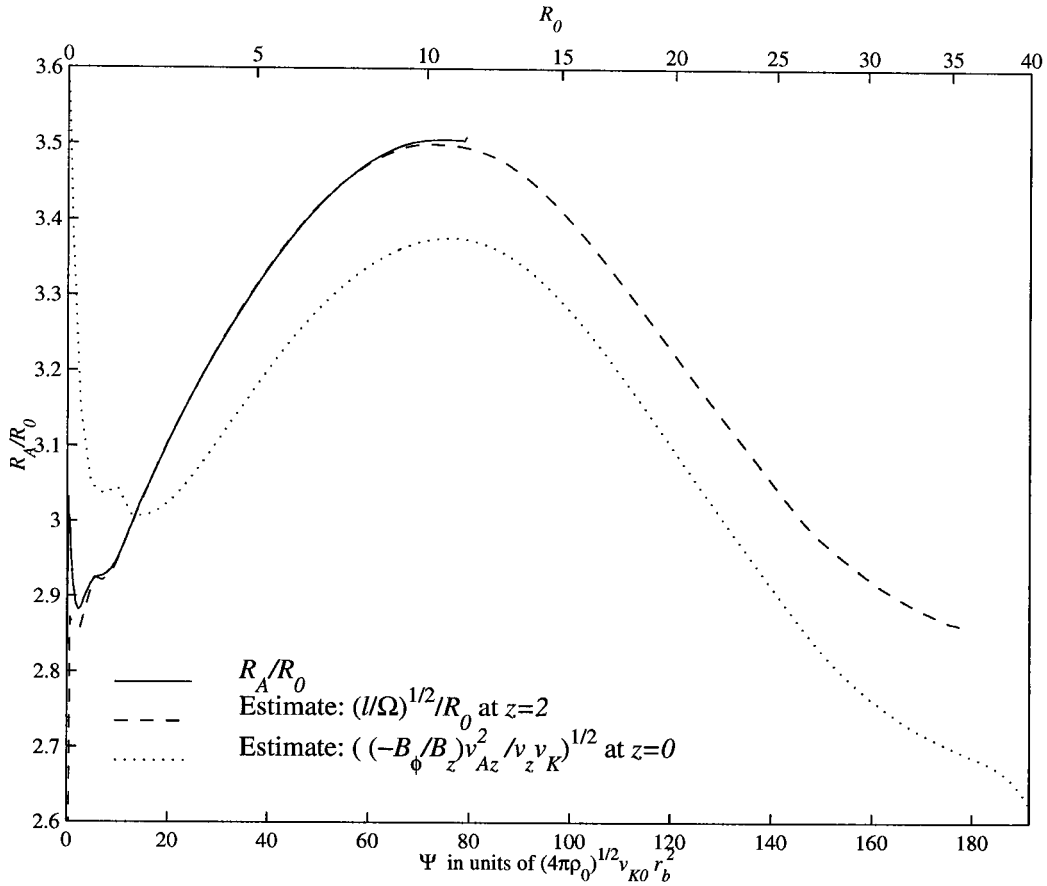

Fig. 3.5 *Greyscale of the density in the reference run, showing collimation.*

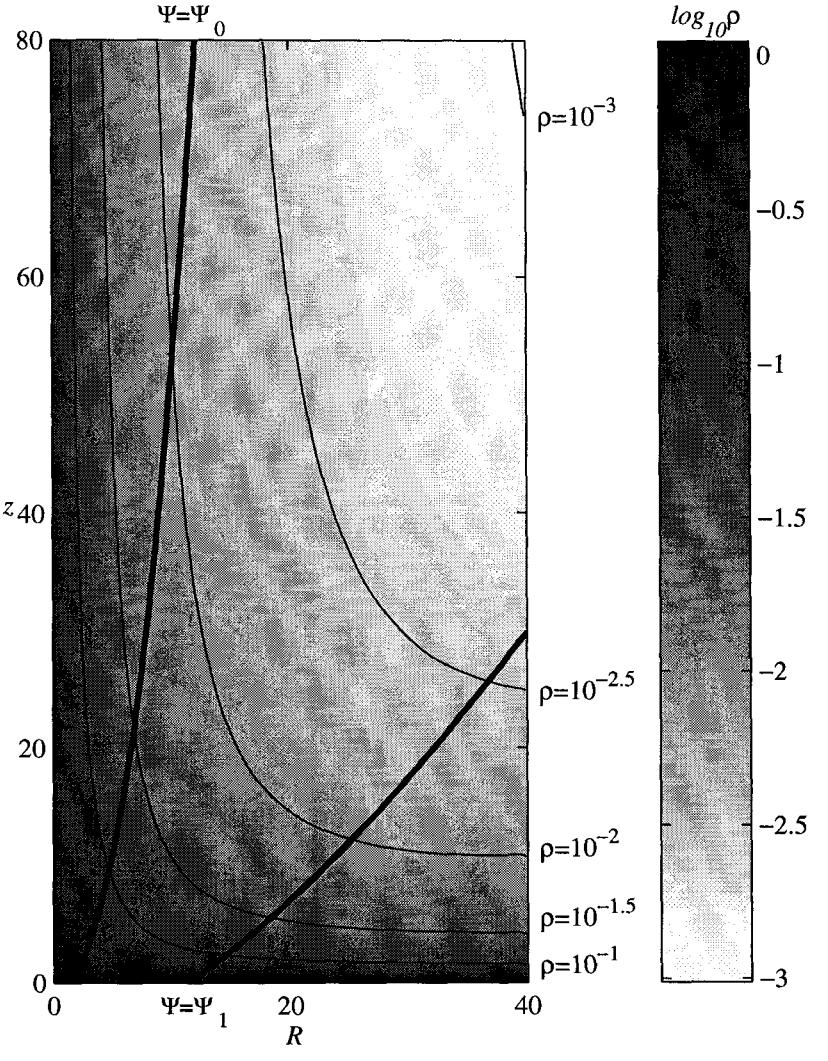

Fig. 3.6 *The four cold conserved quantities, shown as contour levels in a Ψ vs. z plot. Two field-lines and critical surfaces are shown in dots, together with the outer edge of the box $R = R_{\max}$ and the box midline $R = R_{\max}/2$. The region where $\Psi > \Psi_1$ is not fully reliable.*

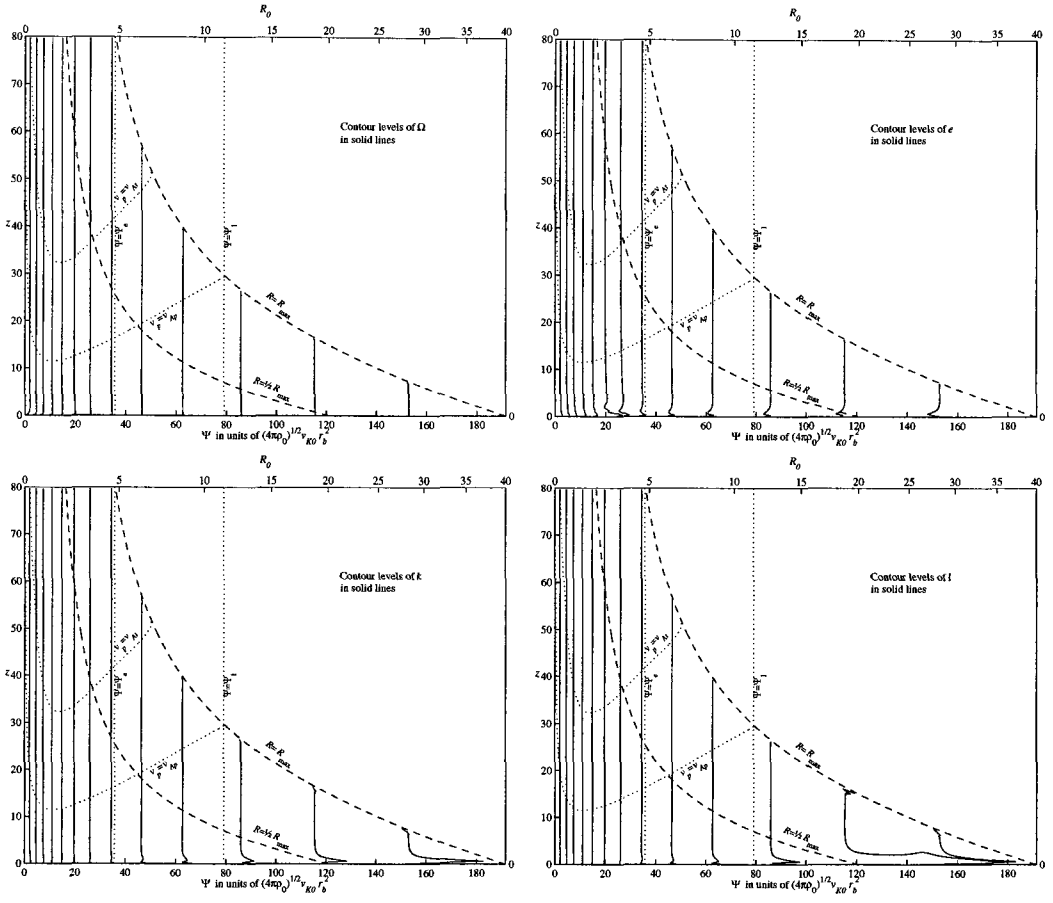

Fig. 3.7 *A variable density simulation defined by* $e_\rho = 0.25$, $e_j = 1.5$, *and* $e_\Psi = -0.5$, *is compared to the reference run, which has the same mass flux* $j = \rho v_z$, *and a flat density profile at* $z = 0$, *defined by* $e_\rho = 0.0$, $e_j = 1.5$, *and* $e_\Psi = -0.5$. *Fieldlines and contours of* M_A *in these two runs are shown.*

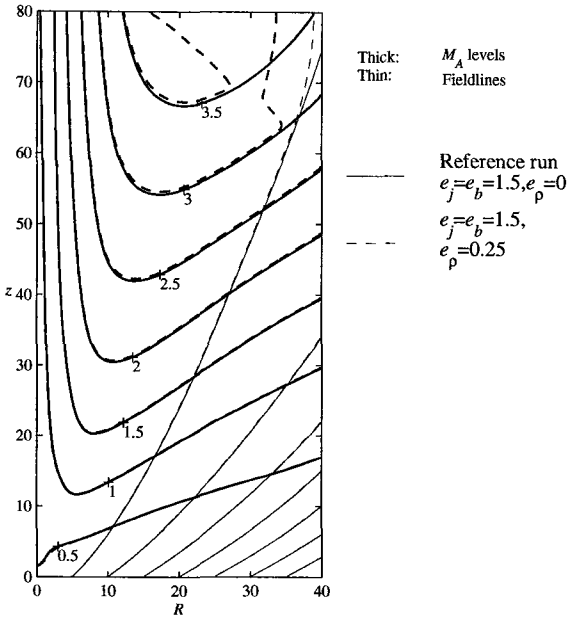

Fig. 3.8 *The variable density simulation defined in Fig. 3.7 is again compared to the reference run, this time by showing contours of the density of one run divided by that of the other.*

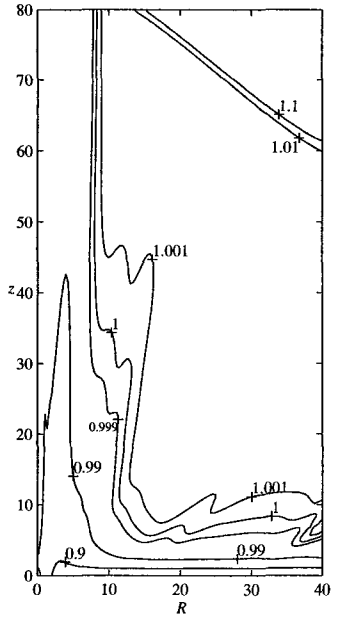

Fig. 3.9 *Comparison of four runs. Alfvén surface in thick lines, fast surface in medium and field-lines in thin. Fieldlines have been chosen to pass through the same footpoints in the four runs.*

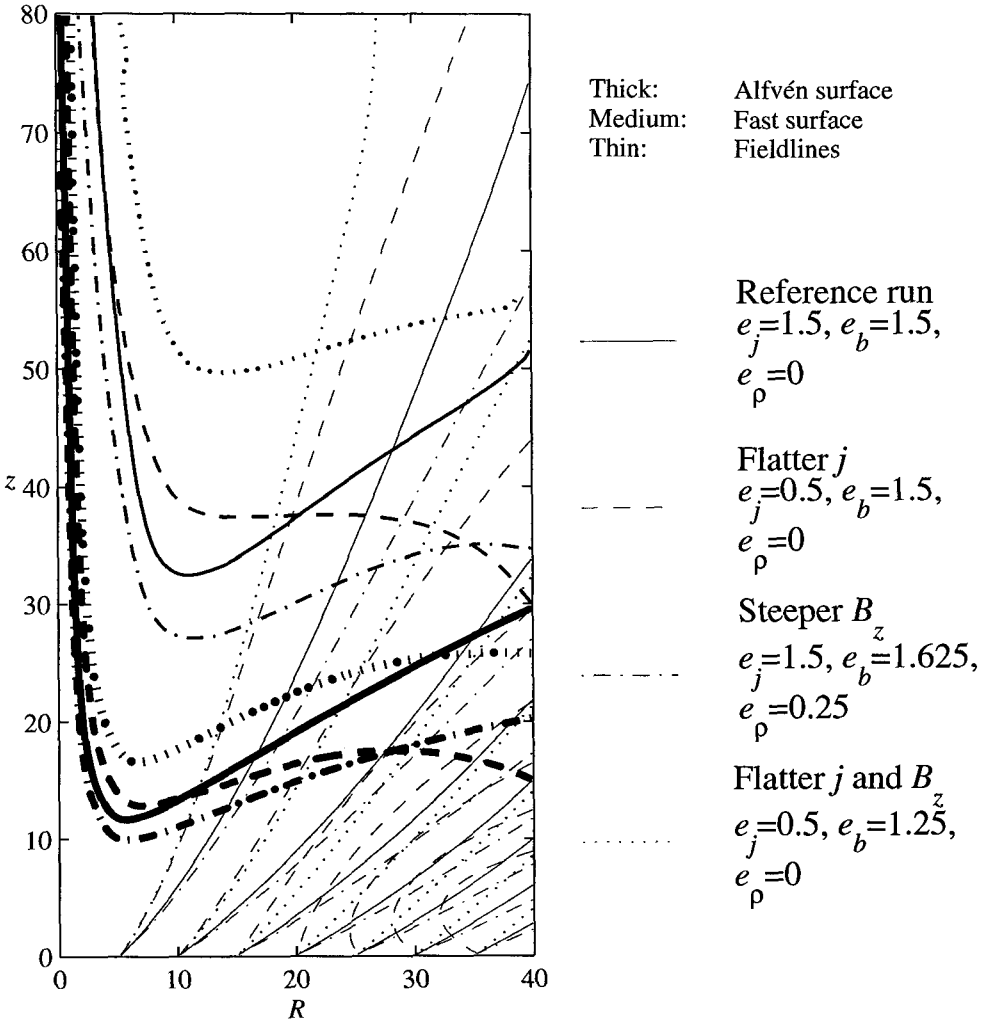

Fig. 3.10 *Contour plots of $M_A = v_p/v_{Ap}$, for the reference run (solid lines) and a larger and wider box (dashes), compared to check convergence.*

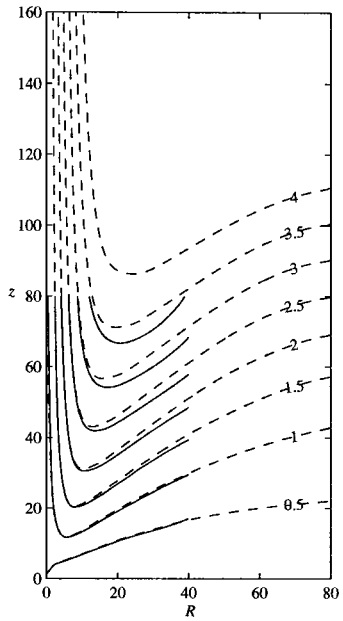

Fig. 3.11 *Simulation on the larger and wider box.*
In solid, the contour levels $f_M/f_C = 0$, 1, 2, 3, and 4, show the ratio of magnetic over centrifugal forces along the fieldlines (shown in dots). The $f_M = 0$ level is a short, thick line at the outer corner.

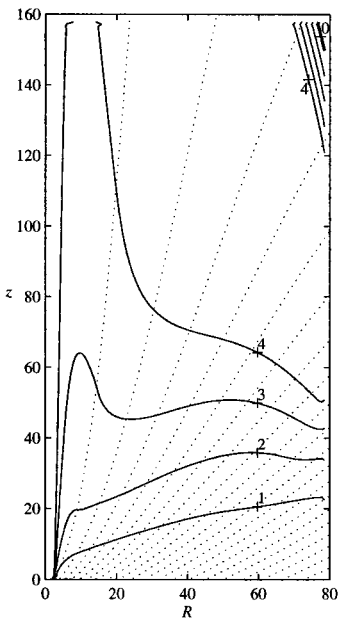

Chapter 4

MHD Outflows from Finite Disks

4.1 Introduction

In the previous chapter we described the use of the ZEUS MHD code to study the problem of wind launching from a Keplerian disk. The disk was idealized as a boundary condition at $z = 0$, on which open magnetic fields are firmly anchored *at all radii*. Mass was injected onto the open field lines at a prescribed rate and then accelerated magnetocentrifugally to produce a high speed wind. In this chapter, we shall tie the open field lines to a finite disk.

There are good astrophysical as well as numerical reasons to consider winds driven from finite regions of accretion disks. There are two popular models for the origin of the spectacular optical jets observed around many young stellar objects (YSOs), both based on the magneto-centrifugal mechanism. The models differ on where the wind-driving open magnetic fields are anchored. If the open field lines are anchored in a narrow region on the disk near the corotation radius of the stellar magnetosphere, then the wind is called an "X-wind" (Shu et al. 2000). The X-wind serves the fundamental purpose of removing angular momentum from the central star and keeping it rotating slowly as observed, below the breakup rotation speed. If, on the other hand, the field lines are anchored over a wider region of the disk, then a "disk-wind" is produced (e.g. Königl & Pudritz 2000). The disk-wind may be primarily responsible for driving the mass accretion through the portion of disk where the wind is launched. The wind-launching region is bound from the outside by a low temperature region (with $T < 10^3$K) where magnetic field is effectively decoupled from the disk material (e.g., Nakano & Umebayashi 1986). For typical parameters of YSO, the radius of the disk region that is well-coupled magnetically is $\sim$1 AU (e.g.,Li 1996). Therefore, the size of the wind-launching region is finite in both models, and it is of considerable interest to examine the effects of the size of the launching region on the properties of the outflows, especially on large scales that can be probed observationally. Small magnetized disks occur in another type of astrophysical systems, the cataclysmic variables (CVs).

Numerically, a finite launching region is highly advantageous because simulations are performed inside a finite computational box. Ideally, the size of the simulation box should not interfere with the wind structure being simulated inside the box. This non-interference is difficult to achieve if mass is injected at all radii from the plane of the disk surface into the wind. In such a case, there will always be a region close to the outer edge of the disk that does not have enough room

inside the computational box to accelerate beyond the fast magnetosonic speed, no matter how big the simulation box is. In other words, there will always be a sub-fast region at the edge of the simulation box, which allows information at the outer boundaries to propagate upstream to the launching surface, creating an undesirable coupling between the wind and the computational box. In some cases, such as in §3.3.1.3 this coupling destroys the wind completely. If, on the other hand, the wind launching region is finite, the last open fieldline will be anchored at a finite radius from the center and lie on the equatorial plane to fill space in the absence of a confining medium.[1] Mass loaded on this last, equatorial fieldline will be accelerated above the fast magnetosonic point at a finite radius and the problem associated with the infinite disk disappears. It is now possible to have a wind that is entirely super-fast before leaving the simulation box. In such a case, the box size should have a minimal effect on the wind.

The removal of box-dependence allows us to simulate simultaneously the launching, acceleration, and collimation of magnetocentrifugal winds from small to large (observable) scales. Traditionally, the large scale wind structure is studied by asymptotic analyses (e.g. Heyvaerts & Norman 1989; Shu et al. 1995). There exists a "gap" between the large scale structure obtained by asymptotic analyses on one hand, and the small structure in the wind acceleration region obtained numerically on the other. The calculations presented here are able to close this "gap" in MHD wind theory and predict the observable quantities of jets/winds on large scales from the conditions on the launching surface. Large scale quantities that are of particular interest include the isodensity contours which control the appearance of optical jets, and the mass and momentum distributions which govern the interaction of the wind with its ambient medium. In the case of YSOs, the interaction creates a bipolar molecular outflow, whose properties are well constrained by observations (Lada 1985). Results of these simulations can be compared to both direct observations and the asymptotic theory.

Smooth, steady, accelerated flows are often found, compatible with most theoretical expectations. These will be presented in §4.2. However, some simulations (presented in §4.3) produced non-steady jets, whose intensity increases and decreases in episodic outbursts, resembling in their intermittency those found by Ouyed & Pudritz (1997a). These non-steady jets are characterized by an intermittent opening and closing of the launching channel, defined by the set of fieldlines whose inclination to the axis is larger than the critical angle of 30° (Blandford & Payne 1982). Many jet flows are well-described as being episodic, which gives more importance to this intermittent model. An exploration of the causes of this intermittency was done, showing that its main cause is the failure of the lower portions of the wind to keep up to quasi-Keplerian speed.

[1] A confining medium would be more realistic. It would require a simulation or at least a description of the interstellar medium; this need is avoided here by setting the last fieldline as equatorial, with expected little change in the magnetocentrifugal results.

4.2 Steady Outflows

The boundary and initial conditions of these simulations have been explained in §2.2.2 and §2.3, where the parameters used are explained.

Because one of the purposes of these finite disk simulations to compare with asymptotic solutions, large computational boxes were used. Assuming that the inner radii are all equal, $r_g = r_b = r_\rho = r_{vi} = r_{vo} = z_{\rho i} = 1$, the outer radii R_D and R_{D1} were taken between 10 and 30, and the box sizes $R_{\max}$ and $z_{\max}$ between 200 and 1000.

In a few of the finite disk simulations, the bulk poloidal field was started using a prescription for the fieldlines as in equation 2.20, with $m_\ell = -R_D/r_\ell < 0$ to ensure that the last fieldline is equatorial.[2] The exponent e_ℓ was set to 1, and the lengthscale to $r_\ell = r_b$. However, after it was observed that some of these finite-disk simulations showed a pronounced instability (§4.3), it was decided to use an initial current-free poloidal field, as described in §2.3.1, with the intention of removing any doubt of the instability being due to an effect of the current j_ϕ otherwise present in the initial condition. This change had no effect in the development of the instability (for the unsteady cases) or on the final steady state achieved (for the steady ones), but it was kept because it provides a good initial condition with the advantage of reducing the number of free parameters.

Another modification introduced in some of the simulations was changing the boundary condition function $\rho(z = 0, R)$, reducing the density close to the origin, so that either the mass flux $j = \rho v_z$ or the kinetic energy term ρv_z^2 would be flat for $R < r_{vi}$, despite the presence of the axial injection. This was done with the intention of representing a low density but large velocity flow at the axis, such as a particle-antiparticle jet. The expected advantage of this is that the axial region would contribute less to the density profile at large z, allowing a more isolated study of magnetocentrifugal effects.[3]

4.2.1 Results

4.2.1.1 Reference run

We first performed a baseline simulation —the reference run— adopting the following conditions. All the inner radii used in definitions of boundary and initial profiles have been set to 1. The outer radii, used in equation 2.16, are $R_D = 10$ and $R_{D1} = 8$, making a rather small launching disk (only one decade in extent). The Keplerian velocity scale is given by $v_{K0} \equiv \Omega_0 r_g = 1.0$. The velocity

[2] In solving the quadratic, the minus sign must be chosen. The opposite choice applies to the infinite disk of the previous chapter, which has $m_\ell > 0$.

[3] It should be mentioned that this axial density reduction has one numerical disadvantage. The reduced density at the axis pushes the fast magnetosonic surface up, so much that frequently this surface is unable to close inside the computational volume. This leads to a diminished control in the axial region, especially for large z. This was considered tolerable, because the upper axial region of the simulation may comprise a core relativistic jet derived from the vicinity of a black hole (in an AGN simulation) or high entropy ionized gass in the case of a YSO, and it is not in any case well represented by the centrifugal model.

profile was set as in equations 2.12-2.14, with the exponents $e_{vi} = 2$ and $e_{vo} = 0$ (implying $e_v = 0.5$), the scale $v_{z0} = 1.7$ for the axial injection, the scale factor $f_{vo} = 0.1$ for the outer profile, and a value of 2 for ν. The magnetic field intensity is defined as in equation 2.11 with $B_{z0} = 4\sqrt{4\pi}$, and $e_b = 1.5$. The density is given by $\rho_0 = 1$, $e_\rho = 0$. However, it is not completely flat, because close to the axis the density was reduced, so that for $z < 0$ and $R < r_{vi}$, the momentum flux component ρv_z^2 is set to a constant value, taken from the value calculated at $R = r_{vi}$.

The initial poloidal field has been chosen as current-free (in equation 2.27, $\alpha = -191.8244$). The initial density field is given by 2.22, with parameters $\eta_\rho = 0.1$, $z_{\rho i} = 1$ and $e_{\rho i} = 1.5$. This flow is very cold, with a sound speed parameter of $c_{s0} = 0.0002$.

The computational box extends up to $(z_{\max}, R_{\max}) = (1000, 1000)$, with 190×210 non-uniform active zones. The z-grid is uniform from $z = 0$ to $z = 8$, with 40 active zones, changing continuously to a ratioed[4] grid with 150 zones going from $z = 8$ to $z = 1000$, with a ratio of 1.0350 between adjacent values of Δz_i; the R-grid is uniform from $z = 0$ to $z = 12$ (thus covering the disk), with 60 active zones, followed by 150 non-uniform zones from $R = 12$ to $R = 1000$, using approximately the same ratio of 1.0350 between zones.

Fig. 4.1 shows the fieldlines and critical surfaces, and Fig. 4.2 shows profiles of velocity and density. The third panel of both figures uses a logarithmic scale in both axes to show both the approach to the asymptotic regime at large altitude and to the launching region at small altitude.

Speeds at various large altitudes can be seen in Fig. 4.3, showing the acceleration of the flow. Profiles of density, multiplied respectively by R^2 and r^2, hint about the asymptotic values (Fig. 4.5). The lever arm ratio $\sqrt{l/\Omega}/R$ has been calculated over the finite disk, and shown in Fig. 4.4.

4.2.1.2 Influence of the axial injection

Two runs were performed having a boundary condition at $z = 0$ with either $j = \rho v_z$ or ρ constant inside $R = r_{vi}$, instead of ρv_z^2 as in §4.2.1.1. The results are shown in Figs. 4.6 and 4.7. Comparing them to the reference run, the different treatment near the axis has influence only inside the fieldline with footpoint at $R = r_{vi}$, but not outside. Inside this narrow region, the main effect of the change is seen in the critical surfaces (Alfvén and fast), which are closer to the disk for the heavier axial jets. The importance of this test is that the exact treatment of the axial injection is relevant only in a limited part of space, which is convenient given the fact that this axial injection is not controlled by the magnetocentrifugal mechanism.

4.2.1.3 Parameter dependence

Four simulations having the same value of $e_b = 1.5$ are shown in Figs. 4.8 and 4.9, panels (abcd). The value of the exponent e_j increases along these panels, which reduces the mass loading in the outer

[4]Each zone is wider than the previous one by a small constant factor.

regions of the disk. The increase of e_j pushes the Alfvén and fast surfaces in the equatorial region outwards, so much that the fast surfaces do not close back to the equator inside the computational volume for the cases presented in panels (c) and (d).

Three simulations, shown in panels (bef) of the same figures Figs. 4.8 and 4.9, have the same value of $e_j = 1.5$. The Alfvén surface moves inwards for increasing e_b; however, the fast surface did not vary regularly. The profiles of constant density are quite similar in these three runs; they seem to be controlled by the profile of j rather than by that of B_z. Figs. 4.8 (a) and (e) have similar hydromagnetic lines. This hints that the position of the critical surfaces might be determined by the adimensional ratio $4\pi\rho v_z v_K/B_z^2$, which is the approximately the same in both panels. However, the corresponding hydrodynamic quantities, as shown in Figs. 4.9 (a) and (e), are not especially similar to each other. It seems that the position of the isodensity contours depends on the mass loading exponent e_j, more than in the magnetic field exponent e_b.

4.3 Intermittent Outflows

4.3.1 Description

When the mass loading ρv_z is increased too much for a certain profile of B_z, the magnetocentrifugal mechanism cannot launch the flow continuously any longer.

The simulations show how the standard magnetocentrifugal mechanism at first starts to operate, launching material in the expected way, accelerating the fluid and forming the expected Alfvén and fast surfaces. However, the stability of the flow is already compromised at its source. The rotational speed v_ϕ, necessary to launch the plasma against gravity, starts to drop below Keplerian at some points just above the disk, at the same time that $|B_\phi|$ grows larger, keeping corotation enforced at the disk surface. When v_ϕ reaches a sufficiently low value (typically $\sim 0.7 v_K$ in the simulations), matter is pulled inwards gravitationally, making a flow parallel to the disk. The fieldlines, which are frozen to the flow, also bend inwards. In particular, their angle to the axis becomes smaller than 30°. This might be a secondary consideration, however: this angle is special only assuming that the rotational speed is close to Keplerian, which had already been violated. The mass density close to the disk increases due to the larger mass loading and the deficient acceleration. The toroidal magnetic field also becomes larger, with the term $-B_\phi v_p/B_p$ becoming of the same order of magnitude as the Keplerian speed. Some time later, the overstretched fieldlines will bounce back to something closer to their original position, allowing again a temporary magnetocentrifugal acceleration of the outflow. Therefore, launching and acceleration do not fully stop, but become intermittent and chaotic, with some regions on the disk contributing to the flow at different times, blobs of matter achieving acceleration at various heights, and, occasionally, moments of smooth outflow when the fieldlines are rebounding to something closer to the configurations shown in §4.2.

4.3.2 Results

A series of simulations was performed with $R_D = 30$, $R_{D1} = 24$, varying exponents e_b, e_ρ and e_v, and otherwise the same physical parameters as the reference run.[5]

The most important result is that for each value of e_b, there was found a value of $e_j = e_\rho + e_v$ low enough that it will make the system unsteady, as shown on Table 4.1, indicating that an increase in the mass loading profile for a given magnetic flux can trigger the unsteady mechanism. The critical parameter seems to be in the neighborhood of $B_z/\rho v_z$ rather than $B_z^2/\rho v_z$, with an exponent $e_b - e_j \approx 0.5$, below which the system becomes unsteady, for the present choice of the other parameters. The instability is slow to appear, typically taking a time of around 100π to affect the inclination of the fieldlines, and ten times as much between the occasional smooth outflows. In the process of formation of the instability, the value of v_ϕ close the disk surface drops below v_K (Fig. 4.10).

Table 4.1: Stability of the simulation for various values of e_b and e_j, for a disk radius $R_D = 30$, $R_{D1} = 24$. Values of v_ϕ taken near the disk surface.

e_b	e_j	e_ρ	$e_b - e_j$	$2e_b - e_j$	Result
1.5	0.5	0.0	1.0	2.5	Unsteady
1.5	1.5	0.0	0.0	1.5	Steady
1.5	1.5	1.0	0.0	1.5	Steady
2.0	1.5	1.0	0.5	2.5	$v_\phi \approx 0.5 v_K$: expected to become unsteady.[a]
2.0	2.0	1.0	0.0	2.0	Steady as of $t = 63\pi$. $v_\phi \approx v_K$: expected to keep steady.
2.0	2.5	1.0	-0.5	1.5	Steady
2.5	2.5	1.5	0.0	2.5	Steady[b] despite $v_\phi \approx 0.7 v_K$.
2.5	2.0	1.0	0.5	2.5	Unsteady.

[a] Instability not yet developed at the end of this run, $t = 62\pi$.
[b] At time $t = 300\pi$.

A series of simulation was performed with $e_b = 1.5$, $e_j = 0.5$, and $e_\rho = 0$, varying the radii of the finite disk R_D and R_{D1}. With $R_D = 30$ and R_{D1} varying between 10 and 24, all the results were unsteady, and the same with $R_D = 25$, $R_{D1} = 20$. A steady simulation was found for $R_D = 20$, $R_{D1} = 16$. Comparing with §4.2.1.1, the values $R_D = 10$, $R_{D1} = 8$ are also steady. This hints that the points where B_z has become too small for the given ρv_z in the unsteady runs are located at $R \gtrsim 20$, which may be a guide in the construction of a more precise criterion for the maximum steady mass loading allowed.

One of the simulations used a prescription for the mass loading boundary condition with a sharp angular dependence, such that if $R > 1.5 r_{vi}$ and the inclination $\theta(R)$ of the fieldline at $(z = 0, R)$ was smaller than 30°, v_z was set to 0.01, times the appropriate spline arc defined in equation 2.16. Otherwise the simulation used the same parameters as in line 1 of the table 4.1. The result was a steady flow. The angular dependence introduced a negative feedback to the unsteady mechanism

[5] The grid used had $z_{\max} = R_{\max} = 200$, with 140×160 active zones, uniform with a spacing $\Delta z_i = \Delta R_j = 0.2$ for $z \leqslant 8.0$ and $R \leqslant 32.0$, ratioed with constant ratios $\Delta z_{i+1}/\Delta z_i = 1.0365$ and $\Delta R_{j+1}/\Delta R_j = 1.0346$ for the remaining 100 zones.

which kept the ratio $k = 4\pi\rho v_z/B_z$ constant (in an average sense) along the disk instead of allowing it to grow with distance as $\propto R$, as the raw exponents would indicate (Fig. 4.11). The mean profile of ρv_z produced by this kind of angular-dependent simulation is probably very close to the maximum loading allowed for steady launching with the given profile of B_z.

4.3.3 Comparison with previous results

An intermittent behavior, whose presence depends on the value of the mass loading, may at first resemble the recent results by Ouyed & Pudritz (1999) (OP99). However, the relation with mass loading is in the opposite direction: their unsteady flows appear for low mass fluxes instead of large. That in itself is not implausible: there might be a range of speeds required for smooth launching, this thesis exploring the upper bound, OP99 the lower.

The results presented in OP99 can be criticized on the basis of their boundary conditions at $z = 0$, which constrain the magnetic field components B_ϕ and B_R too stringently and overdetermine the flow. It would be desirable to repeat these calculations using less restrictive boundary conditions for the magnetic fields, such as those presented here or those presented in Ustyugova et al. (1999). In addition OP99 only present short simulations, and may be describing transients reflecting the initial conditons: they have run their problems by times in the order of $t = 150$, smaller than the times presented here, in fact smaller than the typical time $t = 100\pi$ necessary for the formation of the unsteady mechanism described in this chapter. It would be interesting to observe how these simulations would behave if left to run up to $t = 3000\pi$. Finally, their usage at $z = 0$ of very low values of $v_z \sim 10^{-5} v_K$, implies that the value of the speed in the first active zone of the grid will be much larger than the value at $z = 0$. [6] It could be feared that this impulsive acceleration may weaken the link between the parameters defined at the BC and the simulated flow, because the effective boundary condition for v_z seen by the bulk of the fluid is indeed much larger than the value used to parametrize the runs, and completely different from it. Fortunately, this is not the case, because the ZEUS code used in OP99 guarantees mass conservation up to machine round-off error. While the velocity seen by the bulk of the flow is not authentically as small as the parameter value of around $\sim 10^{-5} v_K$, it can be assured that the mass loading ρv_z has been parametrized reliably. The mass discharge ρv_z controls the launching of cold flows, rather than v_z or ρ separately (§3.4 in this thesis; Krasnopolsky, Li, & Blandford 1999), being of little physical importance which of the two factors in the product is the control parameter. Numerical considerations lead to a preference for reducing v_z rather than reducing ρ, because the latter reduction increases the Alfvén speed, making the Courant condition more stringent. Therefore, OP99 is using a reliable parameter to reduce the

[6] The authors explicitly admit this effect, when they note that while their v_z at the disk is subsonic, supersonic speeds are obtained already at the first active zone in the z direction. In some sense, it is fortunate that impulsive acceleration makes the flow essentially supersonic despite the value of the v_z parameter, because otherwise their simulations would fall under the criticism that crossing the sonic point requires relaxing the constraints imposed by fiat at the disk BC by one degree of freedom (Bogovalov 1997).

mass loading, and numerically the more convenient.

Comparing again with the results of this chapter, the different typical time of appearance, the different mechanism and evolution, and, most obvious, the opposite dependence on the value of mass loading, point out that the intermittent mechanism presented here is distinct from that presented in OP99 and Ouyed & Pudritz (1997a).

4.4 Conclusions

A technique to study launching from a finite disk was presented. Two kinds of flows were observed, steady and unsteady, depending on the mass loading ρv_z for a given value of B_z. Collimation was still observed, despite having a finite disk. The intermittent case may be relevant to those astrophysical jets showing some degree of intermittency and knots, such as the FRI radio galaxy M87 or the microquasar GRS1915+105.

The physical cause of this intermittency is the sub-Keplerian speed of the material close to the disk. Its presence is related to the amount of mass being loaded into the fieldlines; when it is excessive, the wind cannot launch it smoothly. This sub-Keplerian mechanism resembles the Uchida & Shibata (1985) simulations, where a similarly unsteady situation was assumed as an initial condition. However, there the origin of the sub-Keplerian flow was not simulated, and the initial state could not be reproduced at the end of the run, making the mechanism useful to produce a single pulse. The resemblance is probably closer to Bell & Lucek (1995), who obtain a sub-Keplerian rotation and a corresponding pulse of launching from more generic conditions (§1.2.7). The intermittent mechanism presented here can authentically be called "pulsed," as the configuration is able to reproduce itself after the material is launched.

For each magnetic field profile $B_z(R)$ on the disk, there is a maximum mass loading $j_{\max}$. which allows a smoothly accelerating jet. An angle-dependent feedback mechanism, based on the magnetocentrifugal model, limits the mass loading to this maximum value, allowing a smooth jet to flow. The existence of this feedback mechanism hints that $j_{\max}$ might be a more probable value than other discharge rates: if this is the case, then the profile of $B_z(R)$ helps to determine the mass loading j through the requirements of the Blandford & Payne angle $\theta = 30°$ and of keeping the process smooth.

The steady flows presented here have been simulated up to a very large height, equal to 100 times the radius of the disk. In the case of young stars, where the magnetically coupled disk is expected to have a radius $R_D \sim 1$AU, this corresponds to a height of 100AU, already close to the possibilities of observation, bridging the gap between the model and the data.

Fig. 4.1 *Finite disk launching: reference run.*

Surface of constant $M_{AT} = 0.5$, *1, and 2 in solid black (the fast surface thicker); surfaces of constant* $M_A = 0.5$, *1, and 2 in black dashes (the Alfvén surface thicker); surfaces of of constant* $-B_\phi/B_p = 1$, *2 in grey* ($-B_\phi/B_p = 1$ *thicker); fieldlines in black dots. The region painted in grey is influenced by the axial injection; the region in darker grey is out of steady state, and should be disregarded.*

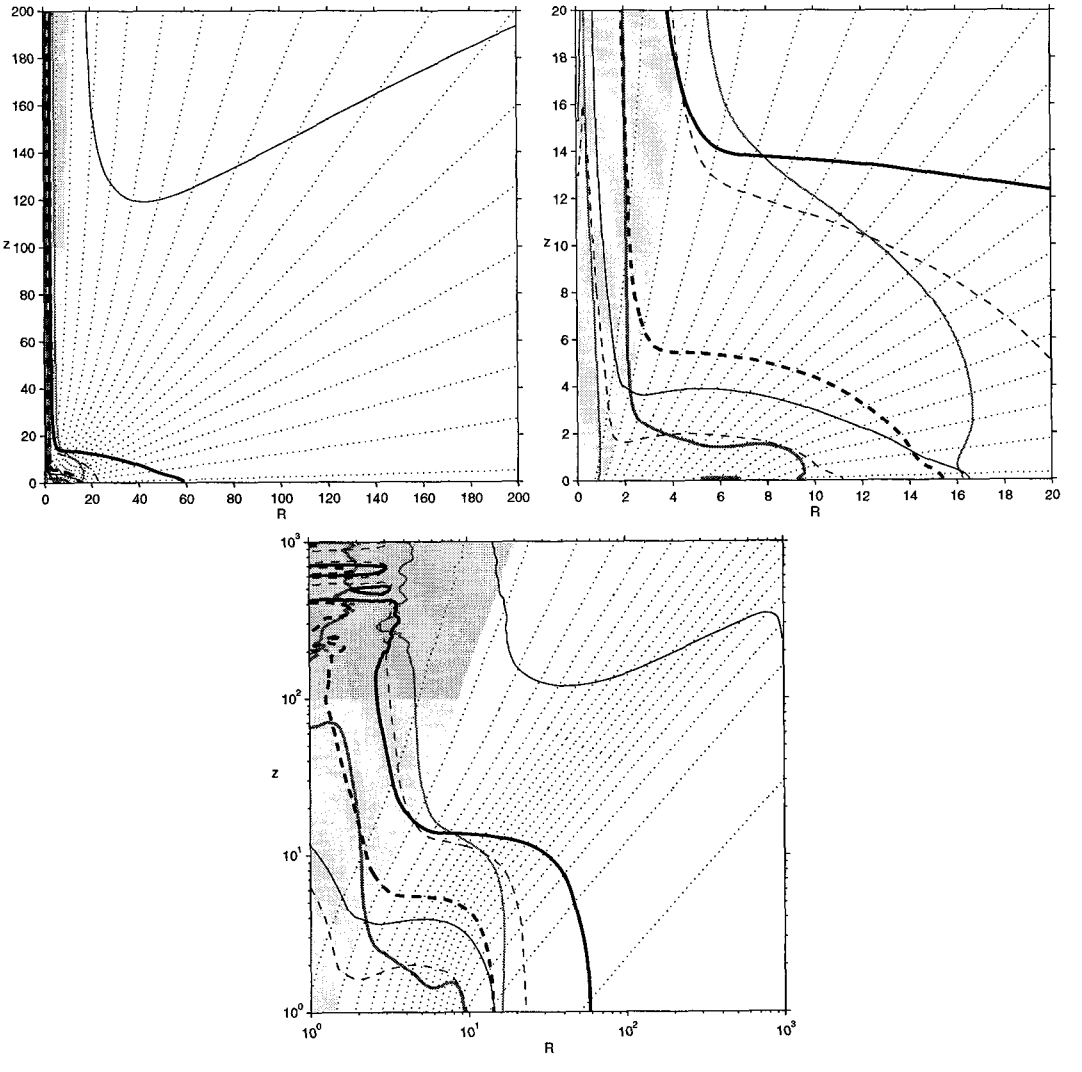

Fig. 4.2 *Finite disk launching: reference run. Density profiles are shown in solid black, spaced logarithmically by half decades (full decades in thicker lines, and the value $\rho = 10^{-1}$ even thicker). Level surfaces of v_p and v_z in black dashes and grey lines, respectively, taken at the values 0.5, 1.0 and 1.5; value 1.0 drawn thicker. fieldlines in black dots. The region painted in grey is influenced by the axial injection; the region in darker grey is out of steady state, and should be disregarded.*

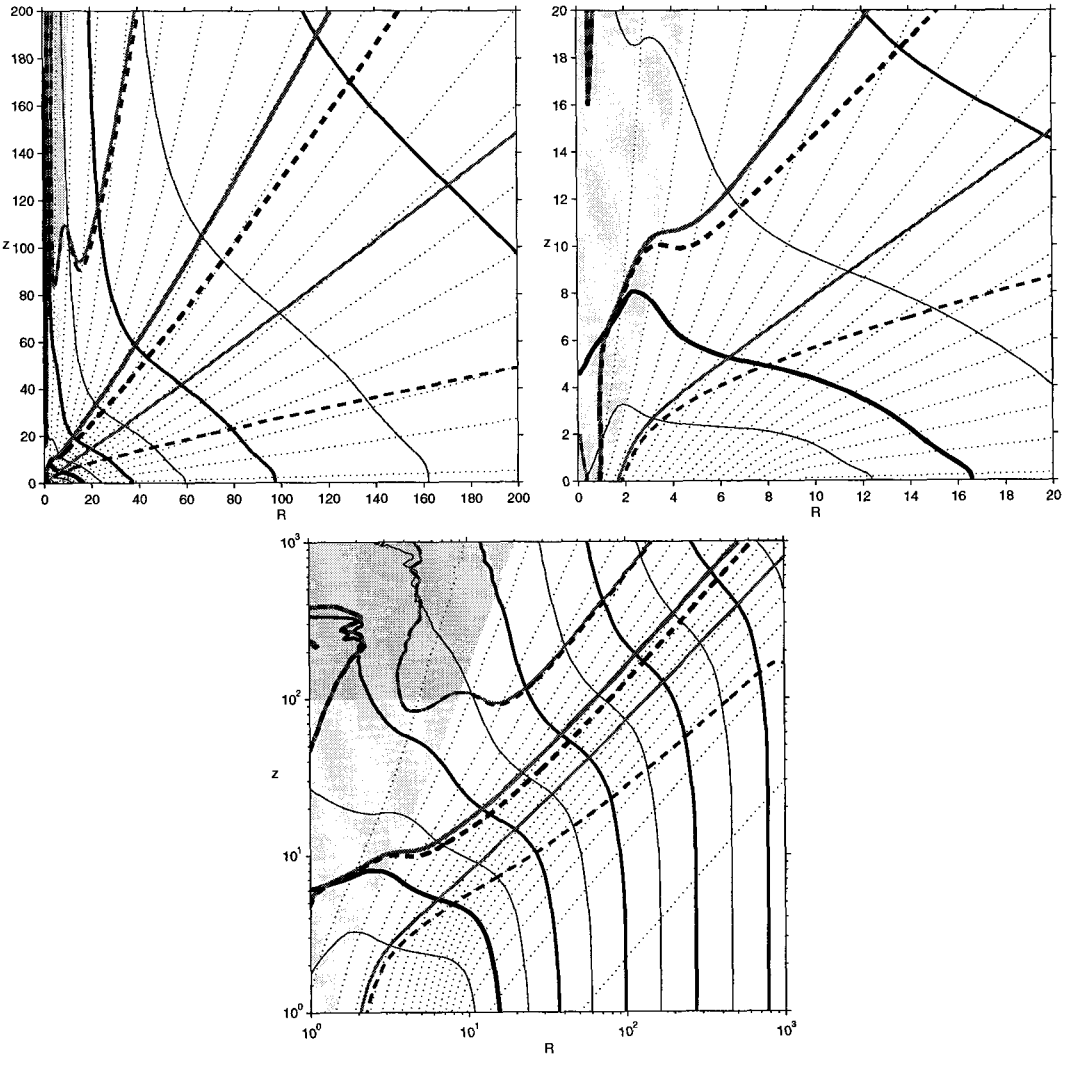

Fig. 4.3 *Finite disk launching: reference run. Values of the velocities v_p (grey) and v_z (black), at the altitudes $z = 900$ (solid), $z = 500$ (dashes), $z = 200$ (dot-dashes), and $z = 100$ (dots)*

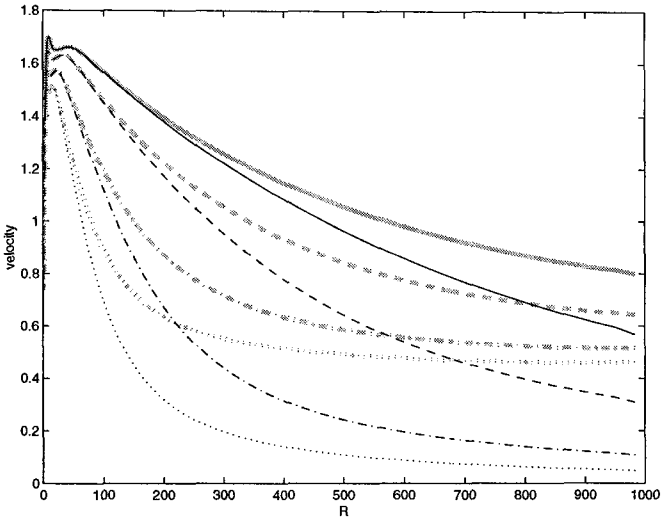

Fig. 4.4 *Finite disk launching: reference run. Lever arm ratio R_A/R_F, calculated at the disk surface using Mestel's theorem $R_A^2 = l/\Omega$.*

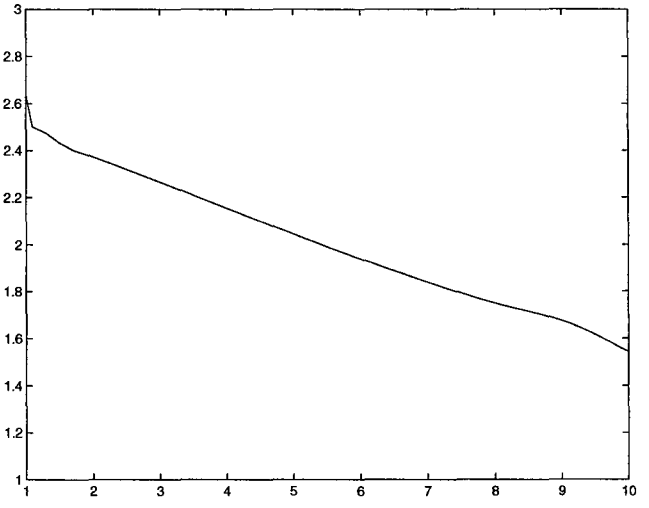

Fig. 4.5 *Finite disk launching: reference run. Values of* ρR^2 *and* ρr^2 *at the altitudes* $z = 900$ *(solid),* $z = 500$ *(dashes),* $z = 200$ *(dot-dashes), and* $z = 100$ *(dots)*

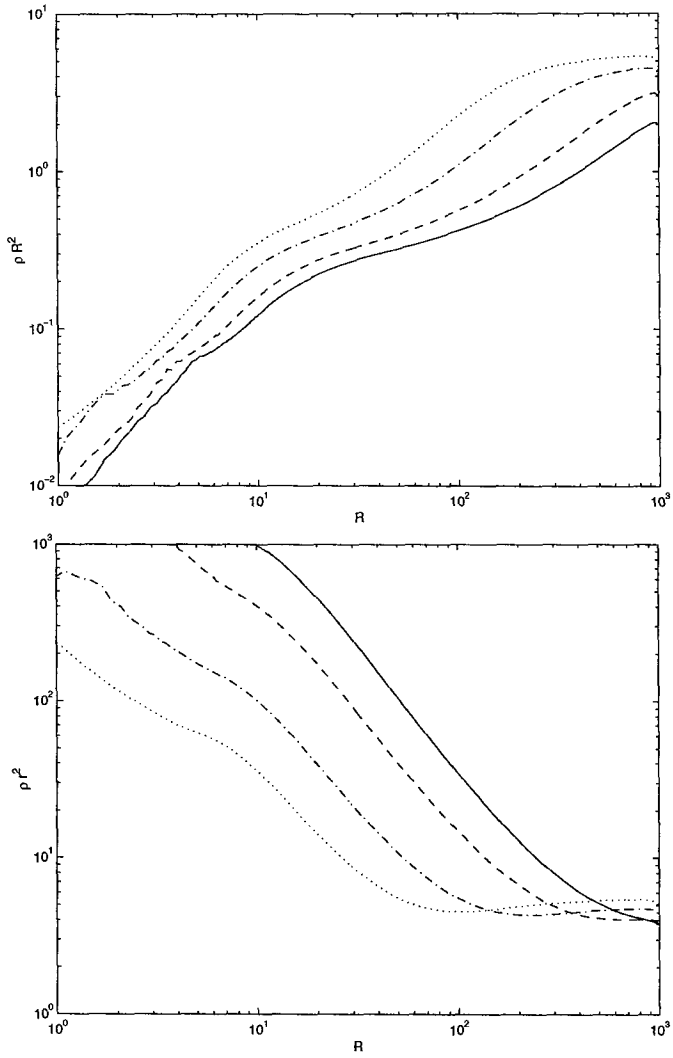

Fig. 4.6 *Launching of a jet with $j = \rho v_z$ flat at the axis. The two panels show hydromagnetic and hydrodynamic quantities, with the lines coded as in Figs. 4.1 and 4.2, respectively.*

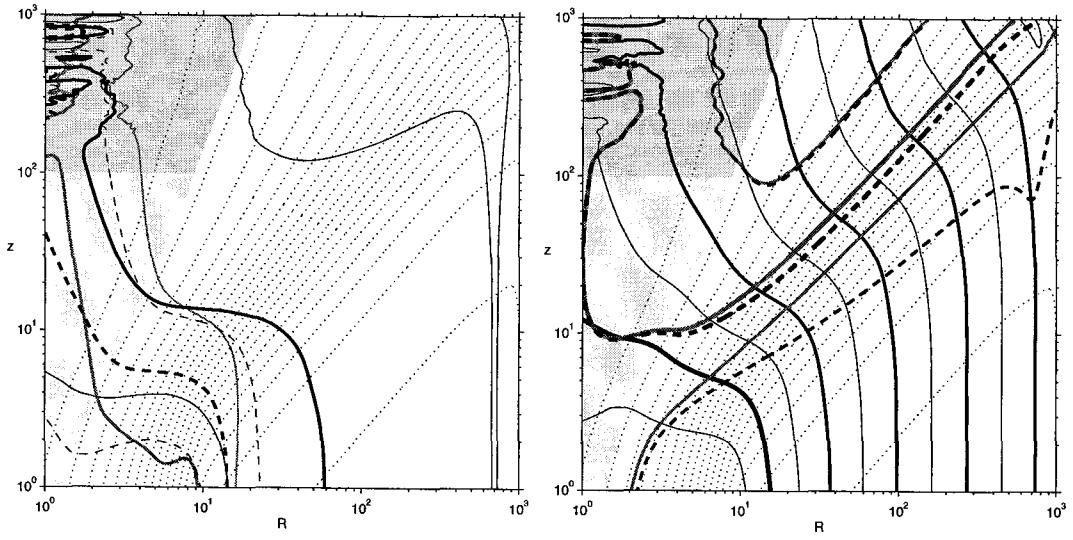

Fig. 4.7 *Launching of a jet with ρ flat at the axis. The two panels show hydromagnetic and hydrodynamic quantities, with the lines coded as in Figs. 4.1 and 4.2, respectively.*

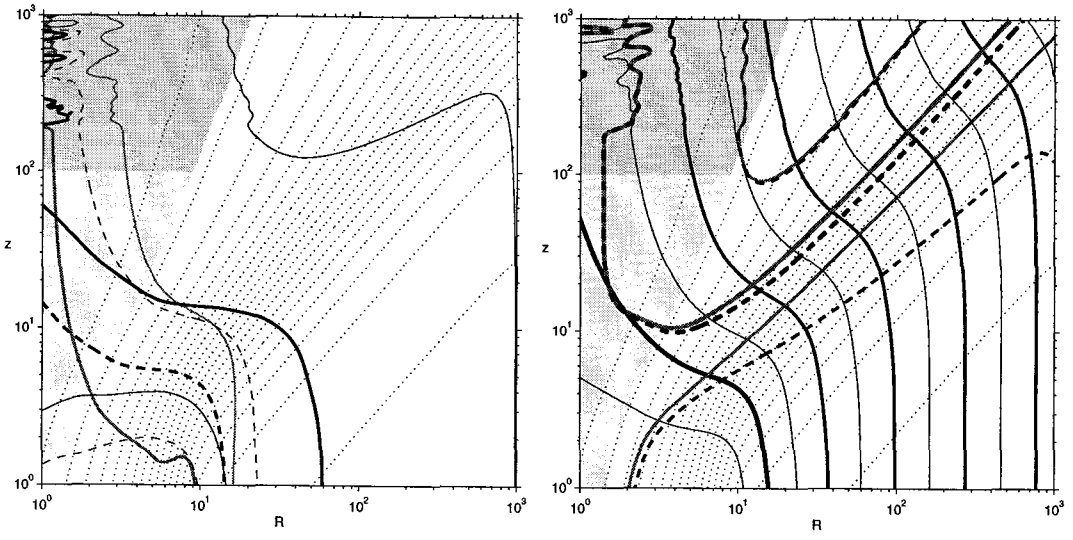

Fig. 4.8 *Six simulations: (a)* $e_b = 1.5$, $e_j = 0.5$; *(b)* $e_b = 1.5$, $e_j = 1.5$; *(c)* $e_b = 1.5$, $e_j = 2.5$; *(d)* $e_b = 1.5$, $e_j = 3.5$; *(e)* $e_b = 2.0$, $e_j = 1.5$ *and (f)* $e_b = 2.5$, $e_j = 1.5$. *Hydromagnetic quantities are shown with lines coded as in Fig. 4.1.*

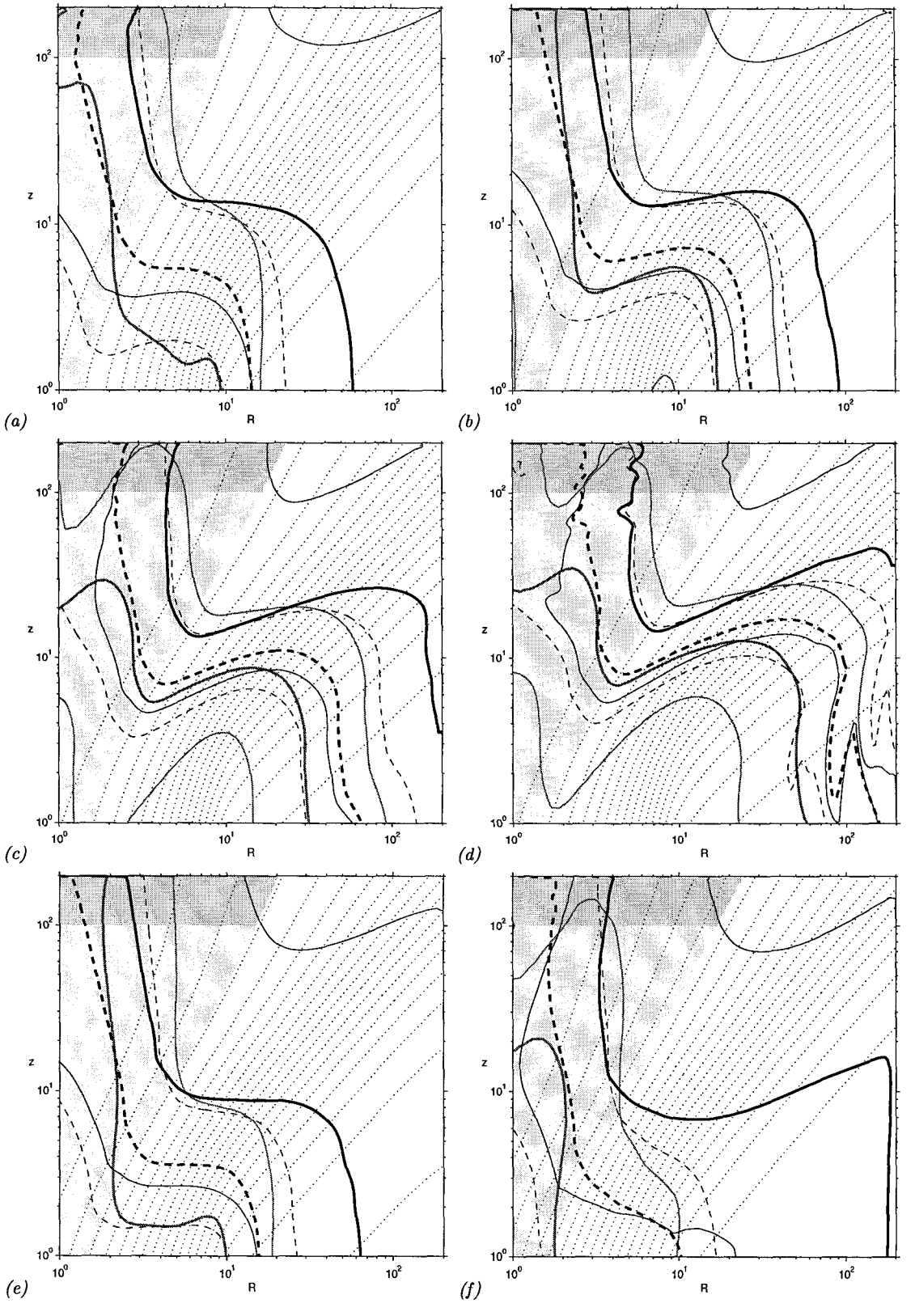

Fig. 4.9 *Six simulations: (a)* $e_b = 1.5$, $e_j = 0.5$; *(b)* $e_b = 1.5$, $e_j = 1.5$; *(c)* $e_b = 1.5$, $e_j = 2.5$; *(d)* $e_b = 1.5$, $e_j = 3.5$; *(e)* $e_b = 2.0$, $e_j = 1.5$ *and (f)* $e_b = 2.5$, $e_j = 1.5$. *Hydrodynamic quantities are shown with lines coded as in Fig. 4.2.*

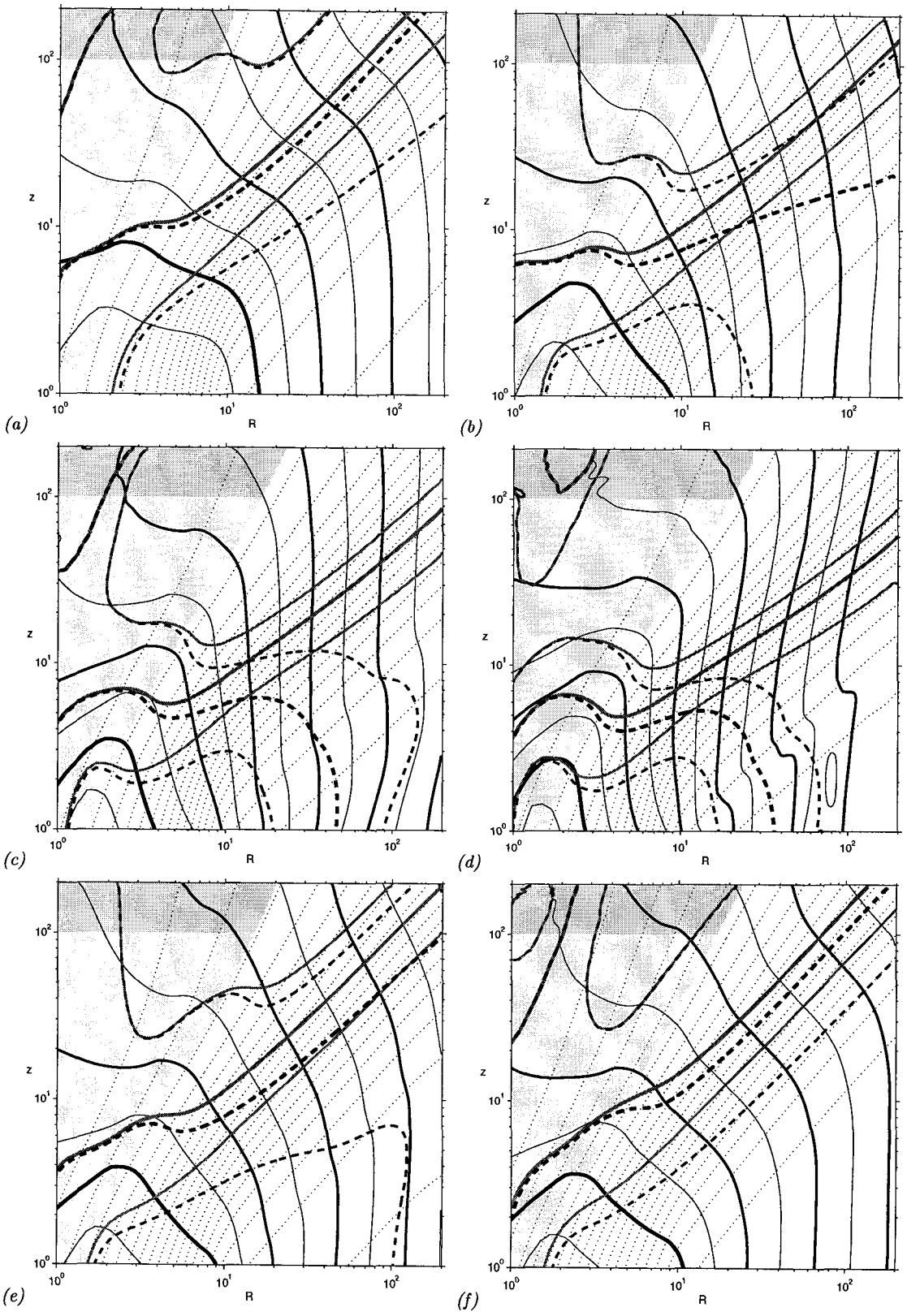

Fig. 4.10 *Values of $v_\phi/R\Omega$ for three simulations: the angle-dependent simulation in solid, an unsteady simulation in dashes, and a steady simulation in dot-dashes: these last two were taken from lines 1 and 2 in Table 4.1.*

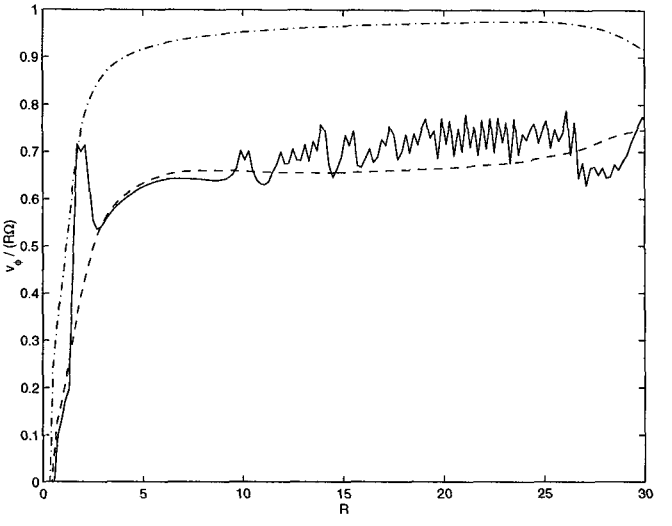

Fig. 4.11 *Values of $k = 4\pi\rho v_p/B_p$ for three simulations: the angle-dependent simulation in solid, an unsteady simulation in dashes, and a steady simulation in dot-dashes: these last two were taken from lines 1 and 2 in Table 4.1.*

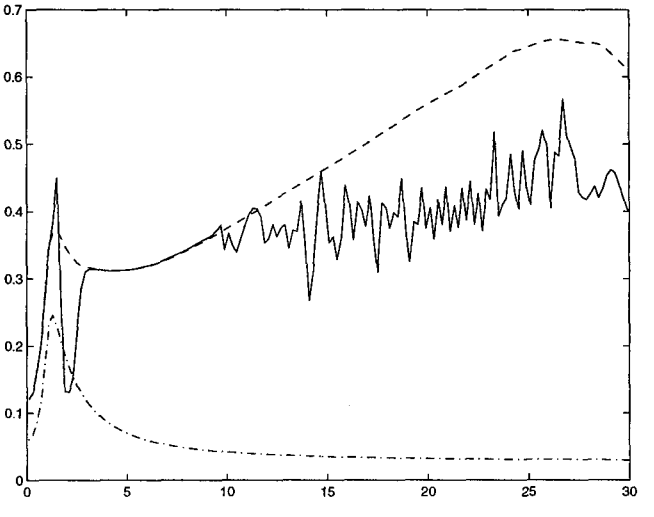

Chapter 5

3D Stability of the Launching Mechanism

5.1 Introduction

The magnetocentrifugal launching mechanism is intrinsically axisymmetric. Questions on its 3D stability against non-axisymmetric perturbations (specifically helical) have been a concern since it was proposed (Blandford & Payne 1982).

The magnetic field configuration required by the mechanism has been compared with some configurations used in plasma-confinement theory and experiment, such as the Z-pinch (with a mostly toroidal field), θ-pinch (with a mostly axial field), and the screw-pinch (having both magnetic components). These plasma-confinement mechanisms are known to be unstable against a variety of modes distorting the plasma column, which for $m > 0$ are called *kink modes*.

The question asked in this chapter is whether these kink modes are able to drive an instability during the formation phase of the jet. Arguments in favor of this kind of instability in jets have been put forward by Begelman (1998), relying on an expected large fraction $|B_\phi/B_p|$. Simulations by Hardee et al. (1994, 1995, 1997, 1999) also point out in that direction.

However, the magnetocentrifugal mechanism implies a large fraction $|B_\phi/B_p|$ at large altitude, but not during early launching. For instance, Königl & Pudritz (2000) present the estimation $|B_\phi/B_p| \sim 1$ at the Alfvén surface, close to the end of the main acceleration of the wind for cold flows. This make the field picture resemble less the Z-pinch and more the θ-pinch, which is more stable. Also the presence of intense acceleration, velocity shear and fast rotation distinguishes these astrophysical flows from the corresponding static-equilibrium plasma-confinement configurations; these differences in the flow field are expected to be stabilizing (Arber & Howell 1996; Hameiri 1981,1981). Other formation mechanisms related to the magnetocentrifugal picture, such as Bell & Lucek (1995), or the intermittent mechanism shown in §4.3, have important axial magnetic fields, weakening again the case for the kink instability: for instance, the 3D stability simulations by Lucek & Bell (1997) were robust against kink instabilities. The answer from theory about the instability of the launching configuration is unclear, making simulations necessary.

5.2 Method

The simulations presented in this chapter start from an axisymmetric steady state configuration, similar to the ones found in §4.2, and add to it an $m = 1$ perturbation of the magnetic field to the initial state. However, the boundary conditions have been kept unperturbed and axisymmetric, because the intention here is studying stability against perturbations of the initial conditions, and not against a small but persistent perturbation at the boundary.

5.2.1 Perturbation

The perturbation has been designed to ensure that the divergence of the magnetic field is kept to zero. A perturbative field $\mathbf{B}_1$ was added to the main field $\mathbf{B}_0$, such that

$$\mathbf{B}_1 = \nabla \times (\xi \times \mathbf{B}_0) \ , \tag{5.1}$$

with ξ a small displacement vector. In order to seed a kink instability with $m = 1$, this displacement was chosen to be $\xi = d \sin(2\pi z/\lambda)\,\hat{x}$, parallel to the x-axis, with d and λ constants with units of length characterizing the perturbation.

5.2.2 Grid

3D cylindrical simulations have the problem that the azimuthal grid spacing close to the axis, $R\,d\phi$, can be very small, leading to a very small timestep Δt, given by the Courant condition required for numerical stability, $\Delta t < \Delta x/v$, where v is at least the maximum of the sound, flow, and Alfvén speeds. The most usual response to this is to do the 3D simulation in Cartesian coordinates. However, when this was tried, the boundary conditions at the outer surfaces and at the disk became too complicated. Even more problematic for this study, both the boundaries and the discretization introduced a permanent, artificial $m = 4$ perturbation.

Therefore a cylindrical coordinate system was preferred. The fact that the flow is super-Alfvénic before hitting the outer surfaces should minimize any effects of the outer boundary condition. Timestep problems were alleviated by using low resolution in R close to the axis and in ϕ. The computational cost of doing long-term 3D simulations would probably not have allowed a much higher resolution inside the given constraints of time and computer allocation. It is also helpful that the initial unperturbed configuration was chosen so as to have a small Alfvén speed at $R = 0$. For the purpose of future research at higher resolution, a system of coordinates where the number of azimuthal zones decreases for small radii may be useful. This way high overall resolution might be kept while having a moderate timestep.

5.3 Results

Six different simulations were performed, varying the amplitude and wavelength of their perturbation, and the resolution of the grid. The unperturbed system and the disk boundary conditions were defined by the parameters $\Omega_0 = 1$, $r_g = r_b = r_{vi} = r_{vo} = 1$, $B_{z0} = 4\sqrt{4\pi}$, $e_b = 1.5$, $v_{z0} = 1.7$, $f_{vo} = 0.1$, $e_{vi} = 2$, $e_{vo} = 1$, $\nu = 2$, $c_s = 0.0002$, and $\gamma = 5/3$. The finite disk has outer radii $R_D = 10$ and $R_{D1} = 8$, as in the run §4.2.1.1. The density was kept flat, with $\rho(R, z = 0) = 1$ over all the finite disk. An additional parameter, $r_{bf} = 1.8$, fixed the magnetic field at $z = 0$ to have a flat constant value between $R = 0$ and $R = r_{bf}$. This was done to reduce the Alfvén speed close to the axis, making the Courant condition more favorable.

Two different grids were used. The lower resolution grid has a z axis with 20 equally spaced zones from $z = 0$ to $z = 8$, followed by 50 ratioed[1] zones from $z = 8$ to $z = 180$, with a minimum step $\Delta z_{\min} = 0.4$, and a constant ratio $\Delta z_{i+1}/\Delta z_i \approx 1.0716$; an R axis with 3 equally spaced zones from $R = 0$ to $R = 2.4$, 24 zones equally spaced zones from $R = 2.4$ to $R = 12$, and 45 ratioed zones from $R = 12$ to $R = 180$, with $\Delta R_{\min} = 0.4$ and a ratio $\Delta R_{i+1}/\Delta R_i \approx 1.0827$; and 64 zones in the azimuthal direction, extending from $\phi = 0$ to $\phi = 2\pi$. The higher resolution grid differs only in having a higher resolution for the inner R axis. This axis is now defined by 30 equally spaced zones from $R = 0$ to $R = 12$, and 45 ratioed zones from $R = 12$ to $R = 180$, these last defined with the same ratios as for the other grid.

Perturbations were imposed with $d = 0.2$ and $d = 1.0$, with wavelengths $\lambda = 10$, 5 and 2.5. The magnetic field was decomposed into azimuthal components $\mathbf{B}_m e^{im\phi}$ using a Fast Fourier Transform algorithm, and the energy was calculated for each of these components. Figures 5.1– 5.3 show how in all the six simulations, the energy of the initial perturbation was initially concentrated in the $m = 1$ component. This component decayed in time instead of growing, as expected in case of a kink instability; this decay features an initial sharper drop. The magnetic energies corresponding to the first few values $m > 1$ have an initial rapid expansion, probably at the expense of the initial fall in $m = 1$, but later also decay, to some energy value typically lower than that of $m = 1$. In these simulations, the energy of the $m \neq 0$ modes did not tend to zero for large t, but rather to a small non-zero value: this might be due to resolution effects. In any case, there was no sign of any long term growth of these modes: the kink instability was not observed.

The evolution of the perturbations is presented by showing 3D images of the Alfvénic surface $v = B/\sqrt{4\pi\rho}$ (Figs. 5.5– 5.9). Note that this 3D-Alfvénic surface is different from both the Alfvén and fast surfaces defined in previous chapters: it has been defined so as to take all three components of the vectors equally, rather than being a critical surface of a steady-state solution. The unperturbed Alfvénic surface has the shape of a cone, with its axis coincident with the axis of rotation (Fig. 5.4);

[1] Each zone is wider than the previous one by a small constant factor.

the axis itself is however hollow, because of the relatively low magnetic field imposed by the flattening of the B_z profile. The perturbation starts by distorting this cone, giving it a helicoidal shape (time $t = 0$, Fig. 5.5). Later in time, the surface develops a hollow cocoon encircling the tip of the cone and the axis of rotation. This cocoon expands in both z and R, and at the same time it becomes thinner, especially at middle altitudes z (times $t = 5\pi$ and $t = 10\pi$, Figs. 5.6 and 5.7). This thinning of the cocoon is not uniform, producing hollow windows through which the tip of the cone is visible (time $t = 15\pi$, Fig. 5.8). These windows enlarge, in some simulations shredding the cocoon into a ribbon-like structure (time $t = 20\pi$, Fig. 5.8(b)). In all the simulations, at some time the mid-height cocoon gets so thin that its upper tip breaks off, swept away towards $z \to \infty$. The Alfvén surface left behind is similar to the initial unperturbed solution, with the addition of a thin, cylindrical ring on top, which expands slowly as it diminishes in height and width (time $t = 20\pi$, Figs. 5.9).

The calculations presented here may be criticized based on a possible influence of the relatively low grid resolution. Low resolution is known to be dissipative, and it could mask some weakly unstable growth. Two resolutions were used to address this; it can be seen that the lack of instability stayed the same in both cases, with similar decay rates for the non-axisymmetric perturbation, and similar evolution of the perturbative features.

5.4 Conclusions

The simulations indicate that the energy of the $m \neq 0$ modes decreases in time, instead of increasing as it would be for a non-axisymmetric instability. It was expected that a strong instability would have found a way to manifest itself destructively, even against an artificial dissipation conceivably imposed by the grid.

This stability against kink perturbations must be compared against the simulations presented by Hardee et al. (1994, 1995, 1997, 1999) which indicate that 3D instabilities may grow in astrophysical jets. A few key differences in the physical models used may be the reason of the different result. Probably the most important difference is that their $z = 0$ boundary condition is not fixed in time and symmetric, but represents an ongoing precession of the jet at the origin: this produces a constant powering of the perturbation through a physical mechanism, as opposed to having only an initial perturbation, as treated in this thesis. Other differences include the confinement of the magnetic field by a fluid pressure that grows with radius (absent in this thesis, which deals with mostly cold jet flows), and their imposition of a preformed jet at the boundary condition instead of a simulation of the acceleration mechanism itself. The instability results of Begelman (1998) depend on the assumption of a magnetic field dominated by its toroidal component and ignoring all shear, which is not the case for the magnetocentrifugal mechanism before a point beyond the Alfvén surface.

Moreover, these studies, based on preformed jets, are more relevant to the propagation of the jet

at large distances than to the launching as presented here in this thesis. Acceleration and velocity shear during launching should have a stabilizing effect, which is lost in studies of preformed jets. However, even for the study of jet propagation, an expected power-law dependence of the fluid pressure with distance may change the stability properties, requiring a revision of some previous results.

Fig. 5.1 *Magnetic energy* $\int d^3r\,|\mathbf{B}_m|^2$ *of the various azimuthal components* $\mathbf{B}_m e^{im\phi}$ *as a function of time. Perturbation defined with* $d = 0.2$, $\lambda = 10.0$.

(a) Lower resolution

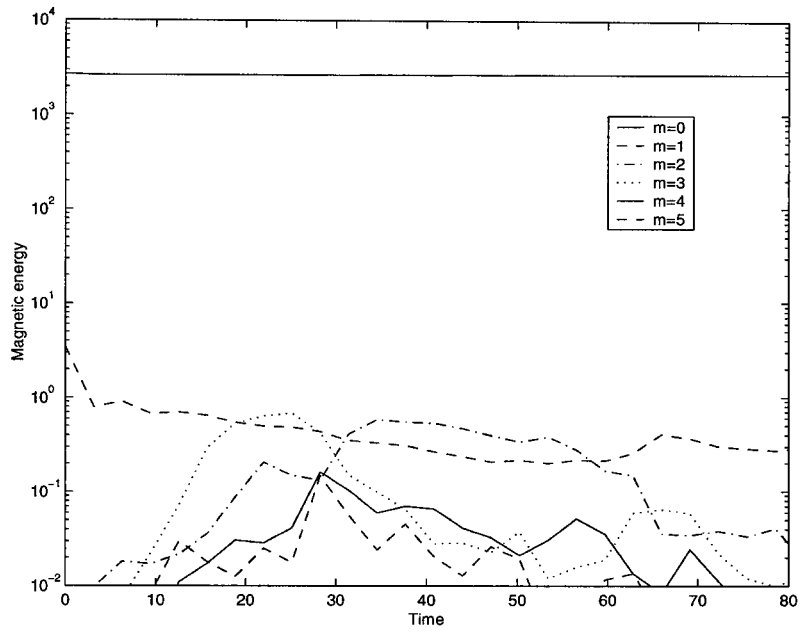

(b) Higher resolution

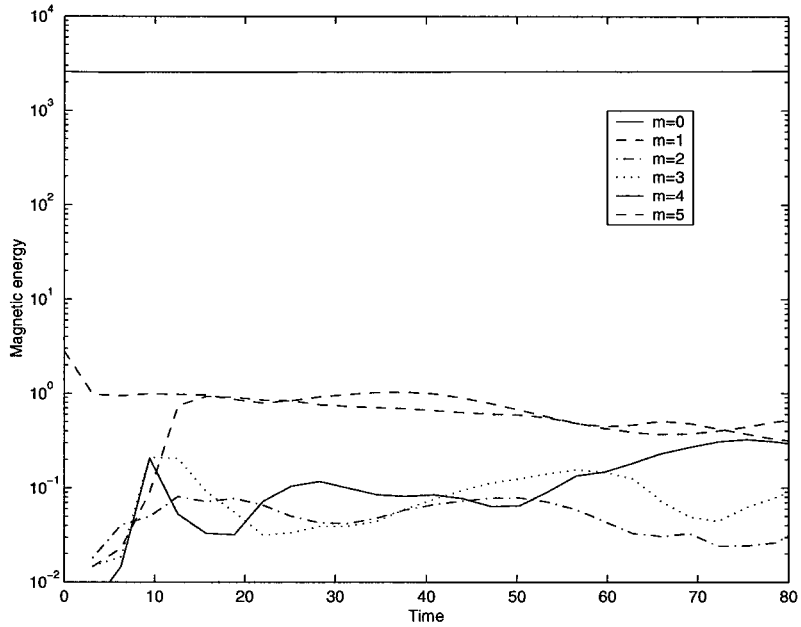

Fig. 5.2 *Magnetic energy* $\int d^3r\,|\mathbf{B}_m|^2$ *of the various azimuthal components* $\mathbf{B}_m e^{im\phi}$ *as a function of time. Lower resolution.*

(a) Perturbation defined with $d = 0.2$, $\lambda = 5.0$.

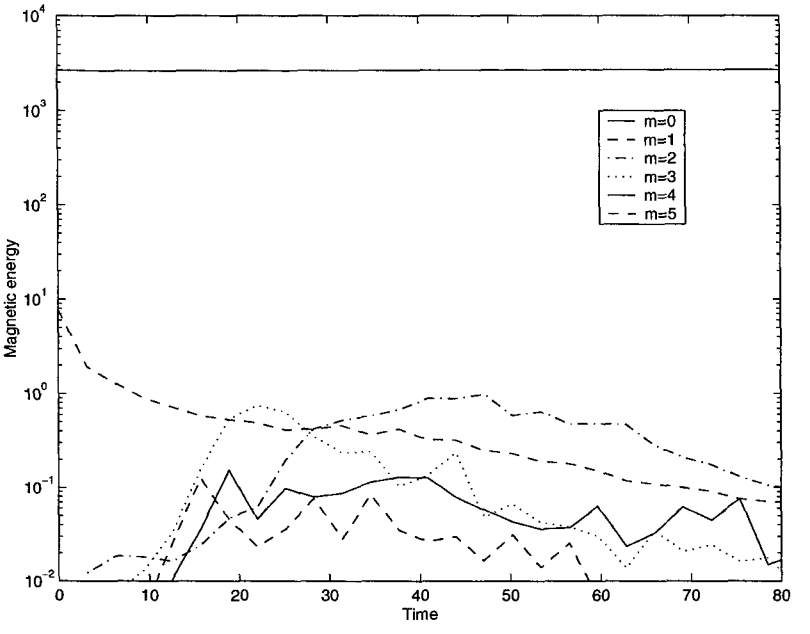

(b) Perturbation defined with $d = 0.2$, $\lambda = 2.5$.

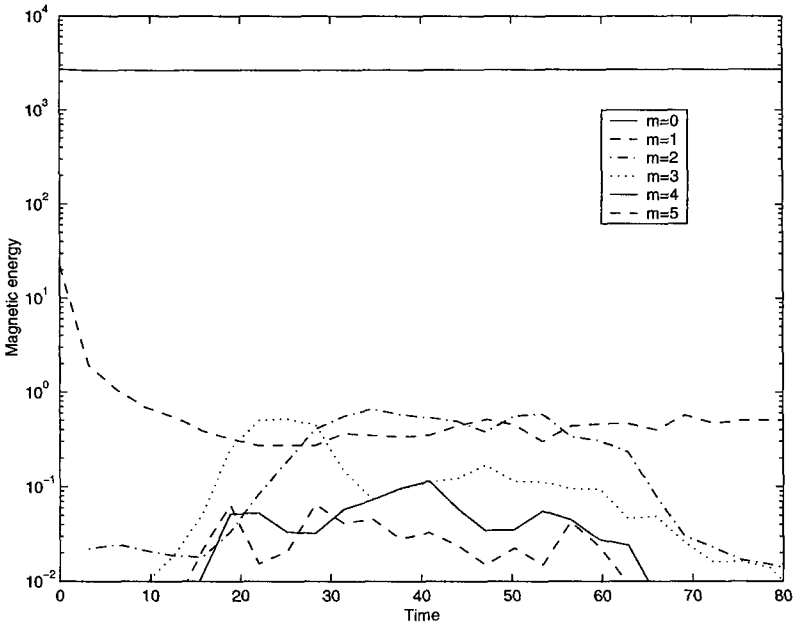

Fig. 5.3 *Magnetic energy* $\int d^3r\,|\mathbf{B}_m|^2$ *of the various azimuthal components* $\mathbf{B}_m e^{im\phi}$ *as a function of time. Perturbation defined with* $d = 1.0$, $\lambda = 10.0$.

(a) Lower resolution

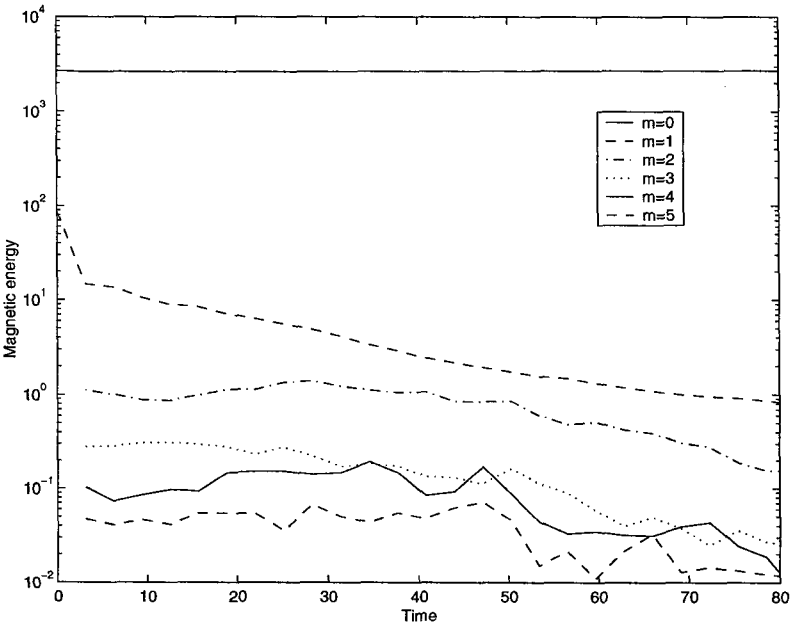

(b) Higher resolution

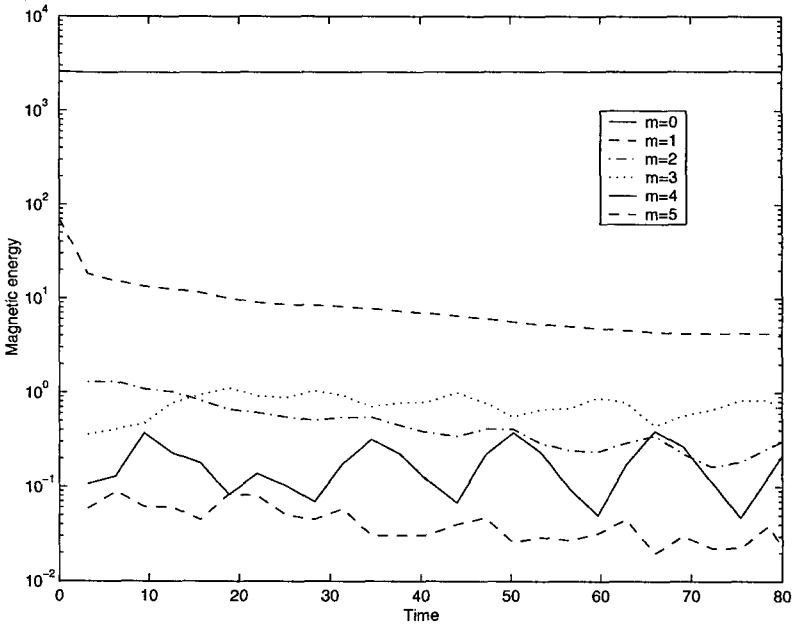

Fig. 5.4 *The unperturbed Alfvénic surface* $v = B/\sqrt{4\pi\rho}$, *at both resolutions.*

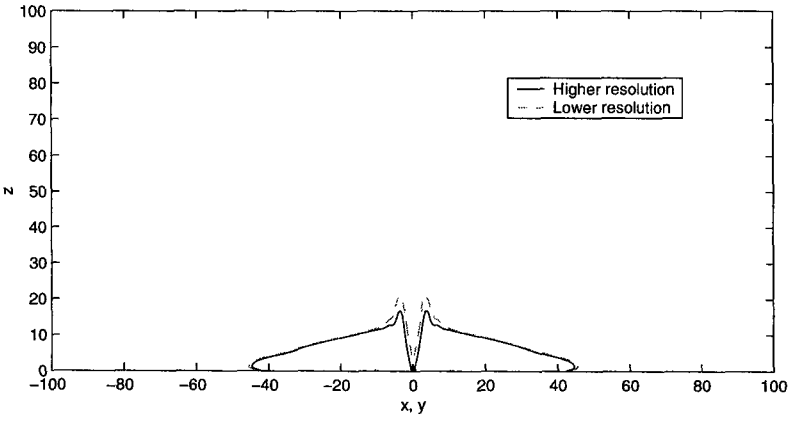

Fig. 5.5 *Alfvénic surfaces* $v = B/\sqrt{4\pi\rho}$, *at time* $t = 0$. *Higher resolution simulations.*

(a) Perturbation defined with $d = 0.2$, $\lambda = 10.0$.

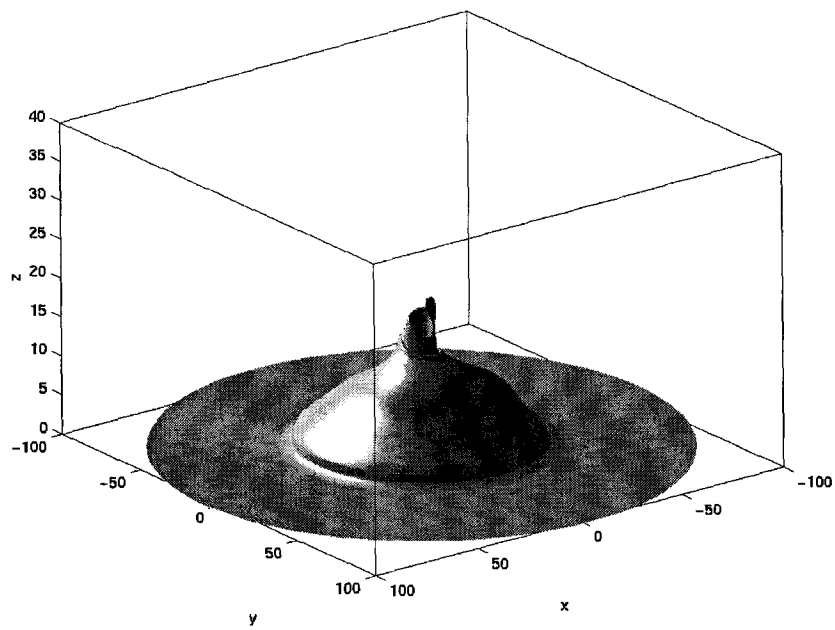

(b) Perturbation defined with $d = 1.0$, $\lambda = 10$.

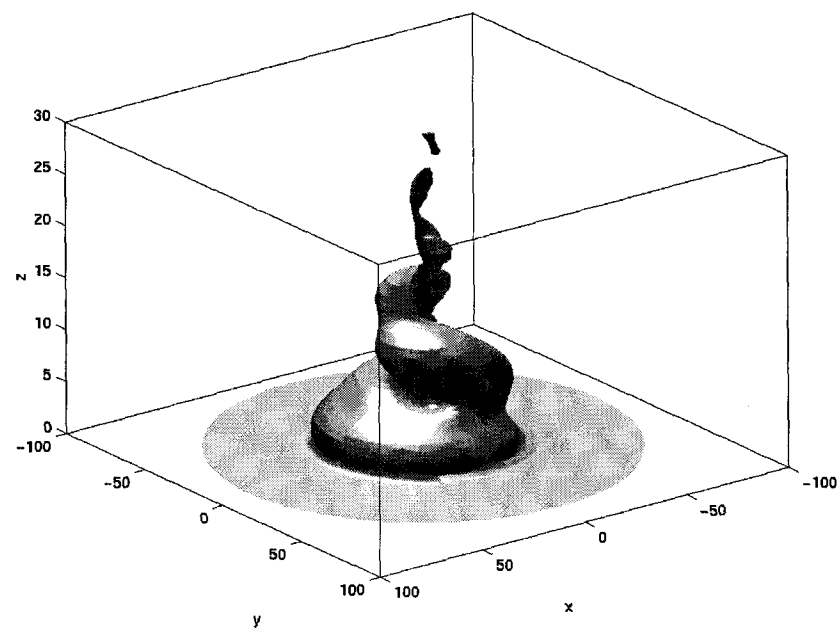

Fig. 5.6 *Alfvénic surfaces* $v = B/\sqrt{4\pi\rho}$, *at time* $t = 5\pi$. *Higher resolution simulations.*
(a) Perturbation defined with $d = 0.2$, $\lambda = 10.0$.

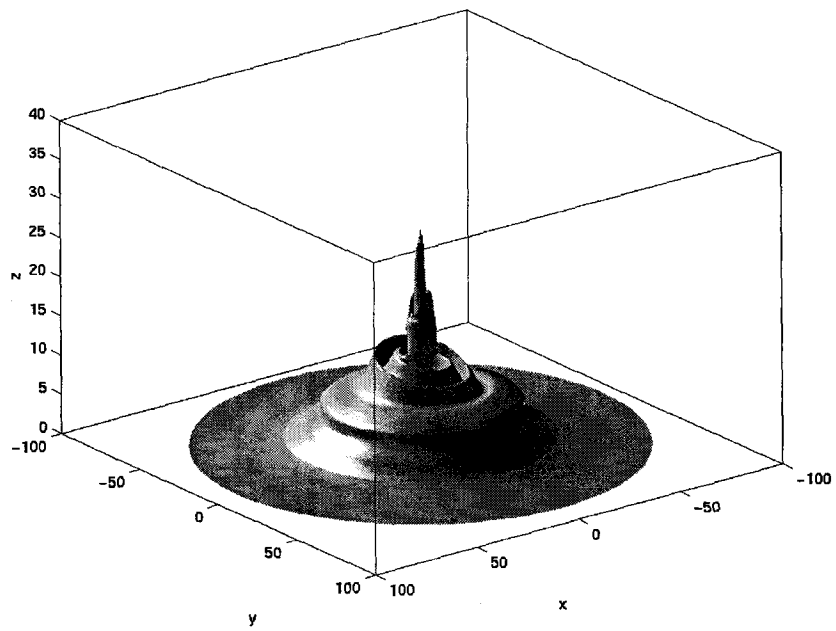

(b) Perturbation defined with $d = 1.0$, $\lambda = 10$.

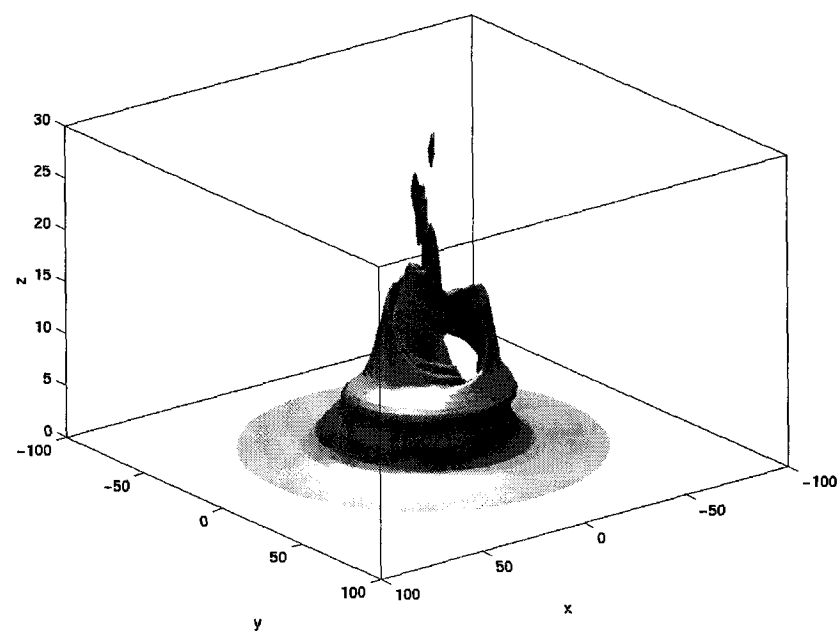

Fig. 5.7 *Alfvénic surfaces* $v = B/\sqrt{4\pi\rho}$, *at time* $t = 10\pi$. *Higher resolution simulations.*
(a) Perturbation defined with $d = 0.2$, $\lambda = 10.0$.

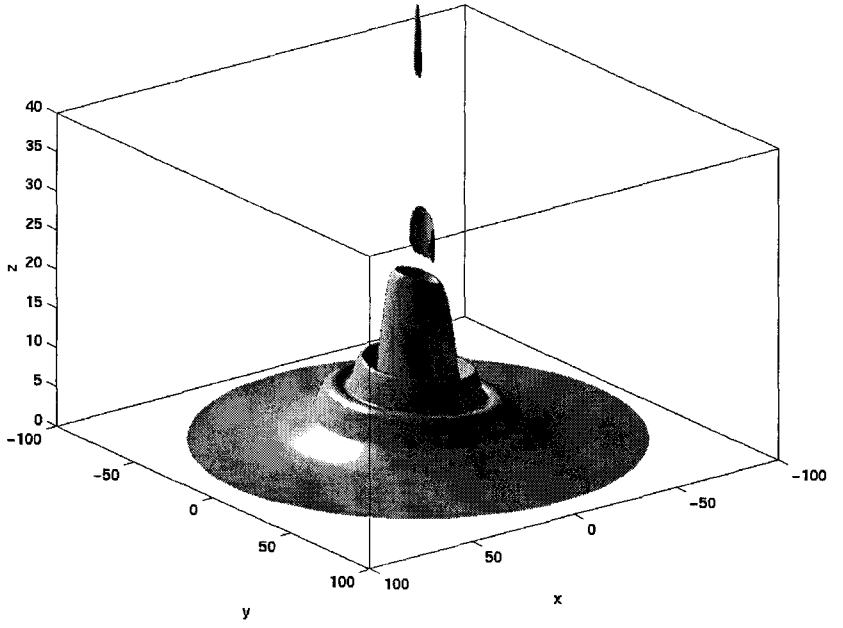

(b) Perturbation defined with $d = 1.0$, $\lambda = 10$.

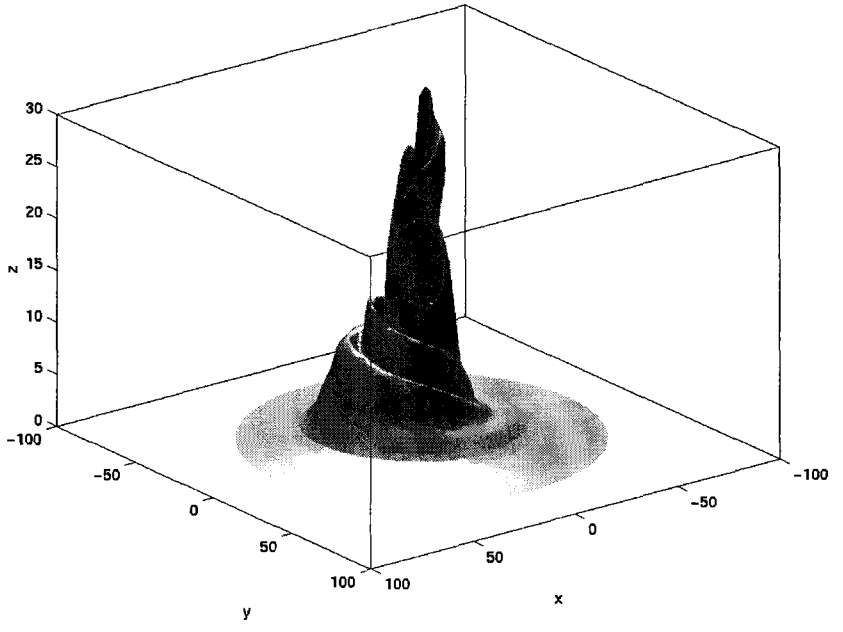

Fig. 5.8 *Alfvénic surfaces* $v = B/\sqrt{4\pi\rho}$, *at time* $t = 15\pi$. *Higher resolution simulations.*

(a) Perturbation defined with $d = 0.2$, $\lambda = 10.0$.

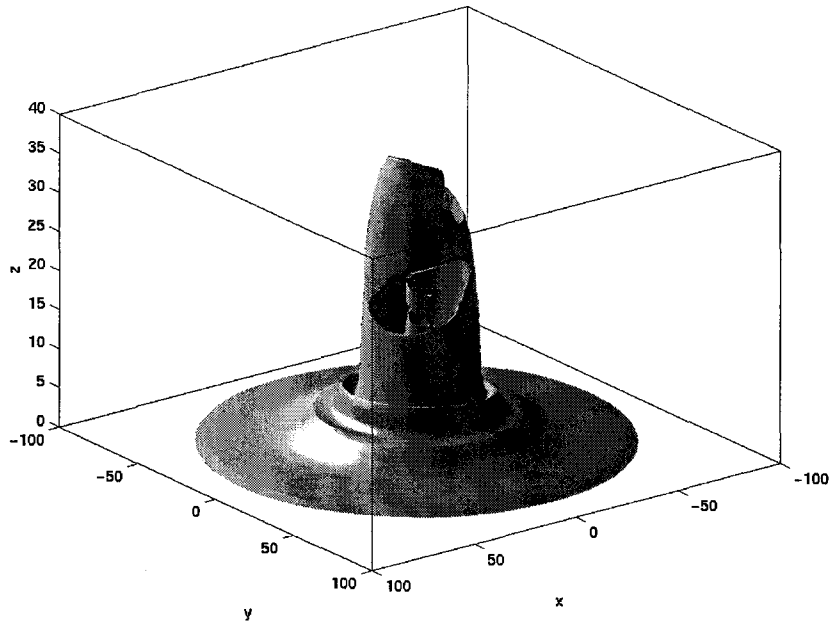

(b) Perturbation defined with $d = 1.0$, $\lambda = 10$.

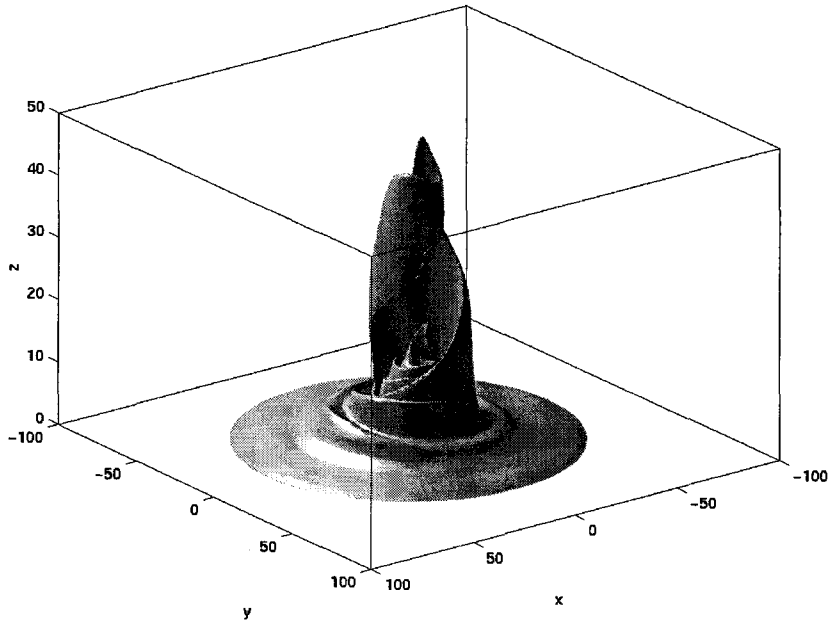

Fig. 5.9 *Alfvénic surfaces $v = B/\sqrt{4\pi\rho}$, at time $t = 20\pi$. Higher resolution simulations.*

(a) Perturbation defined with $d = 0.2$, $\lambda = 10.0$.

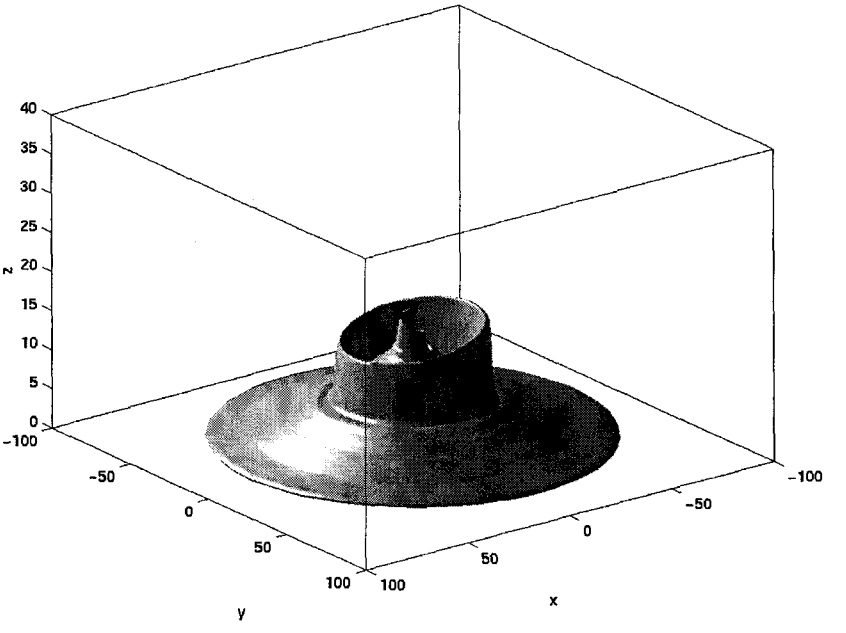

(b) Perturbation defined with $d = 1.0$, $\lambda = 10$.

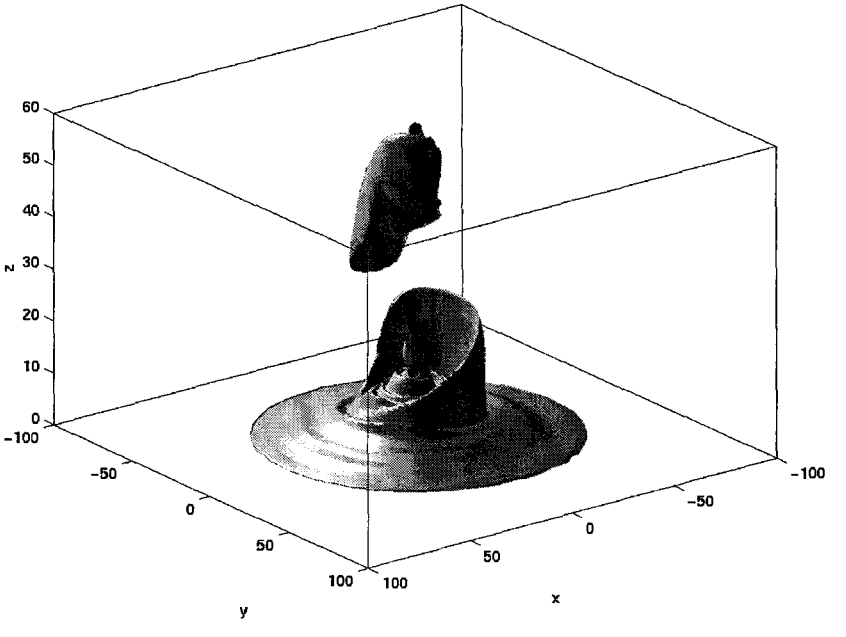

Chapter 6

Solar Wind

6.1 Introduction

The solar wind is a fast, mostly radial outflow of plasma from the Sun (400-800kms^{-1}) with a mass flux of $\sim 2\times 10^{-14} M_{\odot}$ per year. It is ionized, composed mostly of protons and electrons, with an appreciable component of α particles, and a small amount of heavier ions. Biermann (1951) postulated its existence based on the observation of comet tails, following the suggestion by Hoffmeister (1944) that solar particles rather than solar electromagnetic radiation were responsible for the shape of the comet tails. Parker (1958) formulated the hydrodynamic theory of this flow, showing that under wide circumstances a thermally driven outflow was inevitable. Weber & Davis (1967) extended these results by taking into account magnetic forces and a flow v_{ϕ} in the azimuthal direction, initially disregarded by Parker; their prediction for the angular momentum loss of the Sun is substantially larger than the initial numbers given by Parker. These outflow theories were shown in §1.2.2.1.1 and §1.2.2.1.2.

The calculations presented in this chapter start with solar wind observations at high latitudes acquired by the satellite Ulysses. Average fields and parameters are obtained from the data, giving a simple, analytical one-fluid representation of the flow. This analytic model is used as a basis for a 2D simulation that attempts to infer conditions close to the Sun.

6.2 Ulysses mission and results

6.2.1 The orbit

The Ulysses satellite has explored the heliosphere at high solar latitudes, between 80°S and 80°N, at a distance from the Sun between ~1.3 and ~5 AU. The mission was launched from the Earth on 6/Oct/1990. It arrived at Jupiter on 8/Feb/1992, where it used the gravitational field of the planet to accelerate out of the ecliptic plane; this made the mission to polar latitudes possible.

The maximum South latitude of $\Theta = -80.2°$ was achieved on 13/Sep/1994, at a solar distance $r = 2.28$AU. Near its perihelion, Ulysses performed a fast sweep from pole to pole. It crossed the solar equator ($\Theta = 0°$) on 4/Mar/1995, achieved its perihelion on 12/Mar/1995 (at a solar distance $r = 1.34$AU and latitude $\Theta = 6.1°$), and reached its maximum northern latitude of $\Theta = 80.2°$ on 31/Jul/1995. From there the spacecraft continued its northern sweep towards its aphelion, which

it reached on 17/Apr/1998 ($r = 5.41$AU, $\Theta = -6.1°$). Presently Ulysses is performing its second southern sweep, with a latitude of $\Theta = -43.6°$, at a distance from the Sun of $r = 4.08$AU on 20/Jan/2000; it is still in the aphelion side of its second orbit, gaining southern latitude while it approaches the Sun. The data used in this chapter are taken from the high latitude portions ($|\Theta| \geqslant 30°$) of the first southern and northern sweeps, obtained during the quiet portion of the 11 year solar cycle.

The first orbit and the approach to Jupiter are shown in Fig. 6.1.

6.2.2 Data

The hydrodynamic and thermal data used here were obtained by the experiment SWOOPS (principal investigator Dave J. McComas) and described in Bame et al. (1992). The magnetic data were obtained by the experiment VHM/FGM (principal investigator A. Balogh) and described in Balogh et al. (1992). These and other heliospheric data are available at the NSSDC Space Physics web site, `http://nssdc.gsfc.nasa.gov/space/` and at COHOWeb, `http://nssdc.gsfc.nasa.gov/cohoweb/`. The data present at the NSSDC ftp and web sites include the density, temperature, the 3 components of the vectors of velocity and magnetic field, and orbital data. The heliospheric coordinates used are the distance from the Sun center r, the latitude measured from the solar equator $\Theta \equiv 90° - \theta$, and the longitude ϕ. Vector components have been taken along these same coordinate directions.

It is convenient to show the data as functions of time, latitude and radial distance, separating the high latitude data into four datasets. Those four are, by chronological order: the southern aphelion sweep (after achieving a latitude $-30°$ for the first time, but before reaching maximum latitude), the southern perihelion, the northern perihelion, and the northern aphelion. No data from the present second southern aphelion sweep are presented.

In all the figures showing Ulysses data in this chapter, southern data are shown in gray, and northern in black; perihelion data points are shown with thicker dots and lines than those taken at the aphelion. This separation helps to keep track of the fact that each latitude in absolute value was visited four times, at two widely different distances from the Sun. Unless it is explicitly stated otherwise in the caption, only high latitude data ($|\Theta| \geqslant 30°$) have been kept; the few plots including low latitude data show also the initial approach from the Earth to Jupiter in light gray. Most of the data in the figures have been averaged over 120-hour periods: other averaging is announced in the corresponding caption. In many of the data figures, the ordinate axis of the plot is centered on a trimmed mean, with the lowest and highest 1/8 of the data excluded, and its extension is calculated as six times the interquartile range of the data. The caption of these figures mentions that the ordinate axis was calculated, instead of taken directly from the full data range.

The radial magnetic field at high latitude is close to that of a split monopole, with $B_r r^2 = 3.2 \times 10^{-5}$G AU^2 sign($\Theta$) (Fig. 6.2). The radial velocity of the solar wind varies substantially between

high and low latitudes, as shown in Fig. 6.3. Considering only the high latitude part of the data ($|\Theta| \geqslant 30°$) the typical radial speed is $v_r \sim 800 \mathrm{km\,s^{-1}}$, largely independent of latitude and radial distance (Fig. 6.4). The mass loss rate per solid angle $\rho v_r r^2$ at high latitude is shown in Fig. 6.5. Its value of $\rho v_r r^2 \sim 9 \times 10^{10} \mathrm{g\,s^{-1}}$, is also largely independent of latitude and distance from the Sun and when combined with the previously estimated speed v_r gives $\rho r^2 \sim 5 \times 10^{-24} \mathrm{g\,cm^{-3}\,AU^2}$. The flux ratio $k = 4\pi\rho v_r / B_r$, defined in Eq. 1.19, is therefore nearly constant, changing sign between North and South, as shown in Fig. 6.6, with an absolute value around $\sim 1.5 \times 10^{-10} \mathrm{g^{1/2} cm^{-3/2}}$.

The temperature varies with distance following an approximate power law. A polytropic model will be assumed, with $T \propto \rho^{\gamma - 1}$. Plotting T vs. ρ (Fig. 6.7) gives an estimated $\gamma \sim 1.5$, which is below the adiabatic value of 5/3, but also above the isothermal value of 1. This is consistent with the Ulysses results presented by Feldman et al. (1998), where the polytropic γ was estimated to fit between 1.5 and 1.7. The difference from the adiabatic value is probably due to electron heat conduction.

The number density of α particles n_α is a fraction ~ 0.044 of the number density of protons n_p (Fig. 6.8). Therefore it can be assumed that $p = 1.8 \rho k_B T / \mathrm{amu} = (\gamma - 1) u$, taking into account both electron and ion pressure, and that (consistent with a one-fluid model) the electron and ion temperatures are the same.

The corotational angular velocity $\Omega = (v_\phi - B_\phi v_r / B_r)/R$ has a large dispersion (Fig. 6.9). However, its mean value of $\sim 2.1 \times 10^{-6} \mathrm{\,sec^{-1}}$ gives $2\pi/\Omega = 34$ days, agreeing well with the solar rotation period of ~ 36 days near the poles. This again agrees with the present view of the fast solar wind as originating mostly from the polar coronal region. In general terms, Ω tends to be dominated by its magnetic term, as shown in Fig. 6.10 —the small departures from unity in this plot are dominated by long term biases in the measurement of v_ϕ and are probably even smaller in reality than depicted here.

The mean and typical values mentioned here are used in the next section to construct a simple analytical model of the solar wind, which is used as a basis for simulations. They are useful as a reference for the mean field properties of the high-latitude heliosphere near solar minimum.

6.3 Simulations

6.3.1 Method

The simulations are performed using the methods and boundary condition presented in previous chapters of this thesis. Spherical coordinates (r, θ, ϕ) instead of cylindrical coordinates (z, R, ϕ) are used, replacing for instance the boundary condition at $z = 0$ with $r = r_{\mathrm{min}}$. The colatitude $\theta = 90° - \Theta$ coordinate is used in the calculations.

In order to set up the simulations, it is necessary to choose initial conditions, a value of r_{min}, and

define the functions $v_r(\theta)$, $\rho(\theta)$, $u_(\theta)$, $\Omega(\theta)$ and $B_r(\theta)$ at $r = r_{\rm min}$; these functions are taken equal to their initial values at $r = r_{\rm min}$. The initial conditions chosen are

$$
\begin{aligned}
v_r(r,\theta) &= v_{\rm rmin} + (v_{\rm ref} - v_{\rm rmin}) \min\left(\frac{r - r_{\rm min}}{r_{\rm ref} - r_{\rm min}}, 1\right) && (6.1)\\
B_r(r,\theta) &= \left(B_{\rm ref} r_{\rm ref}^2\right) r^{-2} && (6.2)\\
v_\theta(r,\theta) &= 0 && (6.3)\\
B_\theta(r,\theta) &= 0 && (6.4)\\
v_\phi(r,\theta) &= (1 - f_{B\phi})\, r\Omega_0 \sin\theta && (6.5)\\
B_\phi(r,\theta) &= -f_{B\phi} r\Omega_0 \frac{B_r}{v_r} \sin\theta && (6.6)\\
\rho(r,\theta) &= \left(\rho_{\rm ref} v_{\rm ref} r_{\rm ref}\right) r^{-2} v_r^{-1} && (6.7)\\
T(r,\theta) &= T_{\rm ref}\left(\frac{\rho}{\rho_{\rm ref}}\right)^{\gamma-1} && (6.8)\\
u(\rho,T) &= \frac{1.8\rho k_B T}{\mu(\gamma-1)}\,, && (6.9)
\end{aligned}
$$

using a reference radius $r_{\rm ref} = 1{\rm AU}$ where appropriate to obtain the initial values $v_{\rm ref}$, $B_{\rm ref}$, $\rho_{\rm ref}$, and $T_{\rm ref}$. A launching value $v_{\rm rmin}$ is used for the speed, a value Ω_0 for the corotational constant, and a number $0 < f_{B\phi} < 1$ gives the initial fraction of the magnetic term in this corotation. The particle mass constant μ is set to 1 amu and the factor 1.8 takes the presence of electrons and α particles approximately into account. The polytropic index γ has been set to 1.5.

Consistent with the restriction of the data to the high latitude case, the heliospheric current sheet present in the equatorial region was not simulated. In their suite of simulations, Keppens & Goedbloed (1999) present a split monopole for high latitudes and a dipole close to the equator, matching them smoothly. Here it was preferred to restrict the validity of the simulation to high latitudes. The simulations were however extended to the equator for geometrical convenience, in order to avoid forcing the fieldline at $\theta = \theta_{\rm max} < 90°$ to be radial. There is no doubt that the other approach has more generality. In particular, it allows to represent the equatorial region where the sign of the radial magnetic field changes inside the simulation.

The values of $r_{\rm min}$ and $v_{\rm rmin}$ have been chosen so as to have an initial value for the Bernoulli constant e which is approximately the same at $r_{\rm min}$ and at $r_{\rm ref}$. The terms considered in this approximation were the kinetic radial energy, the specific enthalpy, and the gravitational potential.

6.3.2 Results

6.3.2.1 Reference run

This simulation starts with the parameters $r_{\rm min} = 8R_\odot$, $\Omega_0 = 2\pi/34$ days, $B_{\rm ref} = 3.1 \times 10^{-5}$G, $\rho_{\rm ref} v_{\rm ref} r_{\rm ref}^2 = 9 \times 10^{10}$g sec^{-1}, $T_{\rm ref} = 2 \times 10^5$K, $v_{\rm ref} = 900{\rm km\,s^{-1}}$, $v_{\rm rmin} = 418.6{\rm km\,s^{-1}}$, and $f_{B\phi} = 0.7$.

With these values, the magnetic field is essentially passive, which corresponds to the mean values of Ulysses data.

The numerical box extends from $\theta_{\min} = 0°$ to $\theta_{\max} = 90°$, using 90 equally spaced zones, and from $r_{\min} = 8R_\odot$ to $r_{\max} = 1.5\text{AU}$, using 90 zones, equally-spaced with a spacing of 10^{-3}AU for the first 10 zones, and ratioed[1] for the remaining 80.

After steady state is achieved, the resulting flow is mostly radial, with a final speed at $r = r_{\max}$ of $v_r \sim 890\text{km}\,\text{s}^{-1}$. Corotation is properly enforced with the magnetic term becoming dominant at large distances. Fig. 6.11 shows how $v_\phi / R\Omega$ rapidly drops with a power law of r^{-2} from a starting value of ~ 0.5 at $r_{\min}$. However, the angular momentum l has an appreciable fluid contribution, between 0.20 and 0.26, with little radial or angular dependence. Acceleration of the flow can be seen in Figs. 6.12 and Figs. 6.13; they show how the flow, starting barely supersonic, crosses the Alfvén surface and reaches its final speed.

The Alfvén radius is $r_A = 11.5R_\odot$, with little θ dependence. Mestel's theorem $\left(l = R_A^2\Omega = r_A^2\Omega\sin^2\theta\right)$ predicts the angular momentum correctly.

This simulation was also tested with a run starting with $f_{B\phi} = 0.0$ instead of 0.7, with substantially the same results in steady state. This shows that the final value of the toroidal magnetic field is independent of initial conditions.

6.3.2.2 Simulations of faster rotators

The Sun is a star in relatively slow rotation, but with plasma $\beta \ll 1$ at its surface. It is interesting to study the effects that an equivalent star that happens to rotate faster would produce in its outflowing wind. The two simulations presented here are similar to that in 6.3.2.1, differing only in having faster values for Ω_0, corresponding to a rotation period of 1 day and 3 days respectively.

The simulation with a period of 3 days produces essentially the same final speed v_r (Fig. 6.14). Some collimation is visible in the angular dependence of the Alfvén radius (Fig. 6.15), and more clearly in the ratio between the values of θ_r at some large radius r and at the footpoint $r = r_{\min}$ (connected by the same fieldline). This ratio is visibly smaller than 1.0, especially close to the axis (Fig. 6.16).[2] This factor makes the fieldlines not exactly radial, but not enough to be very important.

The simulation with a period of 1 day has marked departures from spherical symmetry. For instance, the final speed at $r = 1.5\text{AU}$ now has a strong angular dependence (Fig. 6.17); the speed is approximately the same as before at the poles but increases towards lower latitudes. Collimation is clearly visible in the position of the Alfvén radius (Fig. 6.18), in the ratio between θ_r and θ_F on the same fieldline (Fig. 6.19), and in the shape of the fieldlines (Fig. 6.20).

[1] Each zone is wider than the previous one by a small constant factor.

[2] A similar simulation, using $\theta_{\max} = 60°$, featured a ratio $\theta_{r_{\max}}/\theta_F = 1$ at $\theta = 60°$, instead of 90°; evidently the degree of collimation was altered by the shape of the computational box.

6.4 Energy and angular momentum flux

It is important to estimate how much energy and angular momentum the Sun currently loses in the solar wind. Those values can be estimated from the Bernoulli constant e defined in Eq. 1.22 and the angular momentum constant l defined in Eq. 1.21 by multiplying these constants by the mass loss rate $\rho v_r r^2$ and integrating over solid angle $d\omega$. In stationary, axisymmetric theory, these values are functions of fieldline only, and furthermore $l = {R_A}^2\Omega$, where $R_A = r_A \sin\theta$ is the cylindrical Alfvén radius. The simulations shown in §6.3.2 agree with theoretical expectations, giving a power $L = \int e\rho v_r r^2\, d\omega = 4.5{\times}10^{27}\mathrm{erg/\,sec}$ and a torque $G = \int l\rho v_r r^2\, d\omega = 1.0{\times}10^{30}\mathrm{dyn\,cm/\,sec}$. [3] The relatively small value obtained for G is due to the small value of the Alfvén radius used in this simulation, consistent with the high values of v_r measured by Ulysses at high latitudes.

It is now time for theory to confront measurement of the fast, "quiet" wind at solar minimum. Assuming a value for the polytropic index γ, the enthalpy per unit mass h can be estimated as $h = \gamma u/\rho$ where u is the internal energy per unit volume, related to the temperature by $u = (\gamma-1)^{-1}1.8\rho k_B T/\mathrm{amu}$. With this in hand, it is possible to calculate the Bernoulli constant. The results (Fig. 6.21) show that the radial kinetic energy term dominates the value of e, with the enthalpy two orders of magnitude smaller and the other terms contributing to e still another order of magnitude lower (Figs. 6.22, 6.23, 6.24, 6.25, and 6.26). The radial kinetic energy (largely independent of latitude, outside of the equatorial region) gives an estimate of the power in the wind as $L = 4\pi\frac{v_r^2}{2}\rho v_r r^2 \sim 3{\times}10^{27}\mathrm{erg/\,sec}$, six orders of magnitude below the solar luminosity.

Assuming axisymmetric, steady state theory, the value of the angular momentum can be estimated from $l = {R_A}^2\Omega$. While strictly speaking Ulysses measurements do not reach the Alfvén radius where $v_r = B_r/\sqrt{4\pi\rho}$, they provide an estimation. Assuming that v_r grows by a factor α between the Alfvén radius and the measured region, and assuming that the flow is mostly radial, we have that $r_A{\sim}r(B_r/\sqrt{4\pi\rho}){v_r}^{-1}\alpha^{1/2}{\sim}11R_\odot\alpha^{1/2}$. With this estimated radius, and remembering that the magnetic term was observed to be dominant in Ω at Ulysses distances, the result is $l{\sim}-RB_\phi k^{-1}\alpha$. The growth ratio α, is between 1.1 and 1.5 (Suess et al. 1998); the simulation indicates $\alpha{\sim}1.3$. Therefore we expect that the magnetic term in $l = R(v_\phi - B_\phi/k)$, equal to $l_M = -RB_\phi/k$, is at least important as the fluid term $l_F = Rv_\phi$ and probably dominant, with a ratio $l_F/l_M{\sim}\alpha - 1{\sim}0.3$. This gives a value for v_ϕ of approximately $0.2\,\mathrm{km\,s^{-1}}{r_{\mathrm{AU}}}^{-1}\sin\theta$, much smaller than the typical values of the solar wind velocity. Extremely high precision would be needed to measure this small velocity component, which also would be masked by non-axisymmetric azimuthal motions in the order of $10\mathrm{km\,s^{-1}}$.

To make the angular momentum measurement and calculation even more complex, there are large systematic errors present in the Ulysses angular data (Goldstein & McComas 1999). Fig. 6.27

[3] These integrals have been integrated over a solid angle of 4π, despite the fact that the simulation extends over a limited angle.

was obtained using the data presented at NSSDC uncritically. Its panels show a specific angular momentum which is not a function of latitude alone; given that the fieldlines are largely radial, this would mean that, despite axisymmetric theory, the quantity l is not being conserved along fieldlines. Fig. 6.28 shows that this unexpected l is dominated by its fluid term, $l{\sim}Rv_\phi$, whose sign changes between hemispheres and when the orbit reaches $r{\sim}3.5$AU. The magnetic term $l_M = -RB_\phi/k$, instead of being the larger term in the directly measured value $l = R\left(v_\phi - B_\phi/k\right)$, is typically two orders of magnitude smaller and it does not agree regularly in sign. The real situation is probably very different: Ulysses measurements of v_ϕ and v_θ have large systematic errors, especially large when dealing with long trends. These errors are so large as to preclude any direct measurement of l (Goldstein 1999). The dispersion of v_ϕ observed in the data is however mostly physical, due to deflections in the wind originated in turbulence and Alfvén waves. It is possible to assume that the dispersive part of Ulysses measurement of the azimuthal velocity ($\Delta v_\phi{\sim}20\mathrm{km\,s^{-1}}$) is a valid estimation despite the many sources of error mentioned in Goldstein & McComas (1999), because these errors affect the long trends more than the fast variations. This "random" variation Δv_ϕ is probably the largest part of the authentic instantaneous value of l, causing effects larger than the theoretical Mestel value of $R_A^2\Omega$ by around three orders of magnitude. This theoretical value might still be the average momentum loss, if the rapidly varying part of v_ϕ nearly cancels out. The measurement of the angle $\arctan(v_\phi/v_r)$, necessary to estimate v_ϕ and l, might be more reliable using long term averages, or taking measurements closer to the Alfvén surface.

The magnetic term is dominant in $\Omega = \left(v_\phi - B_\phi v_r/B_r\right)/R$, giving the expected Parker spiral. However, $l = R\left(v_\phi - B_\phi B_r/4\pi\rho v_r\right)$ may be dominated by the the rapidly varying, noisy v_ϕ term. This combination of inequalities is possible when

$$\frac{|B_\phi B_r|}{4\pi\rho v_r} < |v_\phi| \ll \frac{|B_\phi| v_r}{|B_r|} \tag{6.10}$$

$$\Rightarrow \quad \frac{B_r^2}{4\pi\rho} \ll v_r^2\,, \tag{6.11}$$

that is, in strongly super-Alfvénic flows, as is indeed the case for the Sun where Ω is dominated by the magnetic term at large r, but l has a sizable v_ϕ term (about 25% of the total in the simulations). This value is consistent with allowing some moderate growth factor α for v_r, around 30% after the Alfvén point.

The measured k and e are close to values computed from axisymmetric theory, and Ω is not far away. However, l, dominated observationally by its rapidly varying v_ϕ term, is far from theoretical values.

The departures from theory can be explained by assuming the presence of Alfvén waves superposed on the radial field, breaking both steady state and axisymmetry. If there are large scale departures of the fields, those waves must have a large scale and large time correlation, as suggested

by Forsyth et al. (1996) to explain some departures of Ω from the ideal Parker spiral value. (The large scale trends for l shown in the figures are however explained as instrumental error, rather than requiring a physical explanation.)

A recipe of the solar wind can be formulated by adding three ingredients. The first ingredient is the ideal Parker model, where there is no v_ϕ, no v_θ, no B_θ, a large $B_r \propto r^{-2}$, a large $v_r \propto r^0$, and a moderate B_ϕ which starts modest at small r, with a ratio B_ϕ/B_r increasing with distance. The next addition to the recipe is a small v_ϕ, consistent with Mestel's theorem $l = R_A^2\Omega$, using a value of r_A close to $11R_\odot$. This v_ϕ is rather small, less than $1\mathrm{km\,s^{-1}}$, and it decreases $|B_\phi|$ by some small factor to keep corotation. Finally, the key ingredient consists in Alfvén waves outgoing from the Sun. Those waves modify the non-radial components of the vectors. The already sizable value of B_ϕ is slightly perturbed by these waves; but the values of the other non-radial vector components, which were zero or very small before considering these waves, become completely determined by these waves. This would explain why

1. The flux ratio $k_r = 4\pi\rho v_r/B_r$ and the corotational $\Omega = (v_\phi - B_\phi v_r/B_r)/R \sim -B_\phi v_r/B_r/R$ behave as expected: they depend on quantities mostly unaffected by the waves.

2. The flux ratio $k_\theta = 4\pi\rho v_\theta/B_\theta$ depends on quantities defined exclusively by the waves, and becomes very different from k_r.

3. The angular momentum $l = R(v_\phi - B_\phi/k_r)$ is far off from predictions; its most important term is dominated by wave effects.

In favor of this Alfvén wave theory, it is the fact that v_θ, while typically smaller than v_ϕ, is not usually much smaller. Also the approximate relation

$$\delta\mathbf{v} \sim \frac{\delta\mathbf{B}}{\sqrt{4\pi\rho}}\,, \tag{6.12}$$

frequently fulfilled by the flow perturbations (Bruno et al. 1985) points out to Alfvén waves.

6.5 Conclusions

Ulysses high latitude data taken during a solar minimum were studied and used as the basis for an MHD simulation. Their analysis showed that:

- The energy flux was much smaller than the solar luminosity (six orders of magnitude below). However, the large dispersions of v_ϕ due to waves and turbulence and the large systematic errors in the data (Goldstein & McComas 1999,Goldstein 1999) make a direct measurement of the angular momentum flux impossible.

- The dispersions of the transverse speeds are close to the dispersion of the transverse magnetic fields divided by $\sqrt{4\pi\rho}$ (Bruno et al. 1985). This suggests an Alfvénic wave component in the non-axisymmetric part of the flow.

- A polytropic fit with $\gamma = 1.5$ (Fig. 6.7) was found to the high-latitude data on temperature and density data. This result is consistent with the value found by Feldman et al. (1998), using a slightly different selection of data. This value is both too high and too low. It is too low because, being below $\gamma = 5/3$, it shows that either thermal conductivity or heating are present, while it is too high because extrapolating the polytropic fit from 1.5AU towards the Sun with this value of γ would give an unreasonably high value for the temperature of the solar corona. Clearly the phenomenological polytropic index decreases with radius, showing that the thermal conduction or heating mechanisms are more efficient closer to the Sun. The value $\gamma = 1.5$ is also marginally high in that it implies $T \propto r^{-1}$: any power law steeper than this would have allowed (in principle) subsonic solutions to the Parker equations (Parker 1965). It was decided however to use this value $\gamma = 1.5$ as close to the Sun as possible, to have an estimation consistently based on high-latitude data of the solar wind. The closest approach to the Sun in the simulation was at the sonic point of the solar wind, estimated here to be at $8R_\odot$, based on energy and mass conservation for this value of γ.

- The measured ratio of alpha particles to protons produced an estimate of $1.8\rho k_B T/\mu$ for the pressure, under the assumption that the temperatures of protons, alpha particles, and electrons are the same.

- The Parker spiral structure of the solar wind toroidal field behaved as expected, giving a value of Ω consistent with the period of solar rotation of 34 days. The measured values of Ω in the wind have a large dispersion, but they seem to be closer to the value given by polar rather than equatorial rotation of the Sun. This is consistent with the picture of the solar wind as originating from the polar coronal holes.

- Some other results of Ulysses are shown: the split-monopole shape of B_r at high latitude the lack of latitude dependence of the high-latitude fast flow v_r. The radial velocity term is dominant in the Bernoulli constant e and in the mass flux ρv_r, implying that these quantities are also mostly latitude-independent inside the high-latitude portions of the flow, outside of the equatorial heliospheric current sheet.

The simulation performed here gave the estimation of some quantities difficult to measure directly or estimate from the data, for instance, the value of the ratio Rv_ϕ/l (giving the relative importance of the fluid part of the angular momentum) and the ratio between the Alfvén speed v_A and the speed at infinity v_∞ (giving the precise location of the Alfvén surface). The value of Rv_ϕ/l is particularly

important for the solar case because a direct measurement of the mean values of v_ϕ and l from Ulysses data is impossible. The simulation gives an estimate based on theory of a quantity that otherwise cannot be measured.

Stars rotating 10 and 30 times faster than the Sun were also studied for comparison: they may represent the rotation of the Sun at some earlier stage of its evolution. They showed appreciable magnetocentrifugal acceleration (mostly in the equatorial direction), together with collimation in the polar direction. Compared with launching from an accretion disk, there are many basic differences:

- The accretion disk is close to Keplerian rotation, that is, close to breakup speed. Stars can rotate at any speed between zero and breakup, with the last being the least probable, except for very young stars.
- The wind emitted from a Keplerian disk is probably dynamically cold for most of its trajectory, while the wind emitted by a star has a thermal pressure that may dominate the flow.
- The equatorial mass discharge of the solar wind is lower than that from the poles by a factor of around 2.0. The magnetic field is constant over most latitudes. In the case of a Keplerian disk, the analog of the equator is the outer radius, and the analog of the pole is the inner radius; both the magnetic field and the mass discharge are expected to have strong dependences (power laws) on the distance from the central object.
- The geometry of the emitting surface is spherical instead of largely flat.

Despite these many differences, the collimating mechanism appeared in a similar way. The Alfvén surface of the faster rotator became non-spherical, further away from the Sun at the poles than at the equator by a factor of 10%. The Alfvén radius has a value equivalent to that of the slow rotator at an intermediate latitude. This predicts essentially the same value for the ratio $\frac{\text{torque}}{\text{angular speed}}$ as for the slower rotator. This is probably due to the relatively large value of v_r at $r = r_{\text{min}}$ and to the large thermal pressure. Both effects are spherically symmetric and independent of the rotation, and largely determine the shape of the Alfvén surface, for a given value of the hemispherically symmetric magnetic field B_r, in spite of the larger rotation.

All these data were taken during solar minimum. Ulysses is already starting to measure the polar wind at solar maximum. It will achieve its highest southern latitude $\Theta = -80.2°$, $r = 2.30$AU on 24/Nov/2000 and its highest northern latitude $\Theta = +80.2°$, $r = 2.02$AU on 12/Oct/2001. The conditions of the polar wind are expected to be very different from those found in the previous polar pass. In particular, the transient events are expected to be much stronger, disturbing the structure of the wind. The Ulysses mission is in an unique position to study the 3D evolution of the heliosphere across the entire solar cycle, far from the ecliptic.

Fig. 6.1 *Ulysses orbit. All latitudes included, data averaged in 1-hour periods.*

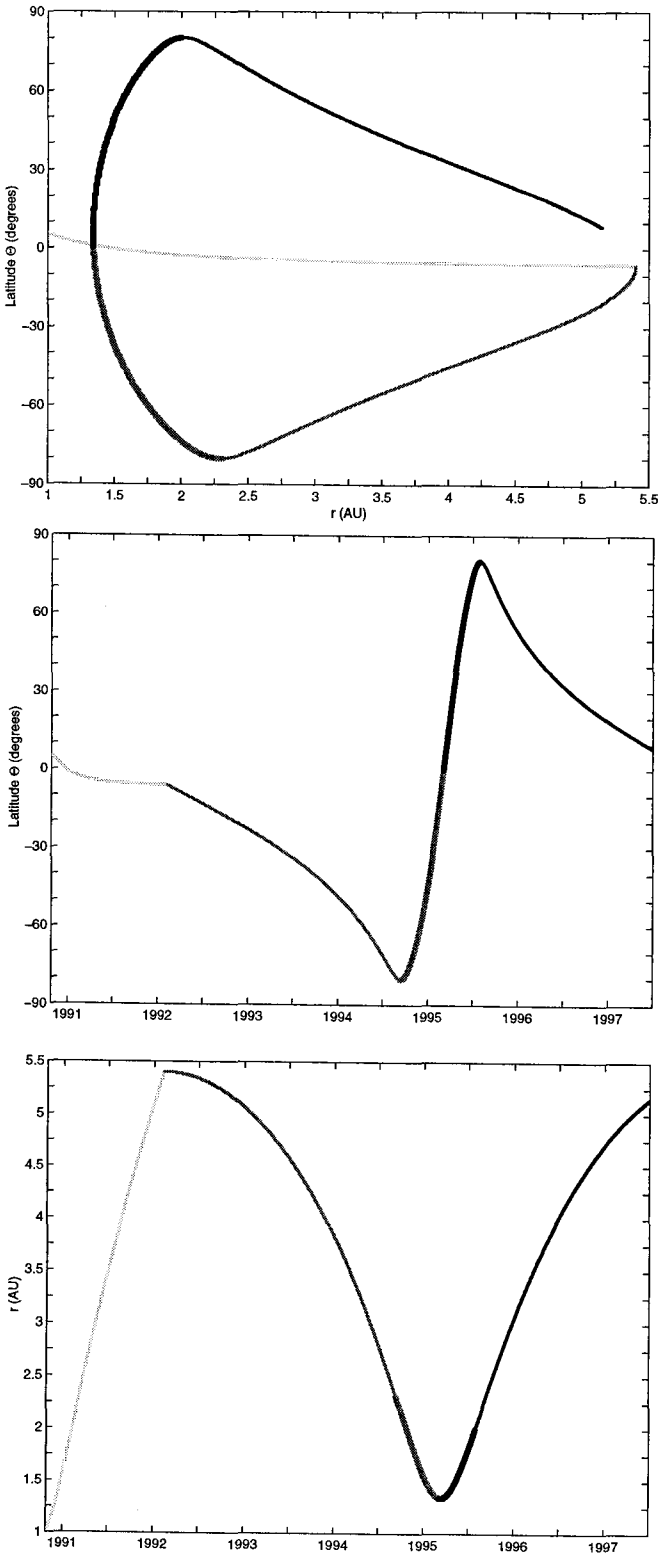

Fig. 6.2 *Magnetic flux per solid angle $B_r r^2 sign(\Theta)$, from Ulysses data. Calculated ordinate axis.*

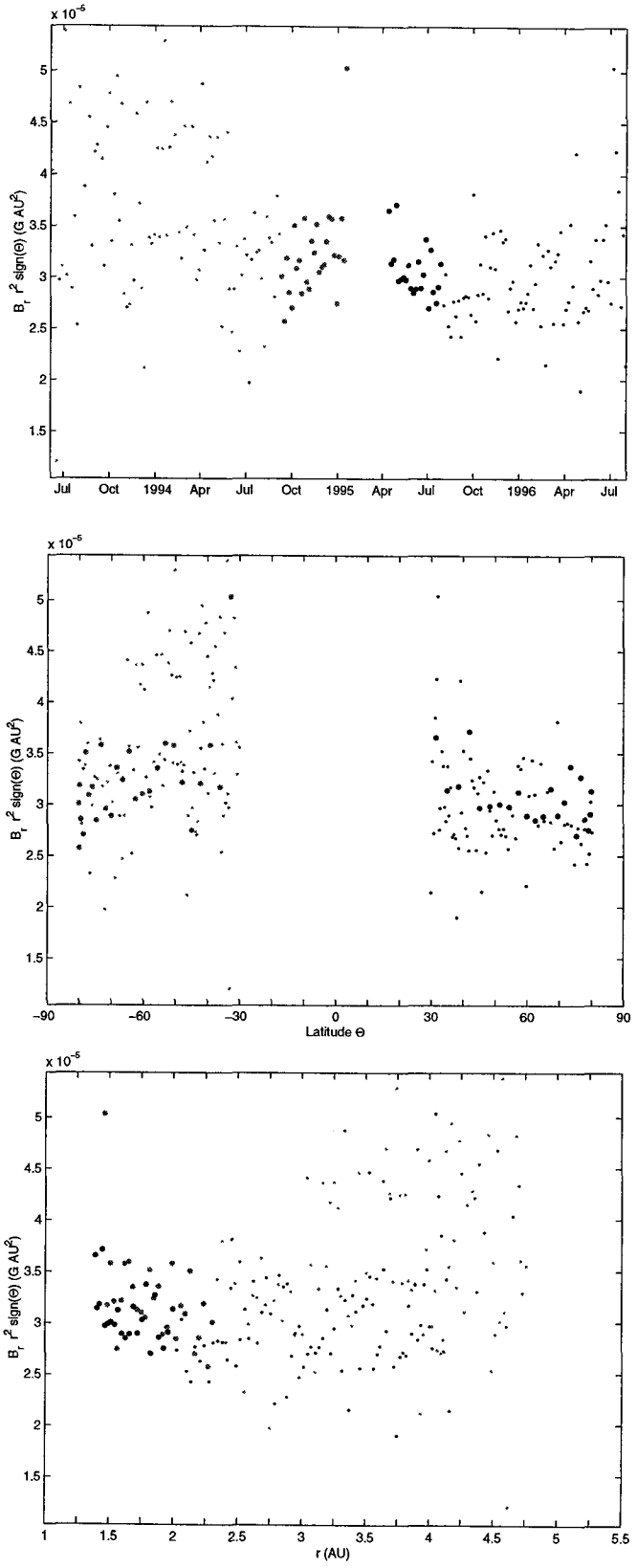

Fig. 6.3 *Radial velocity v_r, until just before the completion of the first Ulysses orbit. Data averaged over 48-hour periods.*

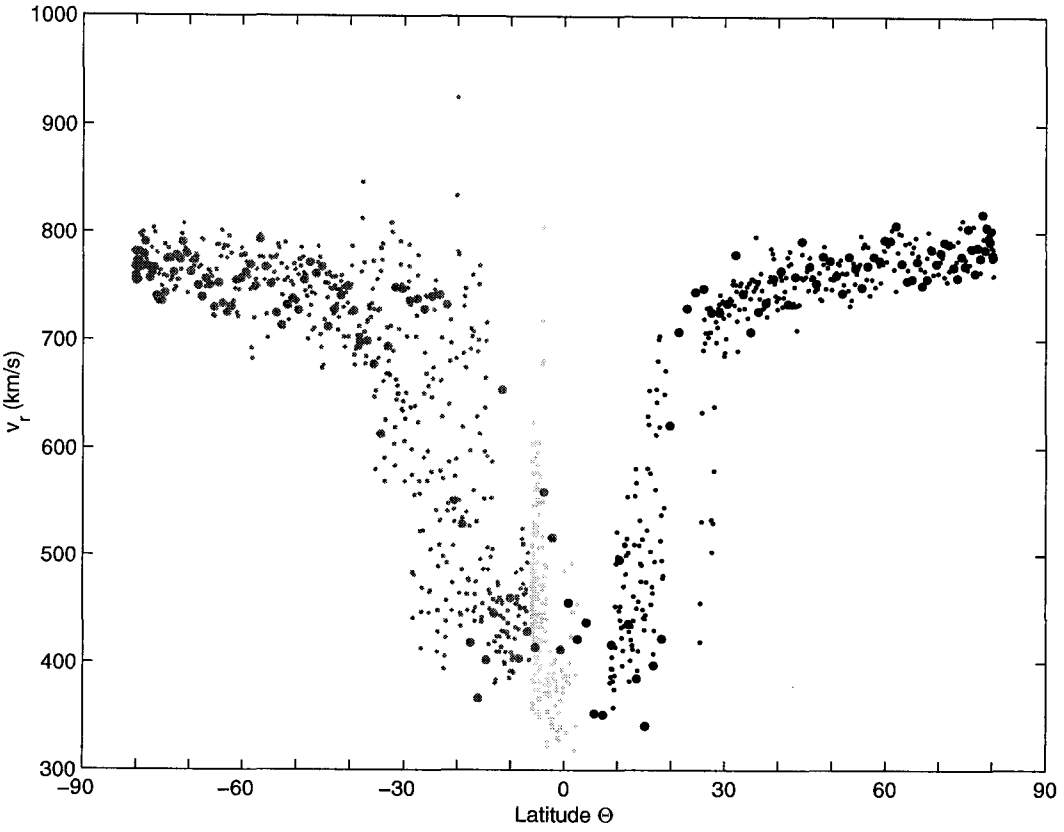

Fig. 6.4 *Radial velocity v_r. High latitude Ulysses data, averaged over 48-hour periods.*

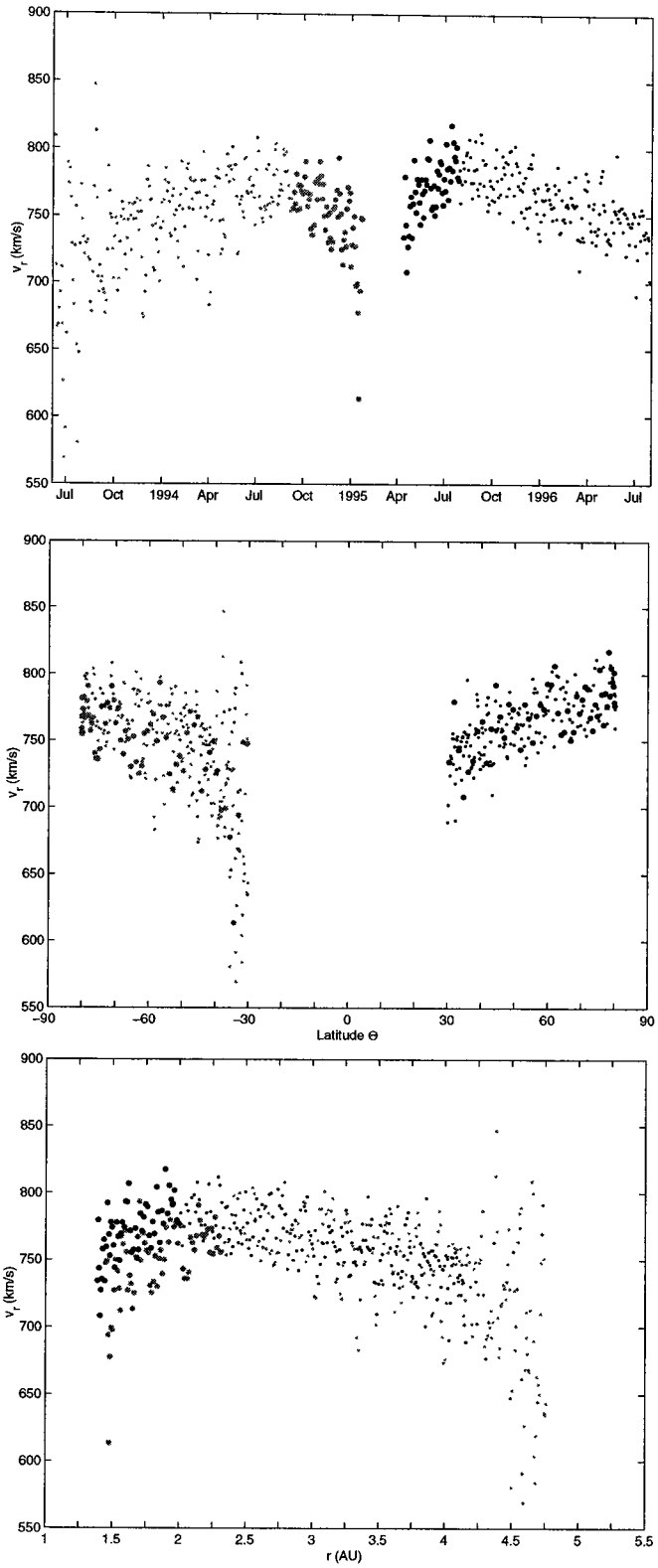

Fig. 6.5 *Mass loss rate per solid angle, $\rho v_r r^2$, from Ulysses data. Calculated ordinate axis.*

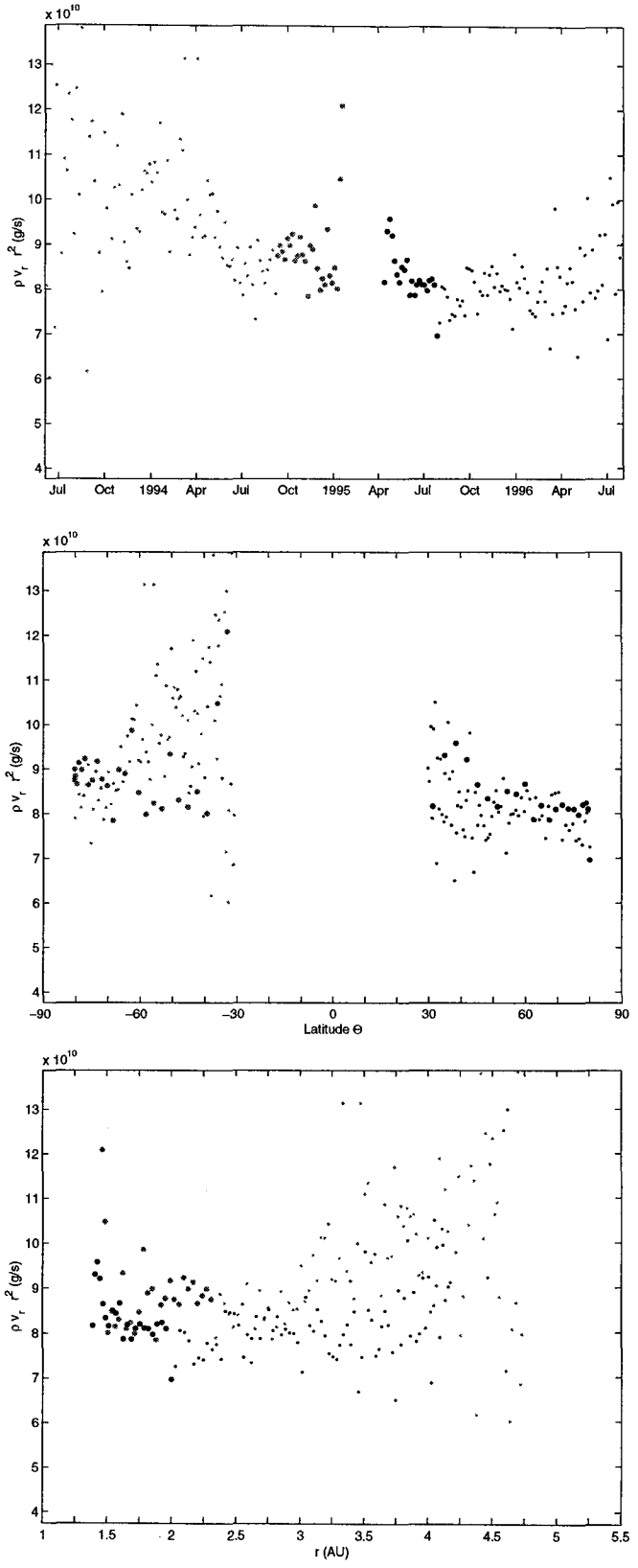

Fig. 6.6 *Flux ratio* $k = 4\pi\rho v_r / B_r sign(\Theta)$, *from Ulysses data. Calculated ordinate axis.*

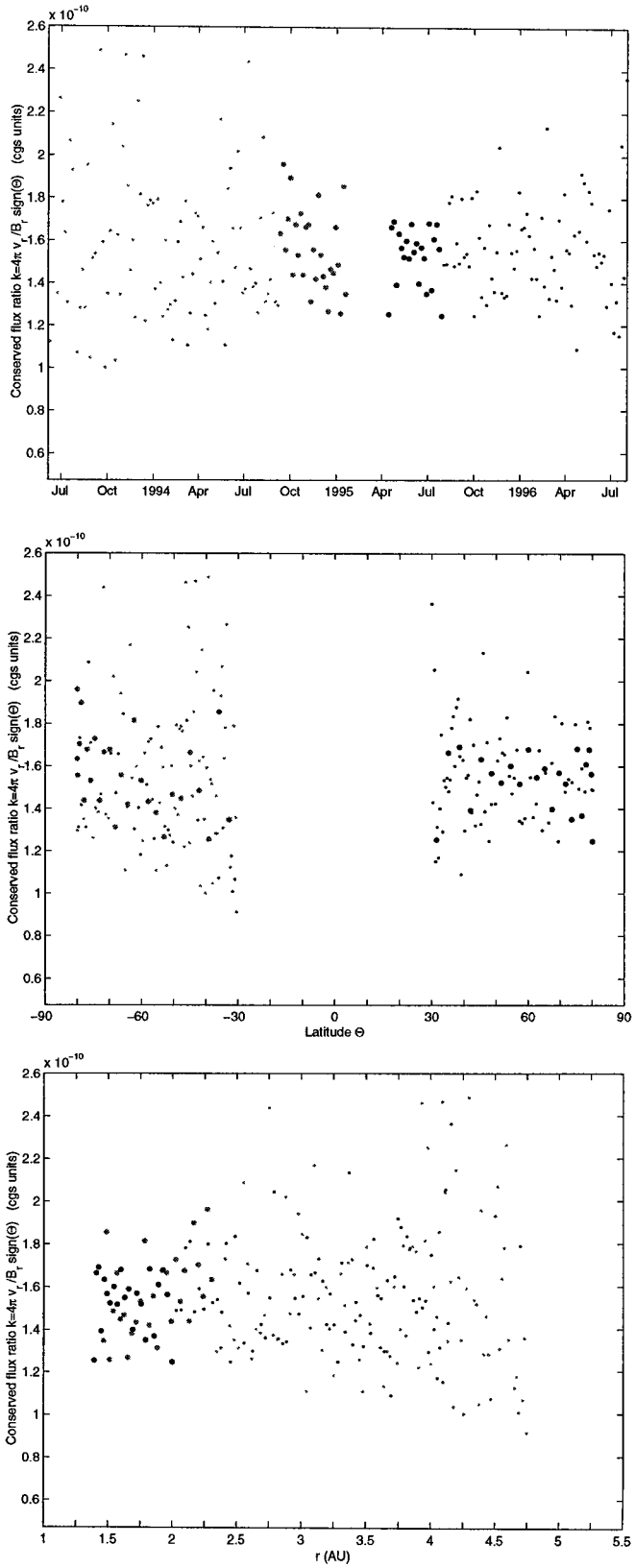

Fig. 6.7 *Temperature as a function of plasma density, from Ulysses data. An indicative line showing a* $T \propto \rho^{0.5}$ *relation is drawn over the data, consistent with* $\gamma = 1.5$.

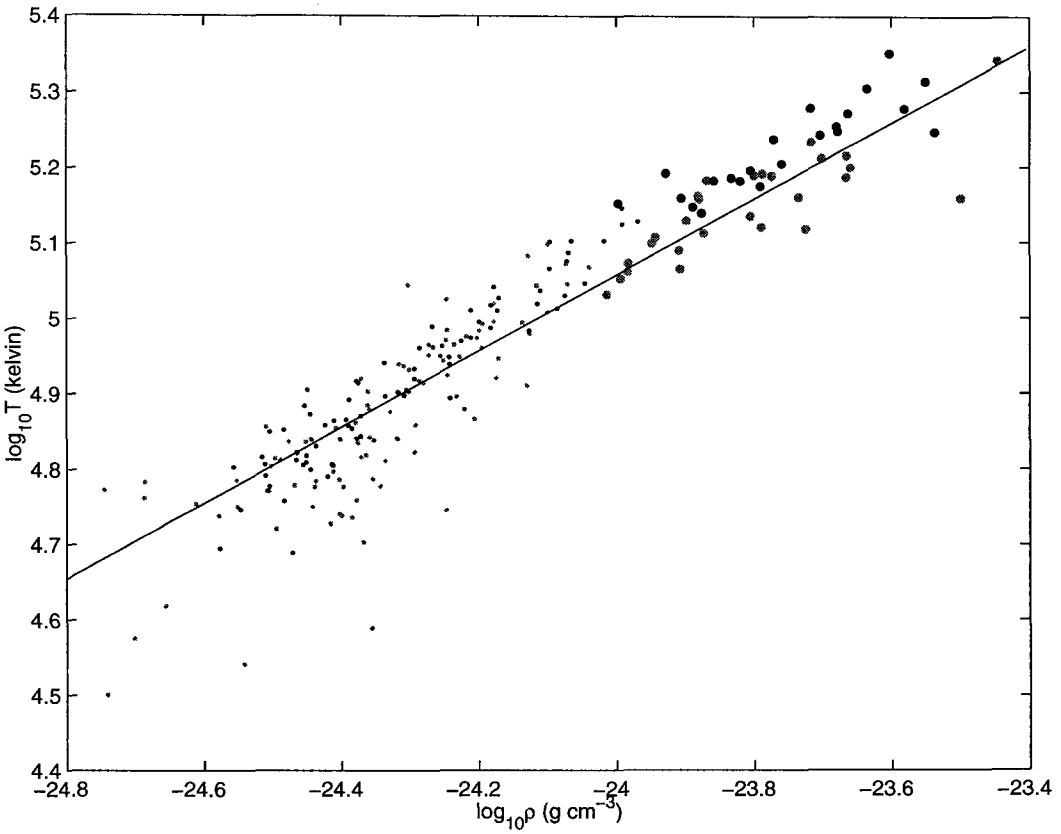

Fig. 6.8 *Ratio of the number of α particles to protons, from Ulysses data. Calculated ordinate axis.*

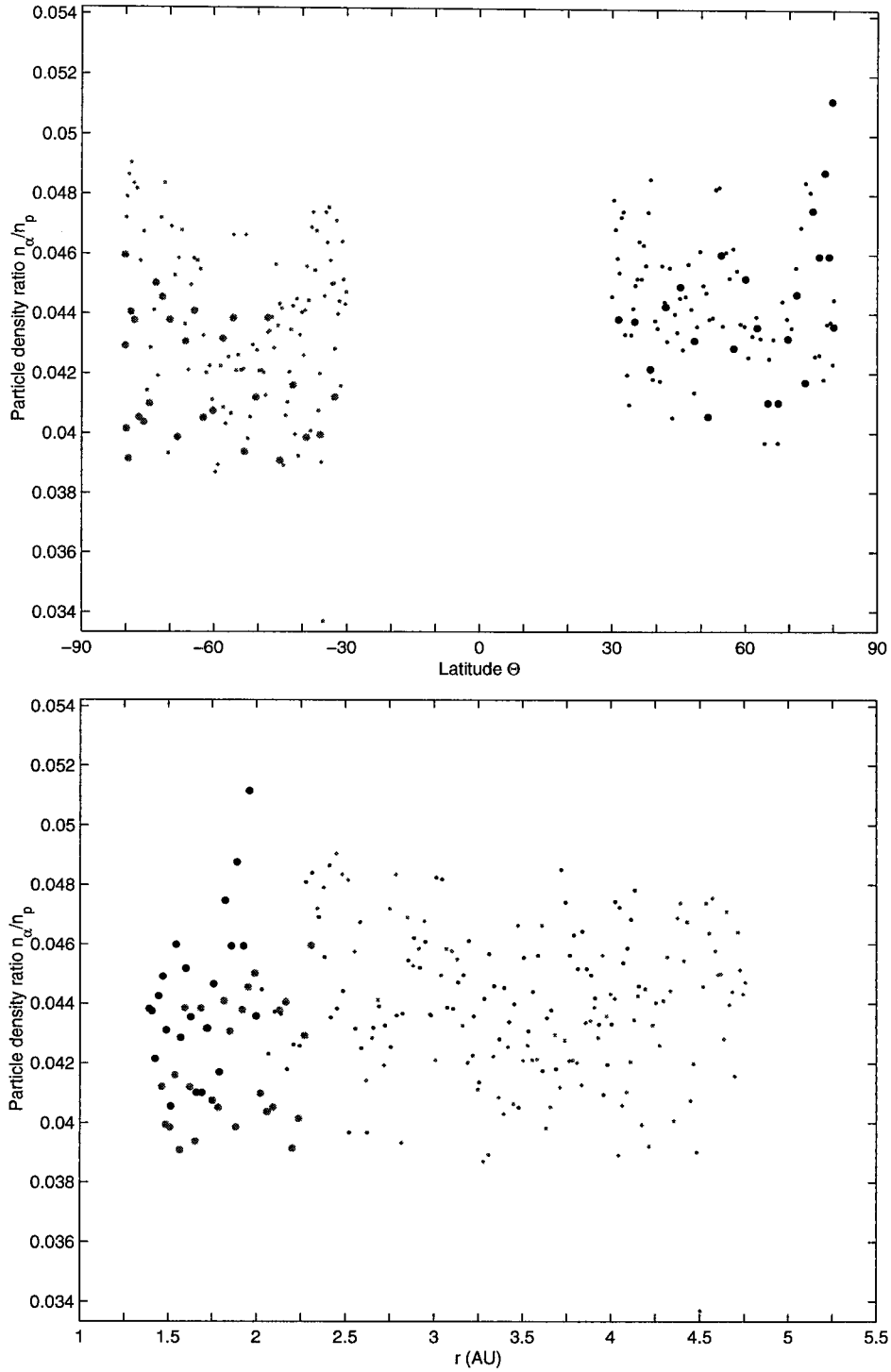

Fig. 6.9 *Corotational* $\Omega = R^{-1}(v_\phi - B_\phi v_r / B_r)$, *from Ulysses data. Calculated ordinate axis.*

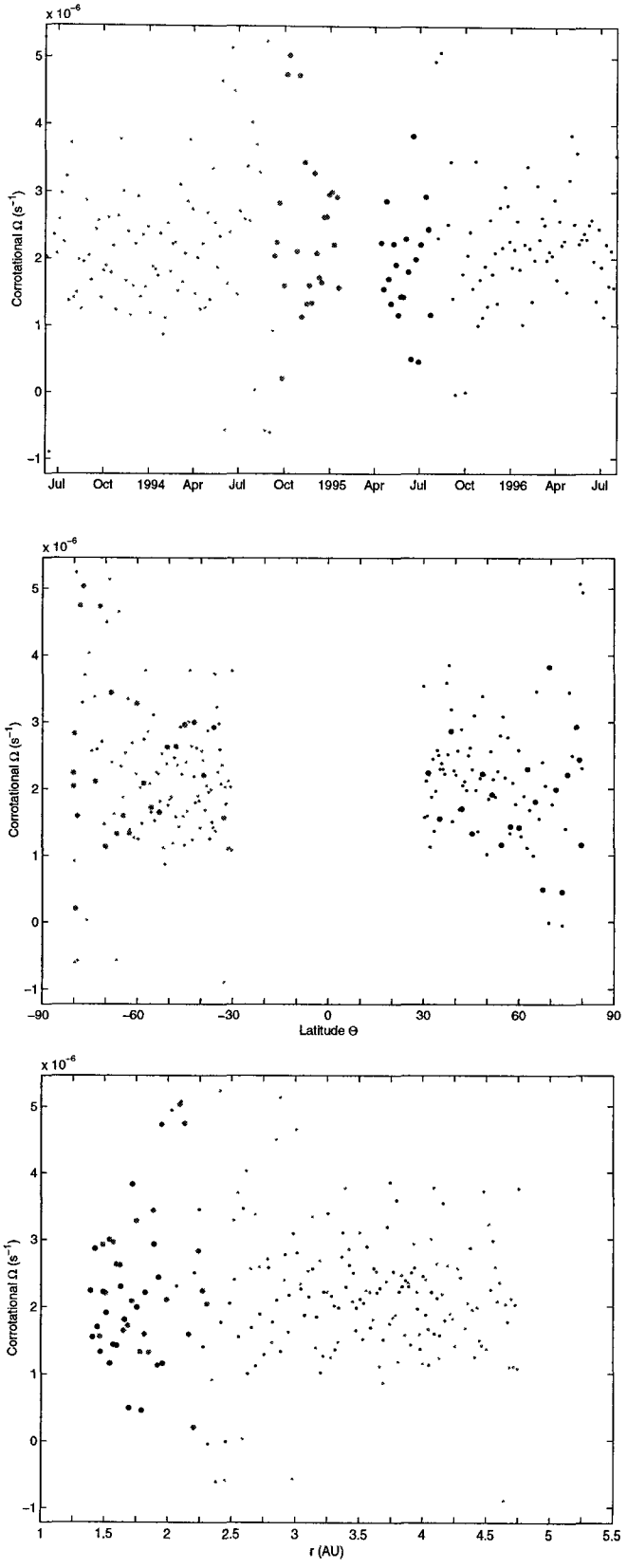

Fig. 6.10 *Ratio of the magnetic term $-B_\phi v_r / RB_r$ of the corotational Ω to Ω itself, from Ulysses data. Calculated ordinate axis.*

Note that the small departures of this ratio from unity are largely due to long term biases in Ulysses measurements of v_ϕ.

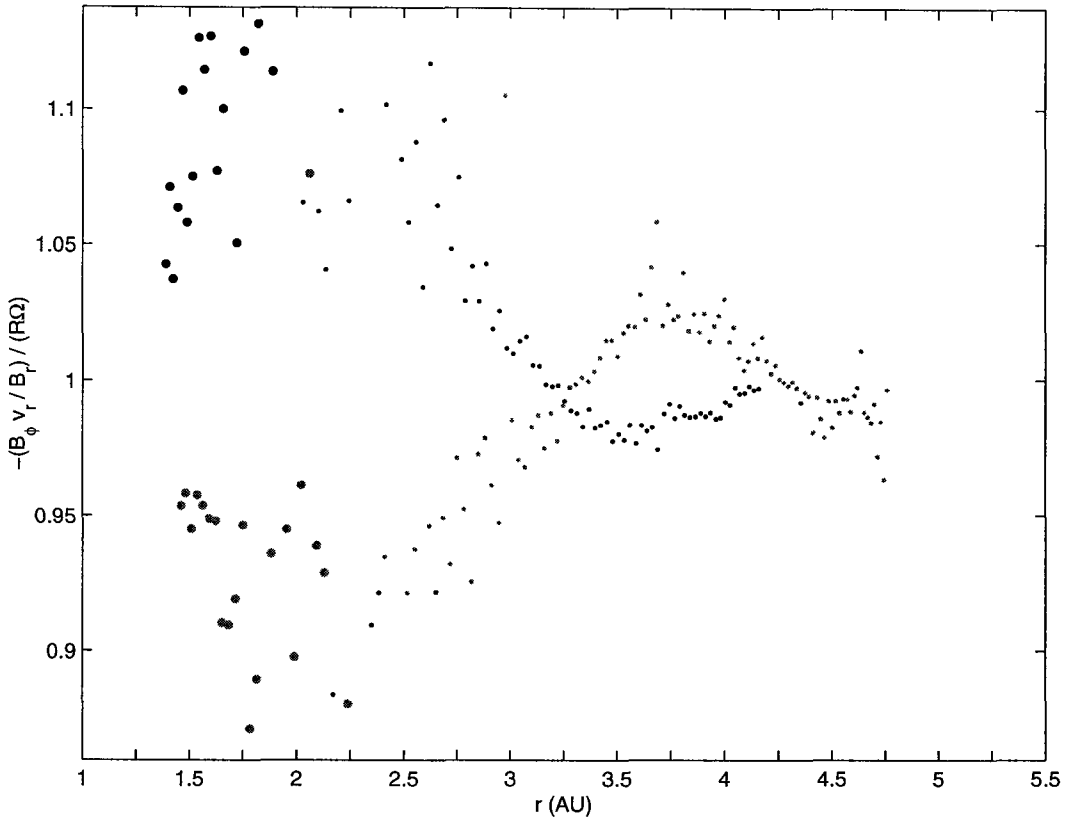

Fig. 6.11 *Solar wind reference simulation. Values of v_ϕ relative to the corotational angular speed and to the specific angular momentum, taken at $\theta = 30.5°$. Values taken at a different angle would not differ appreciably.*

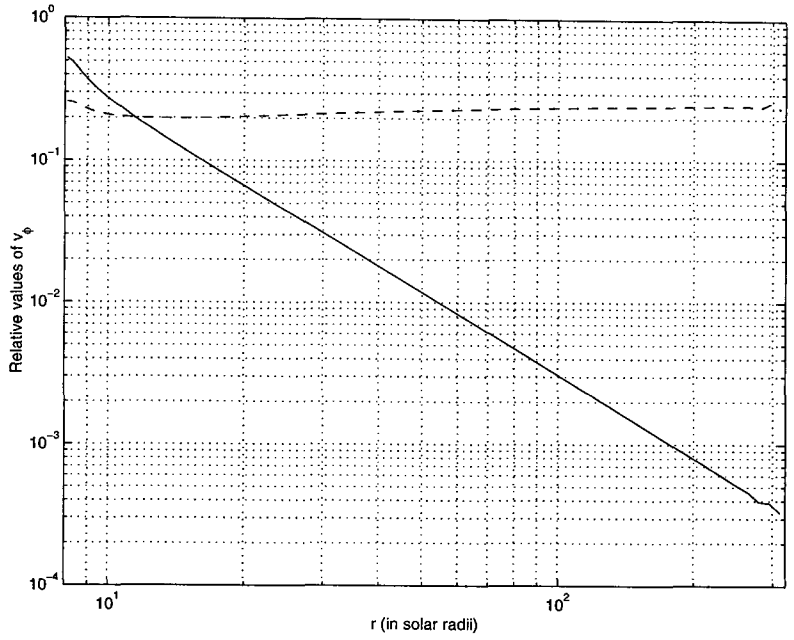

Fig. 6.12 *Solar wind reference simulation. Values of v_r along the radial line $\theta = 30.5°$. Values taken at a different angle would not differ appreciably.*

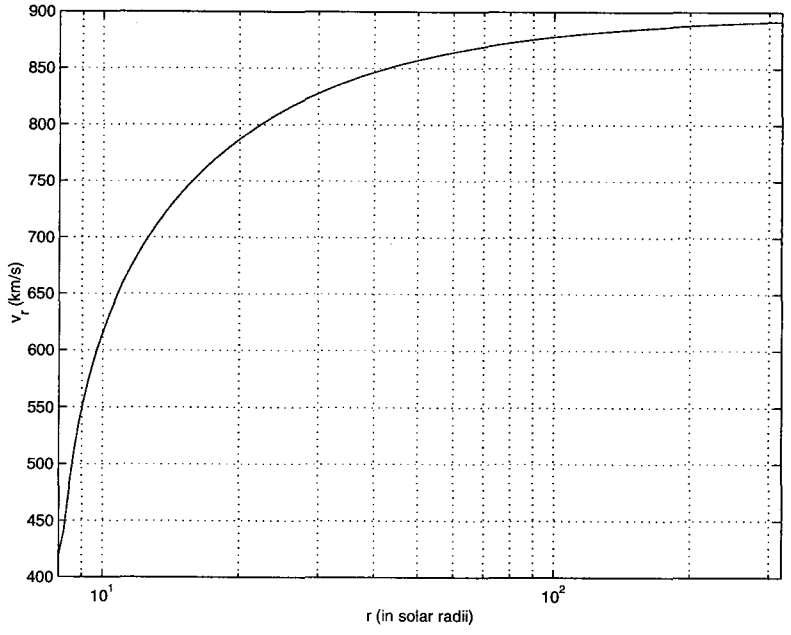

Fig. 6.13 *Solar wind reference simulation. Values of the sonic, Alfvénic and fast magnetosonic Mach numbers on the radial line* $\theta = 30.5°$. *Values taken at a different angle would not differ appreciably.*

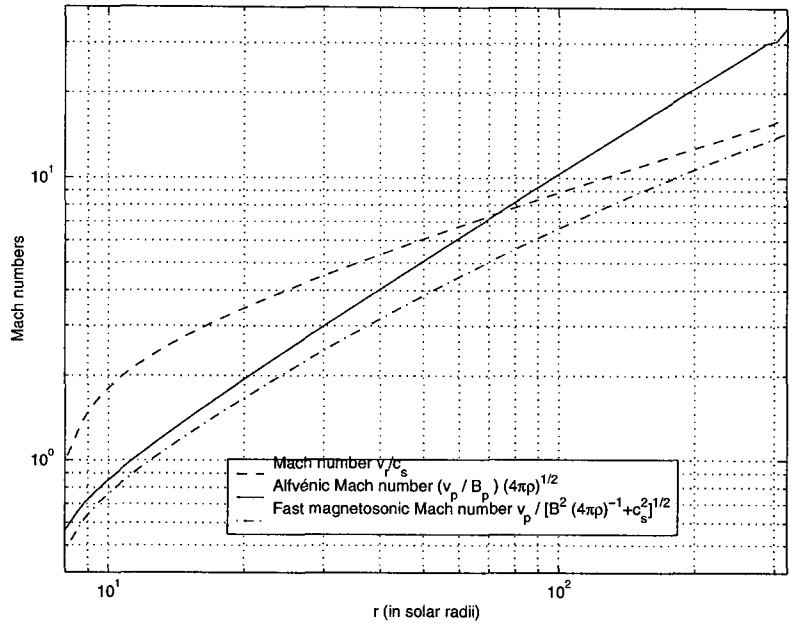

Fig. 6.14 *Solar wind simulation with a 3-day rotation period.*
Values of v_r *at six different heights, as a function of colatitude* θ.

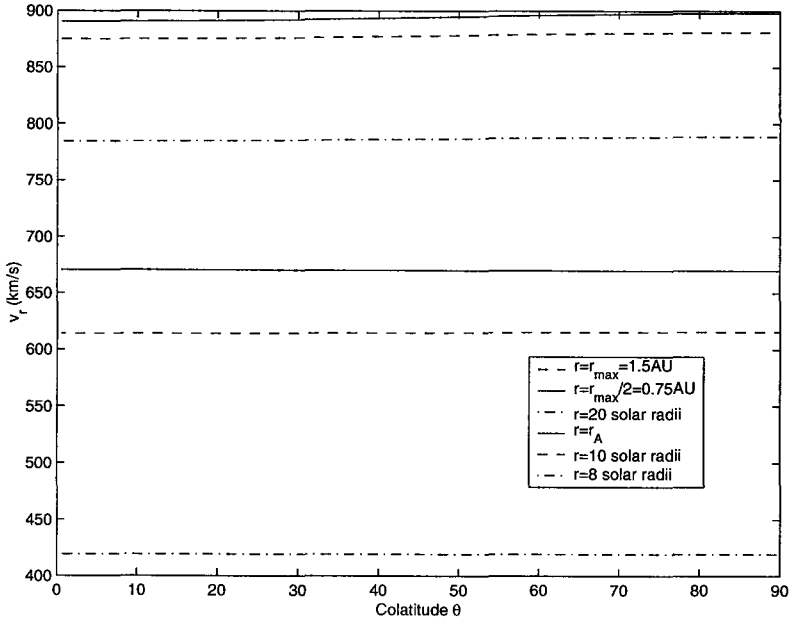

Fig. 6.15 *Solar wind simulation with a 3-day rotation period.*

Critical radii as a function of colatitude θ.

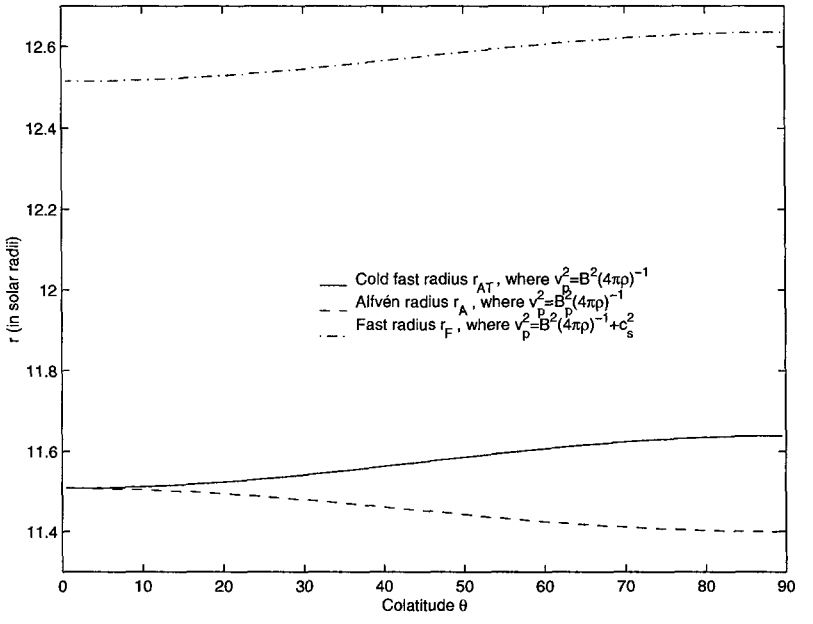

Fig. 6.16 *Solar wind simulation with a 3-day rotation period.*

Ratio between the angle θ_r at a certain radius r and its value θ_F at the footpoint $r = r_{\min}$, taken on the same poloidal fieldline. Two values of r are shown. θ.

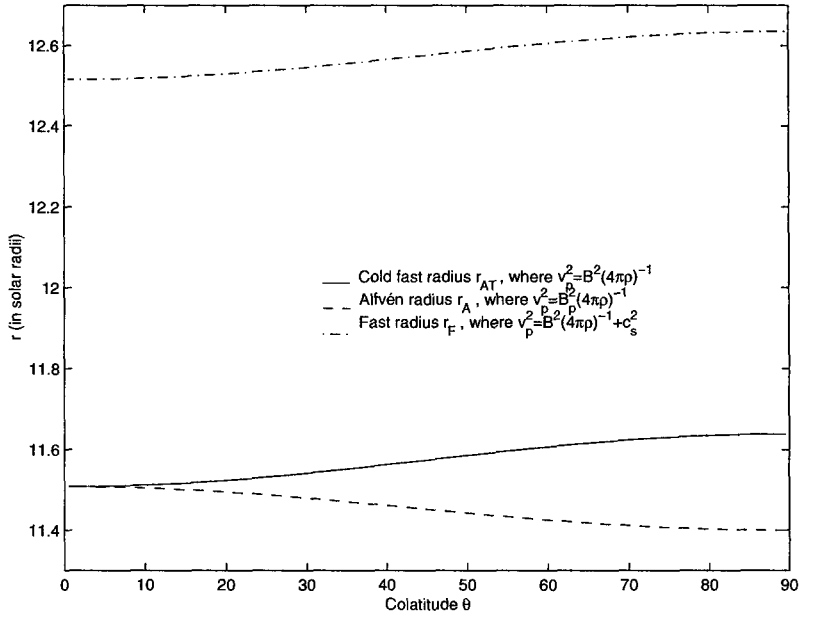

Fig. 6.17 *Solar wind simulation with a 1-day rotation period.*

Values of v_r at six different heights, as a function of colatitude θ.

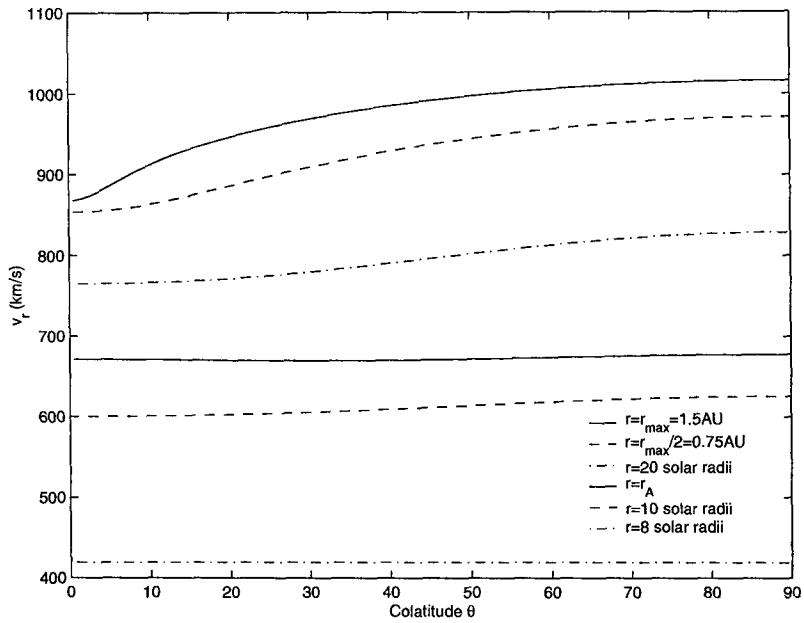

Fig. 6.18 *Solar wind simulation with a 1-day rotation period.*

Critical radii as a function of colatitude θ.

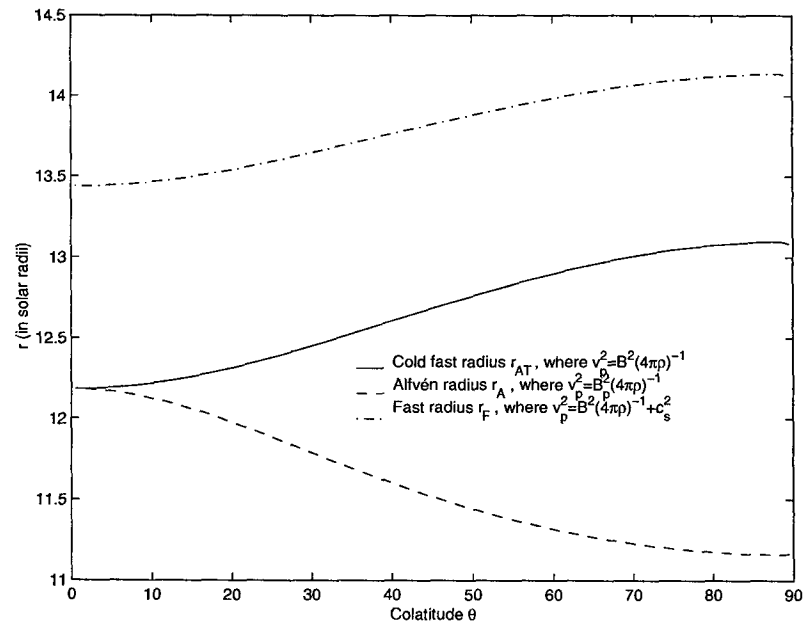

Fig. 6.19 *Solar wind simulation with a 1-day rotation period.*

Ratio between the angle θ_r at a certain radius r and its value θ_F at the footpoint $r = r_{\min}$, taken on the same poloidal fieldline. Two values of r are shown.

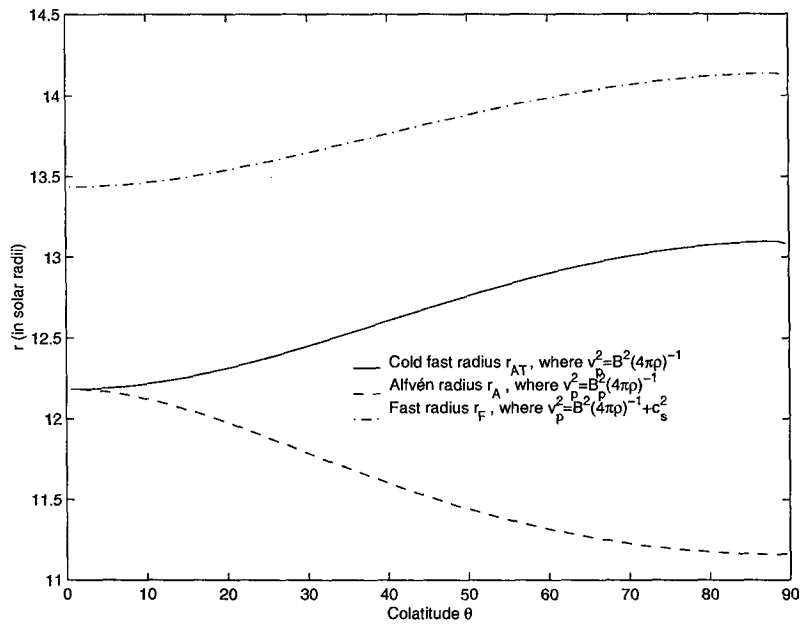

Fig. 6.20 *Solar wind simulation with a 1-day rotation period.*

Twenty poloidal fieldlines, shown on the poloidal plane.

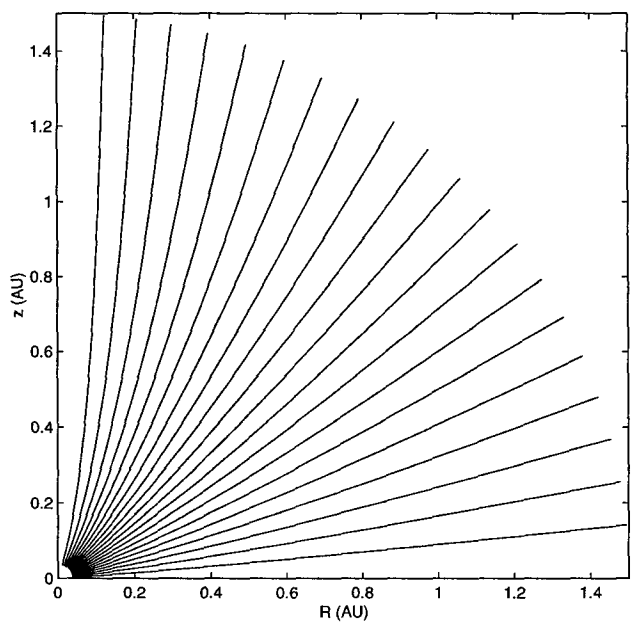

Fig. 6.21 *Bernoulli constant e, from Ulysses data.*

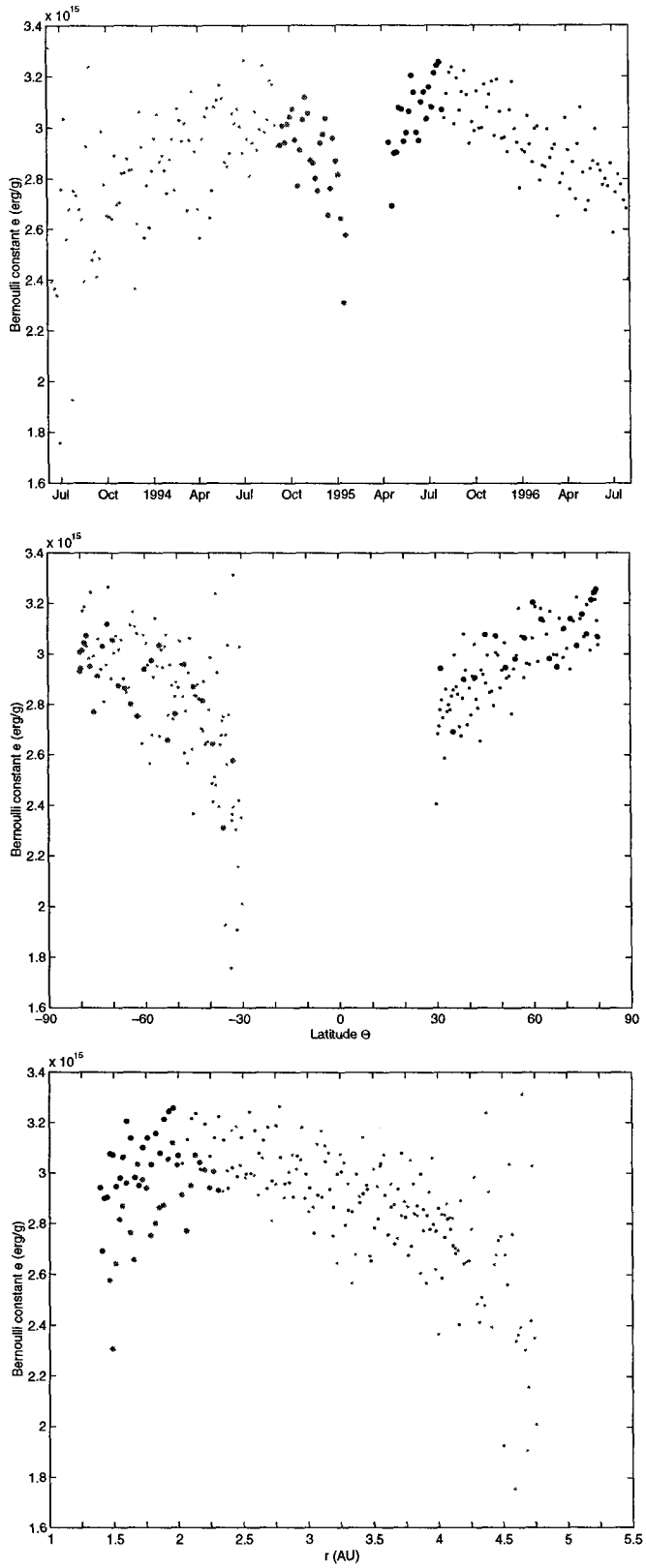

Fig. 6.22 *Specific kinetic energy in the radial direction, $\frac{1}{2}v_r^2$, divided by the Bernoulli constant e. Ulysses data.*

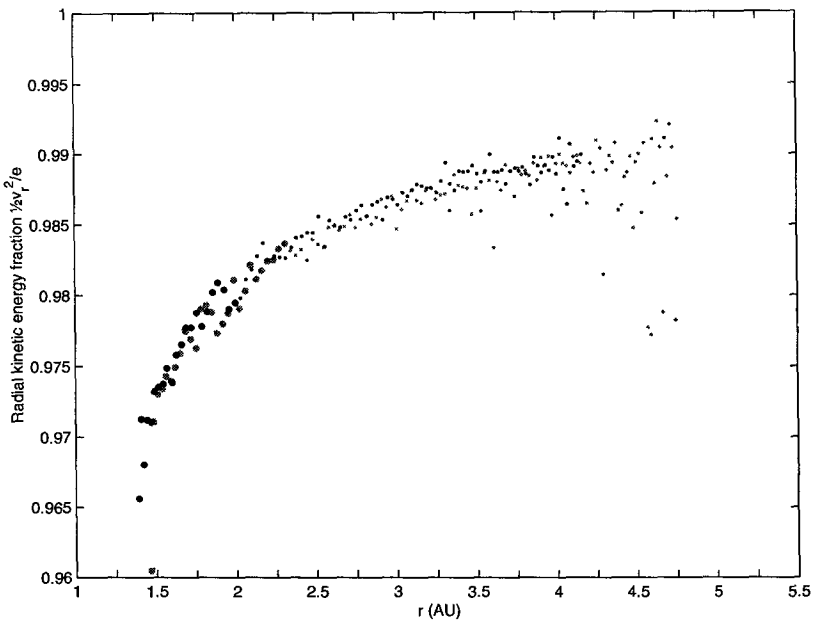

Fig. 6.23 *Specific enthalpy h, divided by the Bernoulli constant e. Ulysses data. This enthalpy has been calculated from the measured temperatures, assuming a polytropic $\gamma = 1.5$.*

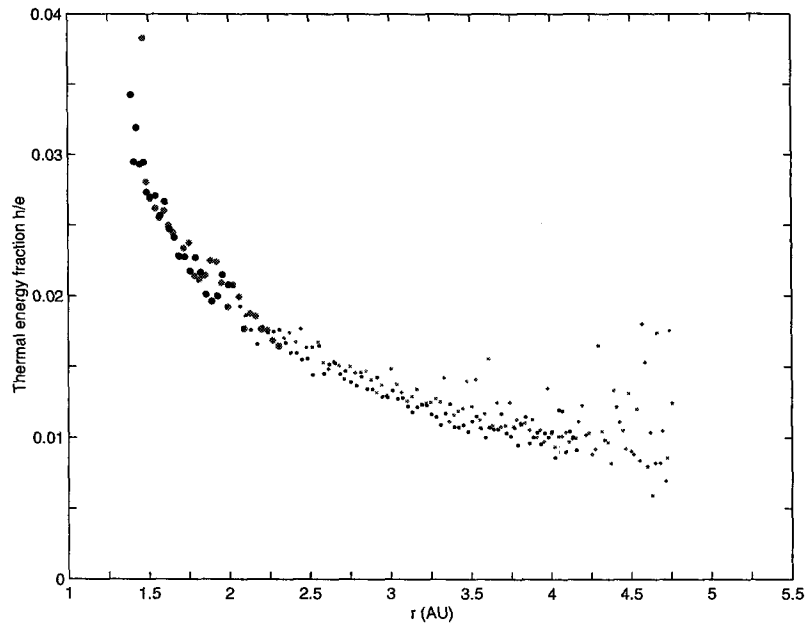

Fig. 6.24 *Specific kinetic energy in the transverse direction,* $\frac{1}{2}\left(v_\phi^2 + v_\theta^2\right)$*, divided by the Bernoulli constant e. Ulysses data. Note that this small term in e is largely influenced by long term biases in Ulysses measurements of* v_ϕ *and* v_θ*.*

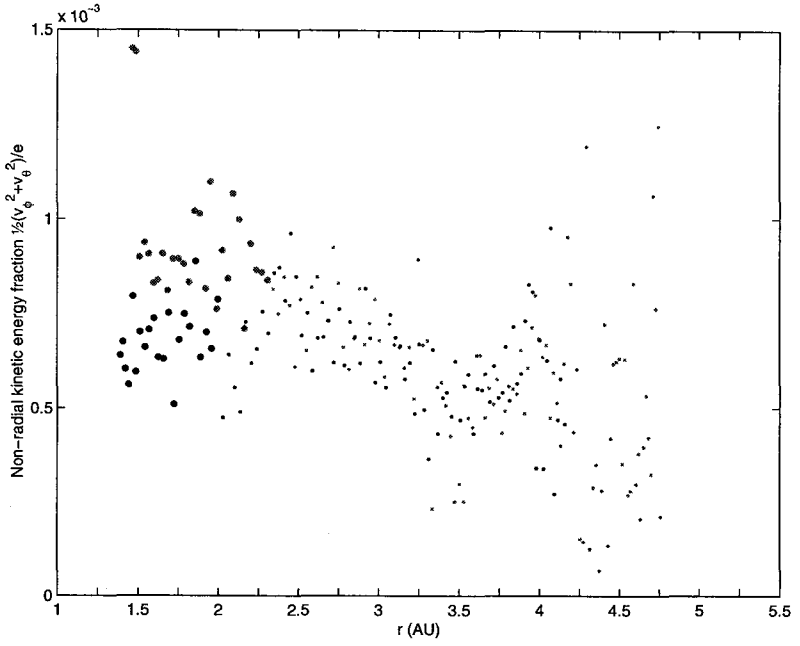

Fig. 6.25 *Gravitational potential* Φ_g*, divided by the Bernoulli constant e. Ulysses data.*

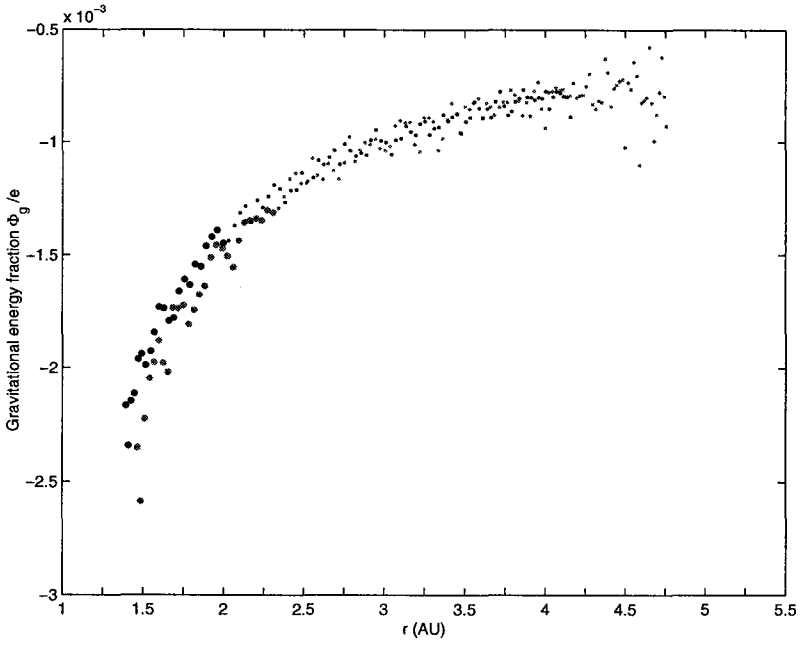

Fig. 6.26 *Magneto-centrifugal term $-R\Omega B_\phi/k$, divided by the Bernoulli constant e. Ulysses data.*

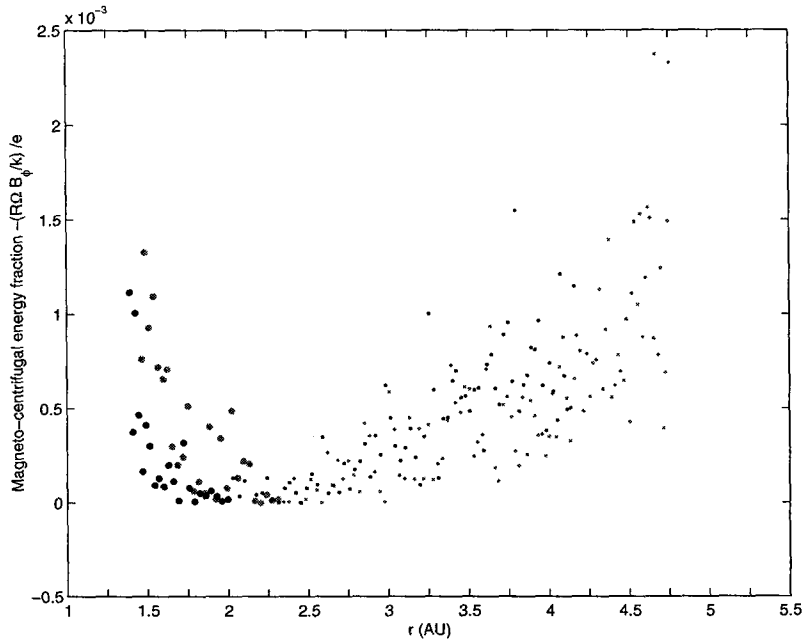

Fig. 6.27 *Specific angular momentum $l = R(v_\phi - B_\phi/k)$, from Ulysses data. Note that this quantity is largely influenced by long term biases in Ulysses measurements of v_ϕ, making an authentic measurement of the angular momentum flux of the solar wind from these data impossible.*

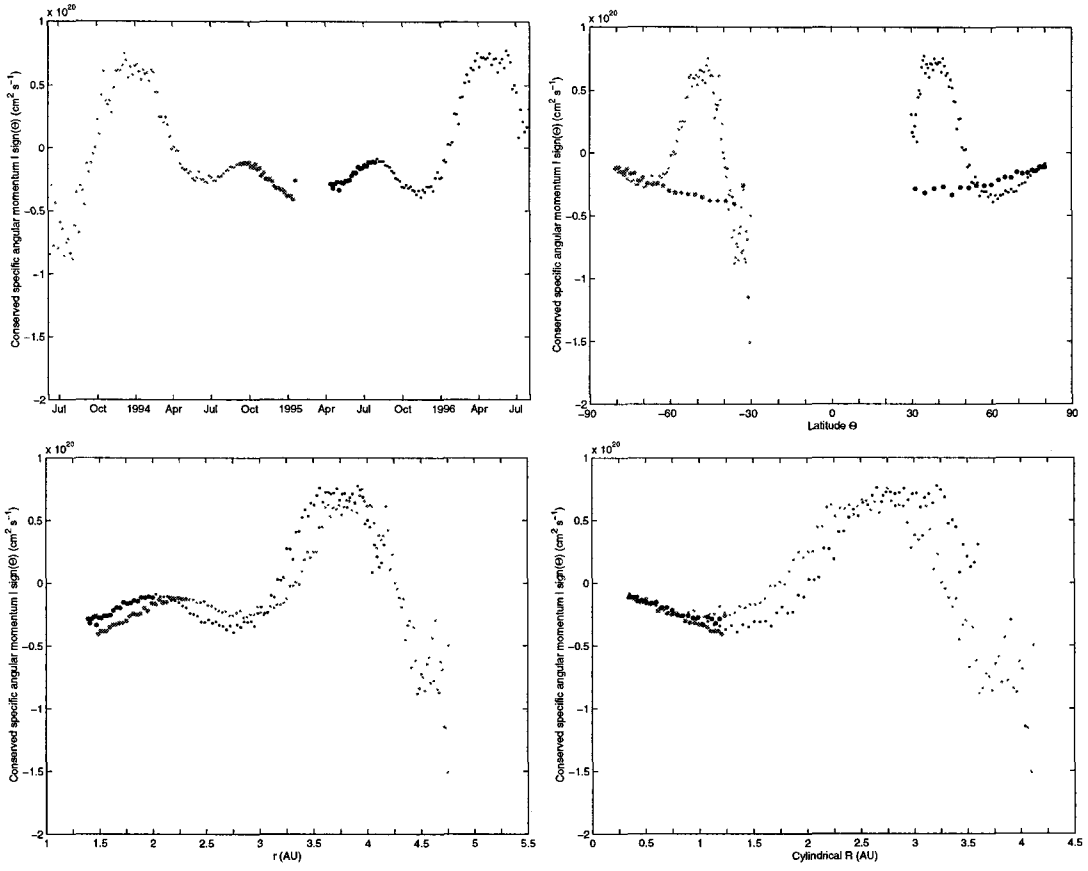

Fig. 6.28 *Specific angular momentum divided by its magnetic term, $-lk/RB_\phi$, from Ulysses data. Note that this quantity is strongly sensitive to the long term biases in Ulysses measurements of v_ϕ.*

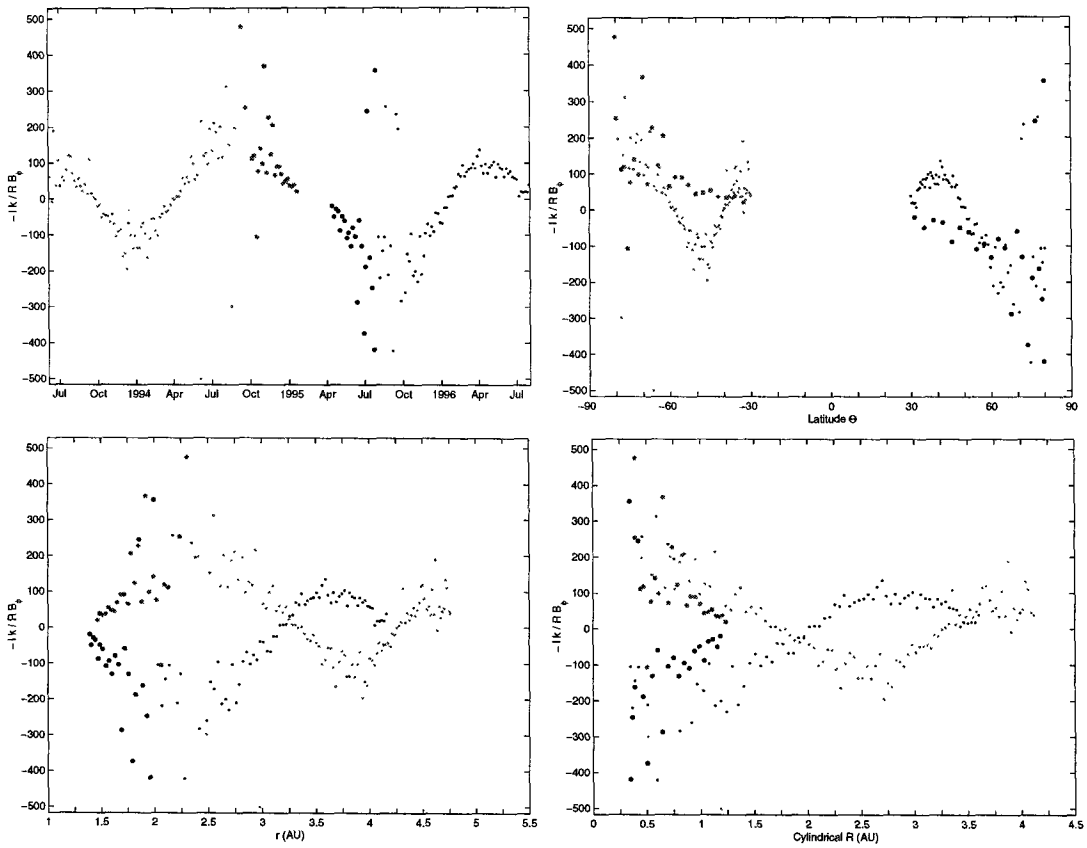

Chapter 7

Conclusions

The principal original conclusions contained in this thesis are:

- It is the total mass flux at the base of the coronal wind, rather than the velocity or the density separately, that determines the character of the outflow.
- There is an intermittent regime of launching, accessible by increasing the mass loading beyond a limit, related to the magnetic flux profile on the disk surface. Transitions between an intermittent and a smooth launching are possible, by changing the amount of mass flux, or by making the mass loading depend on fieldline angle.
- The unexpected 3D stability of the steady-state configurations found against perturbations in the initial conditions, especially against the kink mode, despite reasons to expect such instability.
- Boundary conditions for the disk were written for numerical usage, consistent with mathematical constraints on the number of enforceable boundary conditions. This avoids overdetermining many physical quantities of the wind, such as the inclination of the fieldlines at the disk, the value of the toroidal magnetic field, the Alfvén radius, and the angular momentum flux.
- Data and simulations of the solar wind were combined to produce estimates of the azimuthal velocity and of the Alfvén radius, otherwise not available.
- A stellar wind in faster rotation was simulated, showing again the presence of magnetocentrifugal collimation.

Some of these answers raise new questions and challenges, prompting future simulations, which could give answers to the following questions:

- There is much to be explored concerning the stability of 3D outflows. The results presented here, which were unexpected, encourage to believe that stable outflows can be found. A comprehensive investigation will require 3D simulations with a finer grid, able to reduce artificial dissipation.
- The intermittent mechanism showed how a configuration, initially magnetocentrifugal, was able to change into a generator of pulsed jets. The resulting flows are very complex, and deserve further study. Constructing a theory out of this non-linear and dynamical mechanism only adds to the challenge. Prospects for comparing with observations are good.

- The magnetopropulsive model was mentioned in this thesis as a launching mechanism different from but closely related to the magnetocentrifugal model. It has a stronger azimuthal field at small distances from the disk. Studying its 3D stability against kink modes may teach which of the stabilizing effects for the magnetocentrifugal mechanism is most responsible for the observed stability.

- Integration of outflow models with coronal models such as Miller & Stone (1997) is necessary to answer some physical questions depending on the details of the interaction between the wind and the disk.

- Simulations of the solar conditions should be performed taking into account phenomenological heat transport, and the presence of large amplitude waves, which transport momentum and energy into the flow.

- The success in reducing the number of independent parameters for cold jet launching presented here hints to the possibility of a further reduction, perhaps based on some combination of the mass and magnetic fluxes.

Code will be developed in the future to reflect the physics of these systems more accurately. Relativistic simulations already exist (Aloy et al. 1999; van Putten 1996; Koide et al. 1999) and are a necessary direction for the future numerical study of the jets from AGNs and microquasars.

A black hole magnetosphere and a disk corona require considerations beyond pure MHD, similar to those present in radio pulsars.

The very complex, localized flows revealed in some of the simulations requires the possibility of increasing the resolution by using adaptive methods. Higher space resolution and longer timescales are often conflicting desirable goals, due to the limitations imposed by the Courant condition; new ways of doing as much as possible inside the limitations will be possible by a more intelligent treatment of the computational volume.

Cooling, heat transport, and turbulent magnetic pressure must be added to a realistic simulation of the solar wind, which is the MHD outflow where most data is available; some of these physical effects should also be present on the flows where the data are more sparse.

The observational prospects in the near future are very exciting, with projects such as space VLBI (ARISE, VSOPII); the γ-ray observatory GLAST. Chandra, the $\frac{1}{2}$"-resolution X-ray observatory, is already operating. The Ulysses polar probe is going to perform its solar maximum passage above both poles of the Sun, starting later this year.

There is much to be discovered out there!

Bibliography

M. A. Aloy, J. M. Ibáñez, J. M. Martí, J.-L. Gómez, & E. Müller. 1999, ApJ, 523, L125–L128.

R. R. J. Antonucci & J. S. Miller. 1994, ApJ, 297, 621–632.

N. Arav, Z.-Y. Li, & M. C. Begelman. 1994, ApJ, 432, 62–74.

T. D. Arber & D. F. Howell. 1996, Phys. Plasmas, 3, 554.

A. Balogh, T. J. Beek, R. J. Forsyth, P. Hedgecock, R. J. Marquedant, E. J. Smith, D. Southwood, & B. T. Tsurutani. 1992, A&AS, 92, 221–236.

S. J. Bame, D. J. McComas, B. L. Barraclough, J. L. Phillips, K. J. Sofaly, J. C. Chavez, B. E. Goldstein, & S. R. K. 1992, A&AS, 92, 237–265.

M. C. Begelman. 1998, ApJ, 493, 291–300.

M. C. Begelman, R. D. Blandford, & M. J. Rees. 1984, Rev. Mod. Phys., 56, 255–351.

A. R. Bell & S. G. Lucek. 1995, MNRAS, 277, 1327–1340.

L. Biermann. 1951, Z. Astrophys., 29, 274.

R. D. Blandford, 1993, in "Astrophysical Jets, Proceedings of the Astrophysical Jets Meeting in Baltimore 1992," D. Burgarella, M. Livio, & C. P. O'Dea, eds., Cambidge University Press, p. 15–33.

R. D. Blandford, C. F. McKee, & M. J. Rees. 1977, Nature, 267, 211–216.

R. D. Blandford & D. G. Payne. 1982, MNRAS, 199, 883–903.

R. D. Blandford & R. L. Znajek. 1977, MNRAS, 179, 433–456.

S. V. Bogovalov. 1997, A&A, 323, 634–643.

A. H. Bridle & R. A. Perley. 1984, ARA&A, 22, 319–358.

R. Bruno, B. Bavassano, & U. Villante. 1985, J. Geophys. Res., 90, 4373.

C. J. Burrows, K. R. Stapelfeldt, A. M. Watson, J. E. Krist, G. E. Ballester, J. T. Clarke, D. Crisp, I. Gallagher, John S., R. E. Griffiths, J. J. Hester, J. G. Hoessel, J. A. Holtzman, J. R. Mould, P. A. Scowen, J. T. Trauger, & J. A. Westphal. 1996, ApJ, 473, 437–451.

C. Canuto, M. Y. Hussaini, A. Quateroni, & Z. T. A. *Spectral Methods in Fluid Dynamics.* Springer, Berlin, 1987.

J. W. Chamberlain. 1961, ApJ, 133, 675–687.

J. W. Chamberlain. 1965, ApJ, 141, 320–322.

D. A. Clarke. EDITOR *User Manual*, 1992.
`ftp://zeus.ncsa.uiuc.edu/LCA/codes/zeus3d/editor/manuals/editor21.tex`.

D. A. Clarke, M. L. Norman, & J. O. Burns. 1986, ApJ, 311, L63–L67.

D. A. Clarke, M. L. Norman, & R. A. Fiedler. ZEUS-3D *User Manual*, 1994.
`http://zeus.ncsa.uiuc.edu:8080/lca/zeus3d/zeus32.ps` , or
`ftp://zeus.ncsa.uiuc.edu/LCA/codes/zeus3d/manuals/zeus32.tex`.

M. H. Cohen, 1989, in "BL Lac Objects," L. Maraschi, T. Maccacaro, & M.-H. Ulrich, eds., Lecture Notes in Physics, 334 (Berlin, Springer), p. 13.

P. Colella & P. R. Woodward. 1984, J. Comput. Phys., 54, 174–201.

J. Contopoulos. 1995, ApJ, 450, 616–627.

R. Courant, K. Friedrichs, & H. Lewy. 1928, Math. Ann., 100, 32–74.

L. Dondi & G. Ghisellini. 1995, MNRAS, 273, 583–595.

A. Eckart & R. Genzel. 1997, MNRAS, 284, 576–598.

R. T. Emmering, R. D. Blandford, & I. Shlosman. 1992, ApJ, 385, 460–477.

C. R. Evans & J. F. Hawley. 1988, ApJ, 332, 659–677.

B. L. Fanaroff & J. M. Riley. 1974, MNRAS, 167, 31P–35P.

W. C. Feldman, B. L. Barraclough, J. T. Gosling, D. J. McComas, P. Riley, B. E. Goldstein, & A. Balogh. 1998, J. Geophys. Res., 103, 14547–14557.

L. Ferrarese, H. C. Ford, & W. Jaffe. 1996, ApJ, 470, 444–459.

C. A. J. Fletcher. *Computational Techniques for Fluid Dynamics*, p. 280. Springer, Berlin, 2nd edition, 1990.

H. Ford, Z. Tsvetanov, L. Ferrarese, G. Kriss, W. Jaffe, R. Harms, & L. Dressel, 1997, in "ASP Conf. Ser. 121, Accretion Phenomena and Related Outflows," D. T. Wickramasinghe, G. V. Bicknell, & L. Ferrario, eds., ASP Conference Series, p. 620–625.

R. J. Forsyth, A. Balogh, E. J. Smith, G. Erdös, & D. J. McComas. 1996, J. Geophys. Res., 101, 395–403.

S. T. Garrington, J. P. Leahy, R. G. Conway, & R. A. Laing. 1988, Nature, 331, 147–149.

A. M. Ghez, B. L. Klein, M. Morris, & E. E. Becklin. 1998, ApJ, 509, 678–686.

S. K. Godunov. 1959, Mat. Sb., 47, 271.

B. E. Goldstein, 1999. Private communication.

B. E. Goldstein & D. J. McComas, 1999. NSSDC User's Guide for Data from the Ulysses SWOOPS Plasma Experiment: The Positive Ion Experiment http://helio.estec.esa.nl/ulysses/archive/expt/swoops/Ions/Bai_un.htm.

D. Gottlieb & S. A. Orszag. *Numerical analysis of spectral methods: theory and applications.* SIAM, Philadelphia, 1977.

K. Hain, 1978. NRL Memo Report 3713.

E. Hameiri. 1981, J. Math. Phys., 22, 2080–2088.

P. E. Hardee, D. A. Clarke, & D. A. Howell. 1995, ApJ, 441, 644–664.

P. E. Hardee, D. A. Clarke, & A. Rosen. 1997, ApJ, 485, 533–551.

P. E. Hardee, M. A. Cooper, & D. A. Clarke. 1994, ApJ, 424, 126–137.

P. E. Hardee & A. Rosen. 1999, ApJ, 524, 650–666.

A. Harten, B. Engquist, S. Osher, & S. R. Chakravarthy. 1987, J. Comput. Phys., 71, 231–303.

L. Hartmann & K. B. MacGregor. 1982, ApJ, 257, 264–268.

J. F. Hawley & J. M. Stone. 1995, Comput. Phys., 89, 127–148.

M. Heinemann & S. Olbert. 1978, J. Geophys. Res., 83, 2457–2460.

R. N. Henriksen & D. R. Rayburn. 1971, MNRAS, 152, 323–332.

L. Hernquist & N. Katz. 1989, ApJS, 70, 419–446.

J. Heyvaerts & C. Norman. 1989, ApJ, 347, 1055–1081.

H. M. Hjellming, 1997, in "ASP Conf. Ser. 121, Accretion Phenomena and Related Outflows," D. T. Wickramasinghe, G. V. Bicknell, & L. Ferrario, eds., ASP Conference Series, p. 53–62.

H. M. Hjellming & M. P. Rupen. 1995, Nature, 375, 464–467.

L. C. Ho, A. V. Filippenko, & W. L. W. Sargent. 1997, ApJ, 487, 568–578.

C. Hoffmeister. 1944, Z. Astrophys., 23, 1.

J. Huchra & R. Burg. 1992, ApJ, 393, 90–97.

V. Kalogera & G. Baym. 1996, ApJ, 470, L61–L64.

W. C. Keel. 1983, ApJ, 269, 466–486.

R. Keppens & J. P. Goedbloed. 1999, A&A, 343, 251–260.

S. Koide, K. Shibata, & T. Kudoh. 1998, ApJ, 495, L63–L66.

S. Koide, K. Shibata, & T. Kudoh. 1999, ApJ, 522, 727–752.

A. Königl. 1989, ApJ, 342, 208–223.

A. Königl & J. F. Kartje. 1994, ApJ, 434, 446–467.

A. Königl & R. E. Pudritz, 2000, in "Protostars and Planets IV," V. Mannings, A. Boss, & S. Russell, eds., University of Arizona Press, to appear. Available electronically at astro-ph/9903168.

V. M. Kontorovich. 1959, JETP, 35, 851–858.

J. Kormendy & D. Richstone. 1995, ARA&A, 33, 581–624.

R. Krasnopolsky, Z.-Y. Li, & R. D. Blandford. 1999, ApJ, 526, 631–642.

T. Kudoh, K. Shibata, & R. Matsumoto, 1998, in "IAU Symp. No. 184, The Central Region of the Galaxy and Galaxies," Y. Sofue, ed., IAU, p. 361–362.

C. J. Lada. 1985, ARA&A, 23, 267–317.

R. A. Laing. 1988, Nature, 331, 149–151.

R. A. Laing, 1996, in "ASP Conf. Ser. 100, Energy Transport in Radio Galaxies and Quasars," P. E. Hardee, A. H. Bridle, & J. A. Zensus, eds., ASP Conference Series, p. 241–252.

L. D. Landau & E. M. Lifshitz. *Fluid Mechanics*, p. 394–397 (§104). Pergamon, Oxford, 2nd edition, 1987.

A. Levinson & R. Blandford. 1996, Astron. Astrophys. Suppl. Ser., 120, 129–132.

Z.-Y. Li. 1996, ApJ, 465, 855–868.

K. R. Lind, D. G. Payne, D. L. Meier, & R. D. Blandford. 1989, ApJ, 295, 358–367.

M. Livio, 1997, in "ASP Conf. Ser. 121, Accretion Phenomena and Related Outflows," D. T. Wickramasinghe, G. V. Bicknell, & L. Ferrario, eds., ASP Conference Series, p. 845–866.

R. V. E. Lovelace, C. Mehanian, C. M. Mobarry, & M. E. Sulkanen. 1986, ApJS, 62, 1–37.

S. H. Lubow, J. C. B. Papaloizou, & J. E. Pringle. 1994, MNRAS, 267, 235–240.

S. G. Lucek & A. R. Bell. 1997, MNRAS, 290, 327–333.

M. Manzini, 1994. Numerical methods for 1D compressible flows, an interactive book http://www.crs4.it/HTML/int_book/NumericalMethods/int_book.html.

P. S. Marcus. 1988, Nature, 331, 693–696.

B. Margon. 1984, ARA&A, 22, 507–536.

D. Meier, S. Edgington, P. Godon, D. Payne, & K. Lind, 1997, in "ASP Conf. Ser. 123, The 12th Kingston meeting: Computational Astrophysics," D. A. Clarke & M. J. West, eds., ASP Conference Series, p. 290–295.

D. L. Meier, 1998. Private communication.

L. Mestel. 1968, MNRAS, 138, 359–391.

K. A. Miller & J. M. Stone. 1997, ApJ, 489, 890–902.

I. F. Mirabel, B. Cordier, J. Paul, & F. Lebrun. 1992, Nature, 358, 215.

I. F. Mirabel & L. F. Rodríguez. 1994, Nature, 371, 46–48.

I. F. Mirabel & L. F. Rodríguez. 1998, Nature, 392, 673–676.

I. F. Mirabel & L. F. Rodríguez. 1999, ARA&A, 37, 409–443.

T. Nakano & T. Umebayashi. 1986, MNRAS, 221, 319–338.

K.-I. Nishikawa, S. Koide, J.-I. Sakai, D. M. Christodoulou, H. Sol, & R. L. Mutel. 1997, ApJ, 483, L45–L48.

K.-I. Nishikawa, S. Koide, J.-I. Sakai, D. M. Christodoulou, H. Sol, & R. L. Mutel. 1998, ApJ, 498, 166–169.

M. L. Norman. *The* ZEUS-3D *Code*. `http://zeus.ncsa.uiuc.edu:8080/lca_intro_zeus3d.html`, 1996.

M. L. Norman, J. R. Wilson, & R. T. Barton. 1980, ApJ, 239, 968–981.

J. A. Orosz & C. D. Bailyn. 1997, ApJ, 477, 876–896.

E. C. Ostriker. 1997, ApJ, 486, 291–306.

R. Ouyed & R. E. Pudritz. 1997a, ApJ, 484, 794–809.

R. Ouyed & R. E. Pudritz. 1997b, ApJ, 482, 712–732.

R. Ouyed & R. E. Pudritz. 1999, MNRAS, 309, 233–244.

E. N. Parker. 1958, ApJ, 128, 664–676.

E. N. Parker. 1965, ApJ, 141, 1463–1478.

S. N. Phillips, T. Shahbaz, & P. Podsiadlowski. 1999, MNRAS, 304, 839–844.

T. Piran. 1999, Phys. Rep., 314, 575.

W. H. Press, B. P. Flannery, S. A. Teukolsky, & W. T. Vetterling. *Numerical Recipes in Fortran, The Art of Scientific Computing*, chapter 19, p. 854–862. Cambridge University Press, 2nd edition, 1992.

R. E. Pudritz & C. A. Norman. 1986, ApJ, 301, 571–586.

M. J. Rees. 1966, Nature, 211, 468–470.

B. Reipurth, J. Bally, J. A. Graham, A. P. Lane, & W. J. Zealey. 1986, A&A, 164, 51–66.

R. D. Richtmyer & K. W. Morton. *Difference Methods for Initial-Value Problems.* Wiley, New York, 2nd edition, 1967.

P. L. Roe. 1985, Lectures in Applied Mathematics, 22, 163.

M. M. Romanova, G. V. Ustyugova, A. V. Koldoba, V. M. Chechetkin, & R. V. E. Lovelace. 1997, ApJ, 482, 708–711.

F. H. Shu, J. Najita, E. C. Ostriker, & H. Shang. 1995, ApJ, 455, L155–L158.

F. H. Shu, J. R. Najita, S. H., & Z.-Y. Li, 2000, in "Protostars and Planets IV," V. Mannings, A. Boss, & S. Russell, eds., University of Arizona Press, to appear.

P. S. Smith, 1996, in "ASP Conf. Ser. 110, Blazar Continuum Variability," H. R. Miller, J. R. Webb, & J. C. Noble, eds., ASP Conference Series, p. 135–149.

K. A. Southwell, M. Livio, P. A. Charles, D. O'Donoghue, & W. J. Sutherland. 1996, ApJ, 470, 1065–1074.

J. M. Stone & M. L. Norman. 1992, ApJS, 80, 753–790 and 791–818.

J. M. Stone & M. L. Norman. 1993, ApJ, 413, 198–209 and 210–220.

S. T. Suess, J. L. Phillips, D. J. McComas, B. E. Goldstein, M. Neugebauer, & S. Nerney. 1998, Space Sci. Rev., 83, 75–86.

P. K. Sweby. 1984, SINUM, 21, 995.

S. J. Tingay, D. L. Jauncey, R. A. Preston, J. E. Reynolds, D. L. Meier, D. W. Murphy, A. K. Tzioumis, D. J. McKay, M. J. Kesteven, J. E. J. Lovell, D. Campbell-Wilson, S. P. Ellingsen, R. Gough, R. W. Hunstead, D. L. Jones, P. M. McCulloch, V. Migenes, J. Quick, M. W. Sinclair, & D. Smits. 1995, Nature, 374, 141–143.

Y. Uchida & K. Shibata. 1985, Publ. Astron. Soc. Japan", 37, 515–535.

S. C. Unwin, M. H. Cohen, M. W. Hodges, J. A. Zensus, & J. A. Biretta. 1989, ApJ, 340, 117–128.

C. M. Urry, 1996, in "ASP Conf. Ser. 110, Blazar Continuum Variability," H. R. Miller, J. R. Webb, & J. C. Noble, eds., ASP Conference Series, p. 391–402.

C. M. Urry & P. Padovani. 1995, PASP, 107, 803–845.

G. V. Ustyugova, A. V. Koldoba, M. M. Romanova, V. M. Chechetkin, & R. V. E. Lovelace. 1999, ApJ, 516, 221–235.

B. van Leer. 1979, J. Comput. Phys., 32, 101–136.

J. van Paradijs & J. E. McClintock, 1995, in "X-Ray Binaries," W. H. G. Lewin, J. van Paradijs, & E. P. J. van den Heuvel, eds., Cambridge University Press, p. 58.

M. H. P. M. van Putten. 1996, ApJ, 467, L57–L60.

R. C. Vermeulen & M. H. Cohen. 1994, ApJ, 430, 467–494.

J. von Neumann & R. D. Richtmyer. 1950, J. Appl. Phys., 21, 232–237.

E. J. Weber & L. Davis. 1967, ApJ, 148, 217–227.

R. J. Weymann, S. L. Morris, C. B. Foltz, & P. C. Hewett. 1991, ApJ, 373, 23–53.

L. Woltjer, 1990, in "Active Galactic Nuclei," T. J.-L. Courvoisier & M. Mayor, eds., Saas-Fee Advanced Course 20 (Berlin, Springer), p. 1–55.

S. T. Zalesak, 1987, in "Advances in Computer Methods for Partial Differential Equations," R. Vichnevetsky & R. S. Stepleman, eds., IMACS, p. 15–22.